The keV–TeV connection in gamma-ray binaries

Víctor Zabalza de Torres

The keV–TeV connection in gamma-ray binaries

PhD thesis

Víctor Zabalza

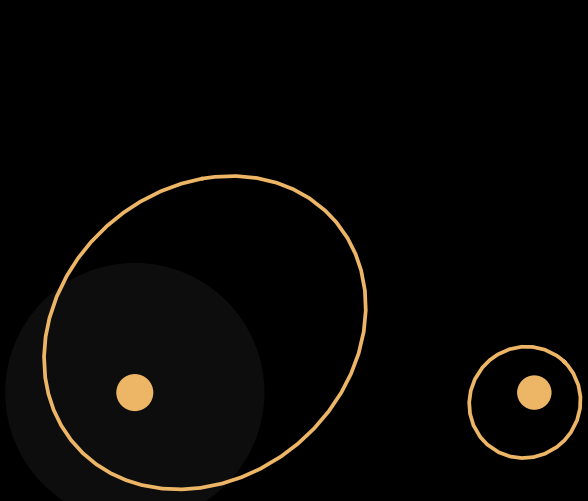

UNIVERSITAT DE BARCELONA

Departament d'Astronomia i Meteorologia

The keV–TeV connection in gamma-ray binaries

Víctor Zabalza de Torres

Barcelona, Maig de 2011

Programa de doctorat en Física

Línia de Recerca en Astronomia i Astrofísica

2007–2011

Memòria presentada per **Víctor Zabalza de Torres**
per optar al grau de Doctor en Física

Director

Dr. Josep Maria Paredes Poy

Front cover illustration: Orbital sketches of the three gamma-ray binaries with known orbital parameters: LS I +61 303, LS 5039 and PSR B1259−63, from left to right. For the first two, the observer direction is downwards, whereas for PSR B1259−63 the orientation of the orbit is unknown and has been assumed. The decretions discs of Be stars are also shown.
Back cover illustration: Word frequency cloud generated by `www.wordle.net` using the text of this thesis.

I do not know what I may appear to the world; but to myself I seem to have been only like a boy playing on the seashore, and diverting myself in now and then finding a smoother pebble or a prettier shell than ordinary, whilst the great ocean of truth lay all undiscovered before me.

Isaac Newton

Acknowledgements

This thesis would not have been possible without the help of many people who have guided and supported me during these years. I am indebted to all the members of the group of high-energy astrophysics at the Universitat de Barcelona, and in particular to my advisor Dr. Josep Maria Paredes, for providing an exciting scientific environment. Their advise, motivation and expertise are the indisputable foundation of this thesis. I would also like to thank all the scientific collaborators around the world that have enormously helped to improve the content of this thesis and in my formation as a researcher. I am also thankful to all my colleagues of the Departament d'Astronomia i Meteorologia for their support and great times both in and out of the department. I am grateful to my family and friends, who have given me the motivation and support I needed during these years. And most of all I would like to thank the loving, understanding, encouraging, and patient Laura, whose constant love and support have helped make this Ph.D. thesis a reality.

To all of you, thank you.

Contents

Resum de la tesi

La connexió keV–TeV a les binàries de raigs gamma

La radiació de raigs gamma és intrínsecament diferent de la radiació emesa en la resta de l'espectre electromagnètic perquè no pot ser generada per la matèria calenta. Per a emetre radiació a energies majors que 1 MeV és necessària la presència dels anomenats processos no tèrmics d'emissió. Aquests processos són capaços de concentrar una gran quantitat d'energia en cada un dels fotons emesos extraient-la de partícules accelerades fins a velocitats relativistes. L'astrofísica d'altes energies estudia alguns dels entorns més energètics de l'univers a través de la seva emissió de raigs gamma, detectada mitjançant observatoris espacials per a raigs gamma d'alta energia (0.1–10 GeV, amb *Fermi* i *AGILE*) o telescopis de Cherenkov atmosfèric localitzats a terra per a raigs gamma de molt alta energia (>100 GeV, amb MAGIC, VERITAS i HESS).

Els darrers anys hem vist un augment significatiu dels resultats observacionals obtinguts en raigs gamma de molt alta energia, passant de menys d'una desena de fonts astrofísiques detectades a finals del segle passat fins a prop de cent fonts avui dia. Aquestes comprenen moltes categories d'entorns astrofísics, com romanents de supernova (SNR), nebuloses de vent de púlsar (PWN) o nuclis actius de galàxia (AGN), entre d'altres (veure secció 1.2 per a una explicació exhaustiva). En totes elles s'hi donen lloc processos que acceleren partícules fins a molt altes energies, bé mitjançant xocs de plasma o dolls relativistes de matèria.

Un dels tipus de fonts que van ser descoberts durant la darrera dècada en raigs gamma de molt alta energia són les binàries de raigs gamma. Aquests sistemes binaris contenen una estrella jove que esta lligada gravitacionalment a un objecte compacte, i.e., un forat negre o una estrella de neutrons. Actualment se'n coneixen quatre: PSR B1259−63, LS 5039, LS I +61 303 i HESS J0632+057. Tot i que sabem que l'objecte compacte a PSR B1259−63 es tracta d'un púlsar jove, no s'han pogut detectar pulsacions a les altres tres fonts, fet que desperta molt interès sobre els escenaris que poden donar lloc a l'emissió multi longitud d'ona. En cas que l'objecte compacte fos un forat negre o

una estrella de neutrons acretant, l'emissió provindria de les partícules accelerades als dolls relativistes generats en acretar matèria de l'estrella. En cas que l'objecte compacte fos un púlsar jove, l'escenari seria similar al del PSR B1259−63, i l'emissió no tèrmica provindria del vent del púlsar xocat en interaccionar amb el potent vent estel·lar.

Totes les binàries de raigs gamma conegudes mostren variabilitat orbital en la radiació emesa en tot l'espectre electromagnètic, des de radio fins a raigs gamma de molt alta energia, i sabem que aquesta prové d'una o vàries poblacions d'electrons relativistes. La presència dels camps magnètics de l'estrella i de l'objecte compacte fa que aquests electrons emetin radiació sincrotró des de radio fins a raigs X durs. L'emissió de raigs gamma d'alta i molt alta energia prové de la interacció dels electrons amb els fotons estel·lars mitjançant Compton Invers. A més, per a les propietats físiques de les binàries de raigs gamma el mateix rang d'energia d'electrons d'alta energia es responsable de l'emissió sincrotró en raigs X (fotons d'energia al voltant del kiloelectronVolt, keV) i l'emissió Compton Invers en raigs gamma de molt alta energia (fotons d'energia al voltant del TeraelectronVolt, TeV). Això ens dóna la possibilitat d'estudiar una mateixa població d'electrons a través de dos processos independents i ens aporta informació no només sobre els electrons relativistes sinó també sobre el camp magnètic, la densitat de radiació i l'absorció a l'emissor no tèrmic. Les binàries de raigs gamma són un laboratori excellent per a posar a prova i millorar els nostre coneixement sobre els processos d'emissió de raigs gamma de molt alta energia. El moviment de l'objecte compacte i l'emissor no tèrmic al voltant de l'estrella dóna lloc a una modulació periòdica de l'entorn en el que es genera l'emissió de molt alta energia, proporcionant-nos l'oportunitat de deduir l'estructura i propietats del sistema a partir de les propietats espectrals i temporals de l'emissió no tèrmica de la font.

Aquesta tesi és el resultat de l'estudi de les binàries de raigs gamma des d'un punt de vista multi longitud d'ona. Hem fet servir una combinació de mètodes observacionals i teòrics per a aprofundir en el coneixement d'aquests sistemes, així com per cercar-ne de nous.

Als Capítols 1 i 2 fem una introducció al camp de l'astrofísica d'altes energies i als processos d'acceleració de partícules, de radiació i absorció més rellevants per a l'emissió de raigs gamma de molt alta energia.

Al Capítol 3 presentem el descobriment de la correlació entre l'emissió de raigs X i raigs gamma de molt alta energia a la binària LS I +61 303. Aquest descobriment va ser resultat d'una campanya simultània d'observació amb el telescopi Cherenkov MAGIC i els satèl·lits de raigs X *XMM-Newton* i *Swift*. A continuació en fem una interpretació física al Capítol 4 mitjançant l'ela-

boració d'un model numèric radiatiu que permet reproduir les observacions simultànies a partir de l'emissió multi longitud d'ona d'una única població d'electrons relativistes. L'elaboració d'aquest model ens permet restringir significativament les propietats físiques de l'emissor no tèrmic i comprovar que l'origen de les variacions en flux és compatible amb pèrdues adiabàtiques dominants a l'emissor.

En cas que la font energètica d'una binària de raigs gamma sigui un púlsar jove, la potència del vent d'aquest púlsar és una dada bàsica per a avaluar el nivell d'emissió no tèrmica. Als sistemes LS 5039 i LS I +61 303 no s'ha pogut detectar el possible púlsar i per tant en desconeixem la seva potència. Al Capítol 5 presentem un mètode per a restringir els valors possibles de la potència del vent del púlsar a través de l'emissió tèrmica en raigs X del vent xocat de l'estrella. En la interacció entre els dos vents, el vent de l'estrella s'escalfa fins temperatures de desenes de milions de graus i emet radiació en el rang de raigs X. La lluminositat total de la radiació tèrmica depen en forta mesura de la forma de la regió d'interacció, que ve determinada per la relació de potències dels vents del púlsar i l'estrella. Donat que observacionalment no es detecta l'emissió tèrmica, podem establir límits superiors a la potència del púlsar a partir de la comparació del càlcul teòric d'emissió tèrmica amb els espectres de raigs X obtinguts per *XMM-Newton*. Amb aquest mètode hem pogut restringir la potència del vent del púlsar a un rang reduït al voltant de $\sim 5 \times 10^{36}$ erg s^{-1}.

Finalment presentem la cerca d'emissió de raigs gamma de molt alta energia provinent del microquàsar Sco X-1 al Capítol 6. Sco X-1 és la font de raigs X més brillant del cel, i seus colors en raigs X es poden relacionar amb els estats d'acreció de matèria sobre l'estrella de neutrons. En un d'aquests estats es forma un doll relativista de matèria, que emet radiació no tèrmica en raigs X durs. Vam realitzar una campanya d'observació simultània amb el telescopi de raigs gamma de molt alta energia MAGIC i el satèl·lit de raigs X *RXTE* per a poder seleccionar les dades de la font durant els diferents estats d'acreció. Malauradament, no vam detectar emissió significativa de raigs gamma de molt alta energia, però els límits superiors obtinguts seran molt útils per a futurs models de l'emissió no tèrmica de la font.

1

Introduction

1.1 High energy astrophysics

The gamma-ray emission from astrophysical sources is arguably different from the emission in the rest of the electromagnetic spectrum because it cannot be generated by hot matter. High energy gamma radiation is therefore an indication that non-thermal processes, which are able to concentrate a large amount of energy into a single emitted photon, are taking place. These processes are related to populations of relativistic particles accelerated in energetic astrophysical scenarios. The interaction of these relativistic particles with their environment –magnetic field, radiation and cold gas– can generate high-energy gamma rays. For some sources the total emitted power above 1 GeV is larger that the power emitted over all the rest of the electromagnetic spectrum. The detection and study of gamma rays allows us to probe into the properties of the most extreme astrophysical sources in the universe.

Until recently, the highest energy band in observational gamma-ray astronomy was the range 0.1–10 GeV, covered by the Energetic Gamma Ray Experiment Telescope (EGRET) aboard the Compton Gamma-Ray Observatory (CGRO). EGRET provided an extremely rich dataset from which a catalog of 270 galactic and extragalactic gamma-ray sources was extracted (Hartman et al., 1999). The next generation of space-borne gamma-ray observatory was embodied in the Gamma-Ray Large Area Space Telescope (GLAST) (later

renamed to *Fermi*), launched in summer 2008. The *Fermi*/LAT instrument, sensitive in the range 0.3–30 GeV, has a field of view of 30% of the whole sky, which combined with survey mode operations, provides a broad coverage of variable sources with variability timescales from seconds up to years. The first year of observations already improved on our view of the gamma-ray sky as compared to EGRET, and provided a catalog of 1451 sources (Abdo et al., 2010, see also Fig. 1.1 for the all-sky two year map from *Fermi*). However, the weight and size limitations of space observatories preclude them from providing effective detection areas above 1 m^2. The reduced number of photons at energies above 100 GeV makes this a practical limit for the observations of TeV sources.

A way to overcome the limits of space-borne observatories has been to detect the highest energy gamma-rays from ground detectors using either direct air shower particle detection or atmospheric Cherenkov telescopes. However, the extremely high background induced by cosmic rays requires these detectors to adequately discriminate between gamma-ray and cosmic ray events. At energies of a few hundred GeV, the Imaging Atmospheric Cherenkov Telescope (IACT) observatories have demonstrated to provide effective rejection of cosmic ray events (up to a factor 10^3) and further improve their sensitivity through their good angular resolution of ~0.1°. A more detailed account of the IACT gamma-ray detection technique is given in Appendix A. The first detection of a source at very high energy (VHE) gamma-rays was performed by the Whipple IACT with the detection of the Crab Nebula (Weekes et al., 1989). Following this breakthrough detection, several IACTs were developed during the 1990s and led to important astrophysical results and discoveries. However, VHE astronomy was still limited to fewer than ten sources. Based on the strengths of these observatories, the current-generation IACTs were developed, namely the High Energy Stereoscopic System (HESS), the Major Atmospheric Gamma-ray Imaging Cherenkov (MAGIC) telescopes and the Very Energetic Radiation Imaging Telescope Array System (VERITAS), in order of first light date. These telescopes have provided us with a population of nearly a hundred VHE emitting sources and have clearly established VHE gamma-ray observations as a new discipline in observational astrophysics. Additionally, the MILAGRO water Cherenkov detector has proven the effectiveness of the direct extensive air shower (EAS) detection technique through the discovery of three new TeV sources (Abdo et al., 2007), one of them confirmed by HESS. A view of the current galactic and extragalactic VHE gamma-ray source catalog is shown in Figure 1.2.

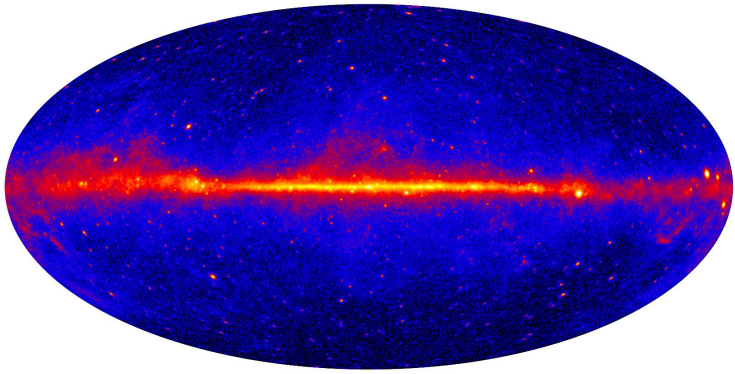

Figure 1.1: All-sky map of HE gamma-ray intensity plotted in galactic coordinates (as for Fig. 1.2). The image has been generated from data obtained during the first two years of operation of *Fermi*/LAT in the energy range 0.3–30 GeV. Image from Vandenbroucke et al. (2010).

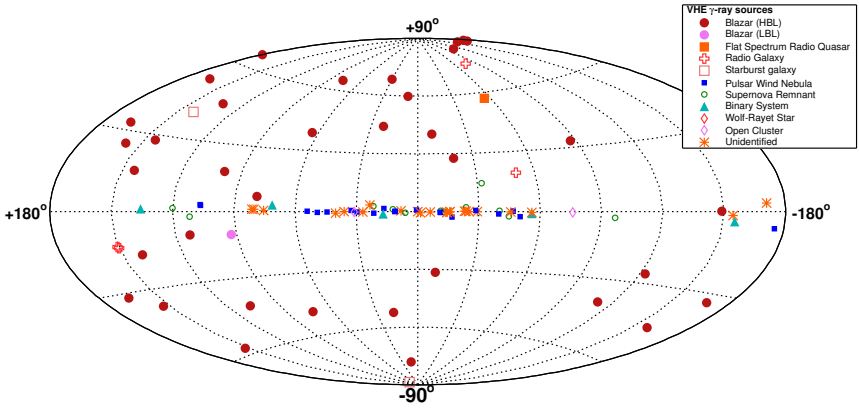

Figure 1.2: All-sky map in galactic coordinates of sources detected at energies above 100 GeV as of March 2011. Image courtesy of Robert Wagner, up-to-date plot available at `http://www.mppmu.mpg.de/~rwagner/sources`.

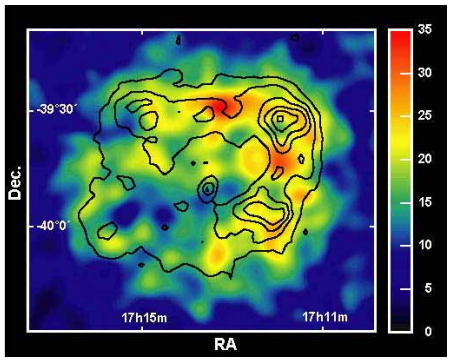

Figure 1.3: Gamma-ray image of the SNR RX J1713.7−3946 obtained with the HESS telescopes. The black contours correspond to 1–3 keV X-ray intensity from ASCA. Image from (Aharonian et al., 2004a).

1.2 Sources of VHE gamma-ray emission

In spite of the relatively small number of sources detected in VHE gamma-rays there is a diverse collection of source classes. Here we will briefly introduce some of them, leaving the category of gamma-ray binaries for a more detailed description in Section 1.3.

Supernova Remnants (SNRs) SNRs were already proposed as the most likely sources of galactic cosmic rays up to an energy of 10^{15} eV in the 1930s (Baade & Zwicky, 1934). The possibility to spatially resolve the SNR in VHE gamma-rays has allowed to study the acceleration that takes place in the strong shocks of the SNR shell. A clear example of the power of VHE observations of SNRs is the case of RX J1713.7−3946 (see Fig. 1.3, Aharonian et al., 2004a).

Pulsar Wind Nebulae (PWNe) In these objects a rapidly spinning neutron star produces a relativistic electron wind that on interaction with the outer shells of the parent supernova remnant produce synchrotron X-ray emission and VHE through Inverse Compton (IC) upscattering of CMB photons. A good example of this class is the detection of energy-dependent morphology in the PWN HESS J1825−137 (Aharonian et al., 2006b), with a smaller extension at higher photon energies, as expected owing to the radiative cooling of electrons convecting away from the pulsar. Many extended VHE sources have been identified as PWNe thanks to the detection of pulsed emission at GeV with *Fermi*, and, in one case, *AGILE*.

Galactic Center The region around the galactic center has been extensively observed by HESS, detecting a point-like source coincident with Sgr A* (Aharonian et al., 2004b) and diffuse, extended emission along the galactic plane coincident with the Galactic Center Ridge (Aharonian et al., 2006a). The origin of the point-like source is not clear, but the morphological match of the diffuse emission with the density of molecular clouds indicates that its origin is the proton-proton interaction of cosmic rays emitted from a central source of age $\sim 10^4$ yr.

Open Clusters The extended source HESS J1023−575 was found to be compatible with the open cluster Westerlund 2 (Aharonian et al., 2007b). Some of the considered emission scenarios for this source include the colliding wind zone of WR 20a (a massive binary in Westerlund 2), collective stellar winds from the ensemble of hot and massive stars in the stellar cluster, diffusive shock acceleration in the wind-blown bubble itself, and supersonic winds breaking out into the interstellar medium.

Unidentified Galactic Plane sources As can be seen in Figure 1.2, as many as 30 VHE sources in the galactic plane remain unidentified. Most of them were detected as the result of the HESS Galactic Plane Survey (Aharonian et al., 2006c) or the all-sky operations of MILAGRO (Abdo et al., 2007). Most of them are extended or elongated, which suggests an SNR and/or PWN origin, but no counterpart at other wavelengths has been found yet.

Active Galactic Nuclei (AGNs) The relativistic jets launched from the supermassive black holes in AGNs provide a population of accelerated particles that radiate from radio to VHE. Their broadband spectra are usually well explained by an electronic population emitting through synchrotron and either synchrotron self Compton or external IC mechanisms. Some of these sources exhibit extremely fast variability and have challenged the current understanding of AGN jets, with Doppler factors of up to 100 required to explain the 3 minute flux-doubling time observed in PKS 2155−304 (Aharonian et al., 2007a). The distance to some of these sources provides the opportunity to study the Extragalactic Background Light (EBL) through the pair-production absorption of the VHE spectra of AGNs.

1.3 Gamma-ray binaries

One of the advances that best exemplifies the qualitative increase in scientific output of the current generation of Cherenkov telescopes is the discovery of

a population of X-ray binaries that emit VHE gamma-rays. The study of the emission of VHE gamma-rays from binary systems provides a unique laboratory to test the physical processes that undergo the relativistic populations of particles accelerated within.

Gamma-ray binaries are binary systems comprised of an young, massive star and a compact object. They display non-thermal emission across the electromagnetic spectrum from radio to VHE gamma-rays and their emission, in practically all bands, is modulated with a period equal to the orbital period. The variability of the ambient conditions as the emitter orbits around the young star provides a unique laboratory to test and improve our current understanding of particle acceleration, transport, emission and absorption in relativistic outflows.

Up to now, only three gamma-ray binaries have been clearly detected and identified: LS I +61 303 (Albert et al., 2006), LS 5039 (Aharonian et al., 2005b) and PSR B1259−63 (Aharonian et al., 2005a). The compact object powering PSR B1259−63 is known to be a young pulsar, the wind of which interacts with the dense stellar wind of the Be star and accelerates particles in the strong shocks developed in the pulsar wind. On the other hand, the nature of the compact objects harbored by LS 5039 and LS I +61 303 is yet unknown. The detection of pulsed emission from PSR B1259−63 has been possible due to its wide orbit, but in the case of LS 5039 and LS I +61 303 the proximity of the putative pulsar to the star would imply the free-free absorption of its pulsed radio emission. Therefore, a non-detection of radio pulses does not necessarily rule out the presence of a pulsar. See Section 1.3.1 below for a discussion of the proposed emission scenarios for LS 5039 and LS I +61 303.

In addition to these three binaries, there are two very strong candidates to enter the category of gamma-ray binaries. The first one is HESS J0632+057, a point-like VHE source located in the galactic plane with variable TeV, X-ray and radio emission (Hinton et al., 2009; Skilton et al., 2009, and references therein). The broadband variability and lack of extended VHE emission are compelling indications that HESS J0632+057 is a gamma-ray loud binary. Recent X-ray observations provided evidence of a ~320 day period (Falcone et al., 2011), and slightly extended emission at milliarcsecond scales (similar to that observed in other gamma-ray binaries) has been detected by Moldón et al. (2011).

The other candidate is 1FGL J1018.6−5856, from which a period of 16.6 days has already been detected in the HE gamma-ray band with *Fermi* (Corbet et al., 2011), and is compatible with the position of an O6V((f)) star, similar to the optical companion of LS 5039. Additionally, the HE gamma-ray source is coincident with an X-ray source that displays similar spectral properties

to other gamma-ray binaries (Pavlov et al., 2011). The source is also positionally compatible with the VHE source HESS J1023−575 (de Oña Wilhelmi et al., 2010), but it is not yet known whether the VHE source is variable. Additionally, the presence of a positionally coincident SNR prevents the clear identification of the VHE source with 1FGL J1018.6−5856.

The High-mass X-ray binary (HMXB) Cygnus X-3 has been recently detected as a variable, flaring source in the HE gamma-ray band both by *Fermi* (Abdo et al., 2009) and *AGILE* (Tavani et al., 2009). The identification of the HE gamma-ray source with Cygnus X-3 is irrefutable given the modulation of the gamma-ray flux with the orbital period of Cygnus X-3 detected by *Fermi*. This source has been extensively observed with MAGIC (Aleksić et al., 2010), but it has not resulted in a detection above 100 GeV. Previous attempts to detect it were based on either radio outbursts or the state of the source at soft or hard X-rays. The all-sky monitoring mode of *Fermi* can be exploited to obtain a near-real-time status of the source in HE gamma-rays. In Appendix B we show the results from an automatic analysis pipeline of *Fermi*/LAT GeV data developed to trigger MAGIC VHE observations during GeV flares of Cygnus X-3. If the source flares at VHE simultaneously to HE gamma-rays, this is the best way to detect such flares, and hopefully in the following years we will know whether Cygnus X-3 does indeed emit detectable radiation above 100 GeV.

Given the current debate on the nature of the compact objects harbored by LS 5039 and LS I +61 303, the detection of VHE emission from an accreting black hole source would be an extraordinary result. In 2007 the MAGIC collaboration found evidence of VHE emission from the microquasar Cygnus X-1 during a flare lasting ~80 min (Albert et al., 2007). However, the gamma-ray signal found was only significant at a 4.9σ level, that translated into a significance of 4.1σ when taking into account the data selection trials. The lack of independent or subsequent detection advises for precaution when considering the physical implications of this result.

1.3.1 Scenarios of VHE emission from gamma-ray binaries

There are currently two main scenarios invoked to explain the broadband emission from gamma-ray binaries: the microquasar and the pulsar binary scenarios.

X-ray binaries are binary systems formed by a star and a compact object which is either a neutron star or a black hole. The strong gravitational pull of the compact object attracts and accretes matter from the star, forming an accretion disk that is extremely bright in X-rays. Microquasars are a unique sub-

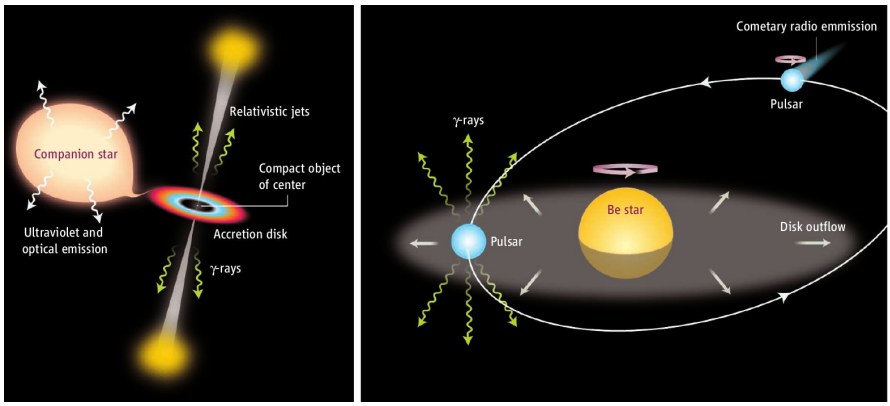

Figure 1.4: Sketch of the two considered scenarios for gamma-ray emission from binary systems. *Left*: the microquasar scenario. *Right*: the binary pulsar scenario. See text for an explanation of the properties of each scenario. Image from Mirabel (2006).

class of X-ray binaries because the accretion of matter onto the compact object triggers the formation of jets composed of plasma accelerated to relativistic velocities. They received their name after their similarity (albeit at scales several orders of magnitude smaller) with quasars. After their discovery by Mirabel et al. (1992) the importance of non-thermal processes was proven and the possibility of effective gamma-ray production at VHE through upscattering of the stellar photons was explored (Levinson & Blandford, 1996; Aharonian & Atoyan, 1998). Recently, a confirmation of the presence of particle populations accelerated up to GeV and higher energies was found in the detection by *AGILE* and *Fermi* of the HMXB Cygnus X-3 (Tavani et al., 2009; Abdo et al., 2009). The *AGILE* team also claimed the detection of flaring HE emission from Cygnus X-1 (Sabatini et al., 2010), but the relationship with Cygnus X-1 was not clear and no subsequent detection has been made.

The proposed microquasar scenario for emission at VHE involves the upscattering of stellar photons by the relativistic particle population accelerated either at the jet base or at recollimation shocks along the jet. The broadband variability of the source may be explained naturally as variability of the mass accretion rate onto the compact object and therefore jet power. The detection of elongated asymmetric emission in high-resolution radio images of LS 5039 was interpreted as mildly relativistic ejections from a microquasar jet and prompted its identification with an EGRET HE gamma-ray source (Paredes et al., 2000). The broadband emission from radio to VHE is developed in detail and applied to LS 5039 and LS I +61 303 by Bosch-Ramon

et al. (2006) and Paredes et al. (2006). A sketch of the scenario may be found in Figure 1.4, left. Note, however, that, for the depicted microquasar, accretion onto the compact object takes place through the so-called Roche lobe overflow mechanism, whereas for the powerful stellar winds of the stars in gamma-ray binaries accretion would be directly from the wind.

As many as 30 years ago, Maraschi & Treves (1981) already proposed the source of non-thermal emission from LS I +61 303 to be the relativistic wind of a pulsar interacting with the stellar wind, an idea subsequently developed upon by, e.g., Tavani & Arons (1997) and Kirk et al. (1999). The lack of accretion signatures in X-ray spectra and the detection of cometary-like, phase-dependent radio emission from LS I +61 303 (Dhawan et al., 2006) prompted the development of models to account for the non-thermal broadband emission of LS I +61 303 and LS 5039 in the pulsar binary scenario (Dubus, 2006). In this scenario, the wind from a young, rotationally powered pulsar interacts with the stellar wind. Particles are accelerated in the shock formed in the pulsar wind and radiate as they travel, possibly at relativistic velocities, along the bowshock-like contact discontinuity formed at the balance of the pulsar and stellar winds. These energetic particles then radiate from radio up to hard X-rays through synchrotron and at higher energies through the IC upscattering of stellar photons. The lower-energy electrons would end escaping the system and creating and asymmetric synchrotron nebula pointing away from the stellar companion, the shape of which would depend on the ram pressure ratio of the stellar and pulsar winds. At even larger distances from the source, extended X-ray emission has been detected in LS I +61 303 (Paredes et al., 2007), PSR B1259−63 (Pavlov et al., 2011) and LS 5039 (Durant et al., 2011), which could be equivalent to the large-scale PWNe found around some isolated pulsars.

1.4 The keV–TeV connection

For all non-thermal emitters there is an intrinsic synergy between the emission at X-ray energies and the emission in VHE gamma-rays. In the presence of a magnetic field, accelerated charged particles will radiate synchrotron emission. For moderate magnetic fields of below 1 G and an ambient radiation field with optical wavelength, as is the case for the emission from stars, the energy required for electrons to emit in the X-ray band (through synchrotron) and the VHE band (through Inverse Compton) is roughly similar. This means that the properties of this particular range of electron energies can be recovered through two different emission bands. Furthermore, emission in these bands may be modulated differently by ambient conditions: synchro-

tron will depend on the magnetic field while IC emission will vary according to the density of seed stellar photons, the geometry and angle of the emitter with respect to the observer, pair production absorption and electromagnetic cascading. These diverse modulations, however, may play advantageous for an understanding of the source since it allows not only to recover the parameters of the emitter but also verify the assumptions made on the system environment. A perfect complement to test the properties of the non-thermal particle population are radio observations, which probe the lower energy electrons that emit through synchrotron radiation. A welcome consequence of the synergy between X-ray and VHE emission in leptonic populations is that X-ray observations are often the best tool to identify the counterparts of unidentified VHE sources, mainly because of the less crowded X-ray sky (as opposed to, e.g., optical).

1.5 Overview of the thesis

Even though gamma-ray loud X-ray binaries have been widely studied, many key characteristics of these sources are still elusive. The unique environment they present and the influence between the different parts of the systems make it difficult to apply knowledge from other fields. While these binaries appear similar on the surface, many properties set them apart and it is clear that the same scenario may not be directly applicable to all of them.

The aim of the present thesis is to deepen our understanding of the hitherto detected gamma-ray binaries and search for new candidates. In all the work presented here we have exploited the keV-TeV connection in gamma-ray binaries through simultaneous X-ray/VHE observations or modeling of the broadband thermal and non-thermal emission from gamma-ray binaries. Here we give a brief overview of the topics covered in the following chapters.

High-energy emission processes

We begin the thesis with a brief explanation of the physical processes relevant to X-ray and VHE gamma-ray emission in Chapter 2. We consider interactions of high-energy particles and photons with the magnetic field (synchrotron, Section 2.2), with the ambient radiation field (Inverse Compton and pair production absorption, Section 2.3), and with the ambient matter (relativistic Bremsstrahlung, neutral pion decay and photoelectric absorption, Section 2.4)

Correlated X-ray/VHE emission from LS I +61 303

During a simultaneous X-ray (*XMM-Newton* and *Swift*/XRT) and VHE gamma-ray (MAGIC) campaign on LS I +61 303 we discovered a correlation between the emission in X-rays (0.3–10 keV) and VHE gamma-rays (>100 GeV). In Chapter 3 we describe the multiwavelength observations and results, as well as a brief physical interpretation of the result. In Chapter 4 we expand on the physical interpretation of the X-ray/VHE correlation and gain insight into the properties of the multiwavelength emitter through the development of a radiative model of emission and absorption. Additionally, in Appendix C we use the case of correlated X-ray/VHE emission from gamma-ray binaries to test the capabilities of the future CTA.

Thermal X-ray emission from pulsar gamma-ray binaries

The lack of a direct detection of the putative pulsars in the gamma-ray binaries LS I +61 303 and LS 5039 limits our understanding of these systems. Typically, only lower limits on the power of the pulsars can be inferred from energy budget considerations. In Chapter 5 we present a novel method to determine an upper limit to the pulsar spin-down luminosity through the study of the thermal X-ray emission from the shocked stellar wind. Given that the pulsar spin-down luminosity is one of the main factors that determine the shape of the interaction region between the stellar and pulsar winds, we can link the lack of thermal features in the soft X-ray spectra of gamma-ray binaries with an upper limit to the pulsar spin-down luminosity. We apply this model to LS 5039 and derive an upper limit close to the lower limit given by energetic efficiency required to emit the GeV spectrum detected by *Fermi*. Therefore, we successfully constrain the pulsar spin-down luminosity to a narrow range around a few times 10^{36} erg/s.

Search for VHE emission from Sco X-1

In May 2010 we performed a simultaneous X-ray/VHE campaign on the microquasar Sco X-1 to search for VHE emission. Sco X-1 is a so-called Z-source and its soft X-ray colors can be linked to the accretion states of the neutron star. In one of these states, known as Horizontal Branch, a powerful relativistic jet is launched. We used the simultaneous X-ray data from pointed observations with *RXTE*/PCA to do an accretion-state-based selection of the VHE data obtained with MAGIC. We did not obtain a significant signal in

any of the states. We discuss the possibilities of VHE emission from Sco X-1 and consider the constrains placed on the system by the measured upper limits.

References

Abdo, A. A., et al. 2007, ApJ, 664, L91
—. 2009, Science, 326, 1512
—. 2010, ApJS, 188, 405
Aharonian, F., et al. 2004a, Nature, 432, 75
—. 2004b, A&A, 425, L13
—. 2005a, A&A, 442, 1
—. 2005b, Science, 309, 746
—. 2006a, Nature, 439, 695
—. 2006b, A&A, 460, 365
—. 2006c, ApJ, 636, 777
—. 2007a, ApJ, 664, L71
—. 2007b, A&A, 467, 1075
Aharonian, F. A., & Atoyan, A. M. 1998, NewAR, 42, 579
Albert, J., et al. 2006, Science, 312, 1771
—. 2007, ApJ, 665, L51
Aleksić, J., et al. 2010, ApJ, 721, 843
Baade, W., & Zwicky, F. 1934, Physical Review, 46, 76
Bosch-Ramon, V., Romero, G. E., & Paredes, J. M. 2006, A&A, 447, 263
Corbet, R. H. D., et al. 2011, The Astronomer's Telegram, 3221
de Oña Wilhelmi, E., et al. 2010, in COSPAR, Plenary Meeting, Vol. 38, 38th COSPAR Scientific Assembly, 2803–+
Dhawan, V., Mioduszewski, A., & Rupen, M. 2006, in VI Microquasar Workshop: Microquasars and Beyond
Dubus, G. 2006, A&A, 456, 801
Durant, M., Kargaltsev, O., Pavlov, G. G., Chang, C., & Garmire, G. P. 2011, ApJ, in press. arXiv:1103.5166
Falcone, A., Bongiorno, S., Stroh, M., & Holder, J. 2011, The Astronomer's Telegram, 3152
Hartman, R. C., et al. 1999, ApJS, 123, 79
Hinton, J. A., et al. 2009, ApJ, 690, L101

Kirk, J. G., Ball, L., & Skjaeraasen, O. 1999, Astroparticle Physics, 10, 31

Levinson, A., & Blandford, R. 1996, ApJ, 456, L29+

Maraschi, L., & Treves, A. 1981, MNRAS, 194, 1

Mirabel, I. F. 2006, Science, 312, 1759

Mirabel, I. F., Rodriguez, L. F., Cordier, B., Paul, J., & Lebrun, F. 1992, Nature, 358, 215

Moldón, J., Ribó, M., & Paredes, J. 2011, The Astronomer's Telegram, 3180

Paredes, J. M., Bosch-Ramon, V., & Romero, G. E. 2006, A&A, 451, 259

Paredes, J. M., Martí, J., Ribó, M., & Massi, M. 2000, Science, 288, 2340

Paredes, J. M., Ribó, M., Bosch-Ramon, V., West, J. R., Butt, Y. M., Torres, D. F., & Martí, J. 2007, ApJ, 664, L39

Pavlov, G. G., Chang, C., & Kargaltsev, O. 2011, ApJ, 730, 2

Pavlov, G. G., Misanovic, Z., Kargaltsev, O., & Garmire, G. P. 2011, The Astronomer's Telegram, 3228

Sabatini, S., et al. 2010, The Astronomer's Telegram, 2715

Skilton, J. L., et al. 2009, MNRAS, 399, 317

Tavani, M., & Arons, J. 1997, ApJ, 477, 439

Tavani, M., et al. 2009, Nature, 462, 620

Vandenbroucke, J., et al. 2010, arXiv:1012.0849

Weekes, T. C., et al. 1989, ApJ, 342, 379

2

High-energy processes in binary systems

The observation of broadband emission from gamma-ray binaries can provide valuable information about the properties of the accelerator and emitter from which high-energy emission arises. However, a good understanding of the underlying radiation and absorption processes is paramount to successfully untangle the properties of the systems. In this chapter we present some of the acceleration, radiation and absorption processes that play an important role in the emission of HE and VHE gamma rays. We note that the chapter will not be an exhaustive review on high-energy processes, but only of those that have a particular importance in gamma-ray binaries. A more detailed account of other phenomena relevant to high-energy astrophysics may be found in Blumenthal & Gould (1970), Rybicki & Lightman (1979), Longair (1992, 1994), Aharonian (2004), and Vila & Aharonian (2009).

Most of the processes relevant to gamma-ray astronomy imply the interaction of accelerated particles (electrons, protons, and nuclei) with ambient targets such as cold gas, low-frequency photons or magnetic fields. For this reason, a convenient way to structure a description of high-energy radiation and absorption processes is to group them by the type of the target, as we do below.

In general, the cross-sections relevant to these processes are well known. The electromagnetic processes are well characterised by their calculation in

the framework of Quantum Electrodynamics, whereas most of our knowledge on the cross-sections of hadronic processes comes from accelerator data.

2.1 Definitions

The calculation of the photon spectrum emitted by a population of particles through a certain process requires the knowledge or calculation of the differential cross-section of the process and the energy distribution of the parent particles.

The differential cross-section $(\mathrm{d}\sigma/\mathrm{d}\Omega)$ of a given process can be thought of as the number of scattered particles per unit time per unit solid angle divided by the incident particle flux.

An integration of the differential cross-section over the scattered particle solid angle results in the total cross-section σ. The total cross-section is a measure of the probability of interaction independently of the direction of the scattered particles. A useful parameter to gauge the efficiency of a given process in a medium with a density n of target particles is the cooling time

$$t_{\mathrm{cool}} = (f\sigma nc)^{-1},$$

where f is the inelasticity of the process and is defined as the mean fractional energy loss per particle per interaction. It is worth noting that in general the cooling time will depend not only on the given process but also on the particle energy. The efficiency of a given process can be evaluated by comparing its cooling time with that of the competing processes of particle energy loss (radiative or non-radiative) and the dynamical times of the source.

The parent particle population may be described by its distribution in energy $N(E)$. The energy distribution is the number of particles per unit energy per unit volume, and in general will be time-dependent. The calculation of $N(E)$ is not trivial, and three approaches may be followed in order of increasing difficulty and self-consistency.

- The first approach is to simply assume a parent particle population and check whether the resulting emitted spectrum fits the data. This provides no information on the energy-loss mechanisms at play in the emitter or the acceleration process, so it may only be used as a probe of the relative efficiency of the different radiative processes. Its power for physical inference is thus quite limited.

- The second approach is to assume an injection spectrum of particles $Q(E, t)$. Given this injection spectrum, the evolved spectrum may be

calculated through the knowledge of the dominant radiative and non-radiative energy-loss processes in the emitter. From the evolved particle energy distribution $N(E)$, one can compute the emitted spectrum. A comparison with observational data will be able to provide information on both the emission processes and the energy-loss channels, but only moderate inference can be made about the acceleration mechanism. This approach is only valid if the emission and acceleration regions are different.

- The last and most accurate approach to obtain $N(E)$ is to compute the injection spectrum from the given acceleration mechanism thought to be at play in the source. From this injection spectrum, the evolved parent particle distribution and emission spectrum may be computed. This method provides the most inference power, but also requires a very good knowledge of the structure and physical properties of the accelerator and emitter regions of the source.

The evolution of the particle spectrum in the last approach above may be computed from the Fokker-Planck differential equation (see, e.g., Ginzburg & Syrovatskii, 1964), which takes into account transport of particles due to diffusion and convection as well as the acceleration of particles through first and second order Fermi-like mechanisms. This equation can be significantly simplified if the volume of the emitter is much larger than the site of efficient acceleration and results in

$$\frac{\partial N}{\partial t} = \frac{\partial}{\partial E}[PN] - \frac{N}{\tau_{\rm esc}} + Q, \tag{2.1}$$

where $N \equiv N(E,t)$ is the particle energy distribution, $P \equiv P(E) = -\mathrm{d}E/\mathrm{d}t = -E/t_{\rm cool}$ is the energy-loss rate per particle, $Q \equiv Q(E,t)$ is the injection spectrum, and $\tau_{\rm esc} \equiv \tau_{\rm esc}(E)$ is the escape time of particles from the source. A Green-function solution to Eq. (2.1) may be used for a general calculation (Ginzburg & Syrovatskii, 1964), but here we will consider the so-called steady state particle distribution. This implies the assumption that the total number of particles remain constant (i.e., $\partial N/\partial t = 0$) and that they continue to radiate as they lose energy, thus creating a stationary parent particle distribution. This assumption will not hold if the dynamical timescales of the source are shorter than the cooling times. If, in addition, we assume that the escape timescale is much larger that the energy-loss rate, the term containing $\tau_{\rm esc}$ can be discarded, so that Eq. (2.1) may be solved as

$$N(E) = \frac{1}{|\mathrm{d}E/\mathrm{d}t|}\int_E^\infty Q(E')\mathrm{d}E',$$

where the energy loss rate per particle $|\mathrm{d}E/\mathrm{d}t|$ will be the sum of the energy loss rates owing to all the relevant radiative and non-radiative energy loss processes in the emitter region. For a given injection power-law spectrum $Q(E) \propto E^{-\alpha}$, the resulting evolved particle spectrum is determined by the energy dependence of the energy loss term. If energy losses are proportional to the particle energy, $\mathrm{d}E/\mathrm{d}t \propto E$, as is the case for relativistic Bremsstrahlung and adiabatic losses, the evolved particle spectrum will reproduce the injected spectrum, $N(E) \propto E^{-\alpha}$. Dominant synchrotron radiation or Inverse Compton in the Thomson regime will result in a steeper particle distribution owing to their energy loss dependence $\mathrm{d}E/\mathrm{d}t \propto E^2$, which results in $N(E) \propto E^{-(\alpha+1)}$. On the other hand, the evolved spectrum will be harder for energy loss rates independent of particle energy or with a negative dependence, such as ionisation losses ($\mathrm{d}E/\mathrm{d}t$ not proportional to E) or Inverse Compton in the Klein-Nishina limit ($\mathrm{d}E/\mathrm{d}t \propto E^{-1}$), resulting in $N(E) \propto E^{-(\alpha-1)}$ and $N(E) \propto E^{-(\alpha-2)}$, respectively.

Once the parent particle population and cooling timescale of the process have been obtained, one can compute the total energy budget available from its energy distribution and the volume of the source as

$$W_{\mathrm{e,p}} = \int_V \int_{E_{\mathrm{min}}}^{E_{\mathrm{max}}} E N_{\mathrm{e,p}}(E) \mathrm{d}E \mathrm{d}V.$$

Given this energy budget, the resulting emitted radiation through a given process with cooling time t_{cool} would be

$$F \simeq \frac{W_{\mathrm{e,p}}}{4\pi d^2 t_{\mathrm{cool}}}.$$

However, this would only provide an estimate flux, and the only way to accurately compute the emitted spectrum is to perform the integration of the differential cross-sections over the parent and target particle populations

$$L(\epsilon) = \iiiint E N(E) c n(\epsilon_0) \frac{\mathrm{d}\sigma(E, \epsilon_0, \epsilon, \Omega)}{\mathrm{d}\Omega} \mathrm{d}\Omega \mathrm{d}\epsilon_0 \mathrm{d}E \mathrm{d}V,$$

where ϵ is the photon energy of the scattered radiation, and the target particle population is characterised by its energy ϵ_0 and density $n(\epsilon_0)$.

2.2 Interaction with the magnetic field

2.2.1 Synchrotron emission

Synchrotron emission is the radiation emitted by a charged accelerated particle located in an ambient magnetic field **B**. This channel of emission may ac-

count for the non-thermal power-law spectrum in many astrophysical sources from radio up to gamma-rays. The classical electromagnetic treatment of synchrotron radiation (e.g. Ginzburg & Syrovatskii, 1965) provides an accurate treatment for the moderate magnetic fields found in gamma-ray binaries. The charged particle will spiral around the direction of the magnetic field lines owing to the Lorentz forces. The centripetal acceleration will cause it to radiate at frequencies close to the characteristic frequency of the spiral. The girofrequency can be related to a characteristic energy, which for a particle of energy E and mass m is

$$E_{\rm c} = h\nu_c = \frac{3}{4\pi}\frac{heB\sin\alpha E^2}{m^3c^5}, \tag{2.2}$$

where α is the so-called pitch angle, i.e., the angle between the magnetic field and the direction of the particle. The spectral distribution of photons radiated by a single particle of energy E in an isotropic magnetic field is given by

$$P_{\rm sy}(E,\epsilon) = \frac{\sqrt{2}}{h}\frac{e^3B}{mc^2}F(x), \tag{2.3}$$

where $F(x) = x\int_x^\infty K_{5/3}(\xi)\,{\rm d}\xi$, $x = \epsilon/E_{\rm c}$, and ϵ is the energy of the emitted radiation; $K_{5/3}(\xi)$ is the modified Bessel function of order 5/3. A practical analytical form of the term $F(x)$ in Eq. (2.3) is $F(x) \approx 1.85x^{1/3}\exp(-x)$ (Melrose, 1980). The error incurred by making this simplification is less than a few percent up to photon energies of $10E_{\rm c}$, and will be used in calculations throughout this thesis. The synchrotron emissivity $P_{\rm sy}(E,\epsilon)$ presents a peak at $\epsilon \simeq 0.29E_{\rm c}$ with a sharp decline at higher energies. The dependency of the synchrotron characteristic energy and the cooling time on the charged particle mass implies that the process will be much more efficient for electrons than for proton owing to the mass ratio $m_e/m_p \simeq 1836$. In particular, the energy loss rate of protons will be $(m_p/m_e)^4 \simeq 10^{13}$ times slower, and their characteristic energy will be $(m_p/m_e)^3 \simeq 6\times10^9$ times lower than for electrons. For the ambient conditions of the emitter in gamma-ray binaries, we can assume that only electron synchrotron emission will be relevant.

The energy-loss rate of electrons owing to synchrotron radiation can be obtained through integration of Eq. (2.3) over ϵ, and is

$$-\left.\frac{{\rm d}E}{{\rm d}t}\right|_{\rm sy} = \frac{4}{3}\sigma_{\rm T}cu_{\rm mag}\frac{E^2}{(m_ec^2)^2}, \tag{2.4}$$

where $u_{\rm mag} = B^2/(8\pi)$ is the magnetic field energy density, and $\sigma_{\rm T} = 8\pi r_e^2/3$ is the Thomson cross-section. The cooling time for high-energy particles in a magnetic field can then be expressed as

$$t_{\rm sy} = \frac{3}{4}\frac{(m_e c^2)^2}{\sigma_{\rm T} c u_{\rm mag} E} \approx 4 \times 10^5 \, E_{\rm GeV}^{-1} B_{\rm G}^{-2} \ {\rm s}, \tag{2.5}$$

where $E_{\rm GeV}$ is the electron energy in units of 10^9 eV and $B_{\rm G}$ is the value magnetic field in Gauss.

The emission from a population of particles $N(E)$ may be computed by integrating Eq. (2.3) over the parent particle energy distribution,

$$L(\epsilon) = \int_{E_{\rm min}}^{E_{\rm max}} N(E) P_{\rm sy}(E, E_\gamma) {\rm d}E.$$

A power-law distribution of particles with an exponential cutoff, described by $N(E) \propto E^{-\alpha} \exp[-(E/E_0)]$, where E_0 is the cutoff energy, will give rise to the following emitted spectrum

$$L(\epsilon) \propto \epsilon^{-\frac{\alpha-1}{2}} \exp\left[-(\epsilon/\epsilon_{\rm max})^{1/2}\right],$$

where $\epsilon_{\rm max} = 0.29 E_{\rm c}(E_0)$.

At lower energies self absorption should be taken into account to compute synchrotron emission. In the optically thick regime, the emitted spectrum will be $L(\epsilon) \propto \epsilon^{5/2}$. However, in the present thesis only energies above X-rays will be considered, so the reader is referred to, e.g., Pacholczyk (1970) for a detailed treatment of the optically thick case.

2.3 Interaction with the radiation field

2.3.1 Inverse Compton Scattering

Compton scattering is the process through which high-energy photons collide with stationary or slow-moving electrons and transfer part of their energy and momentum to the electrons. The inverse scenario, where the electron has a higher momentum than the photon and the photon energy is increased through the interaction, is called IC and is of profound importance in high-energy astrophysics. IC provides a way to transfer energy from the accelerated populations of ultrarelativistic electrons to the ambient photon field and thus originate very high energy emission up to tens of TeV.

The angle-averaged total cross-section of inverse Compton scattering depends only on the product $\kappa_0 = \epsilon_0 \gamma$, where ϵ_0 is the energies of the interacting

photon and γ the energy of the electron, both in units of $m_e c^2$. In the non-relativistic regime ($\kappa_0 \ll 1$), the IC cross-section will approach the Thomson cross-section as $\sigma_{\rm IC} \approx \sigma_{\rm T}(1 - 2\kappa_0)$. In the ultrarelativistic regime ($\kappa_0 \gg 1$), known as Klein-Nishina regime, the cross-section decreases with the particle energy as $\sigma_{\rm IC} \approx (3/8)\sigma_{\rm T}\kappa_0^{-1}\ln(4\kappa_0)$. A useful expression for the IC cross-section with an accuracy better that 10% in a broad range of κ_0 is given by Coppi & Blandford (1990):

$$\sigma_{\rm IC} = \frac{3\sigma_{\rm T}}{8\kappa_0}\left[\left(1 - \frac{2}{\kappa_0} - \frac{2}{\kappa_0^2}\right)\ln(1+2\kappa_0) + \frac{1}{2} + \frac{4}{\kappa_0} - \frac{1}{2(1+2\kappa_0)^2}\right].$$

The energy distribution of the scattered photons may be computed from the IC differential cross-section. We can consider the case where a population of isotropically distributed electrons upscatter a directed low-energy photon beam with number density n_{ϵ_0}. The spectrum of radiation scattered at an angle $\theta_{\rm IC}$ relative to the initial photon beam is (Aharonian & Atoyan, 1981)

$$\frac{\partial^2 N(\theta_{\rm IC}, \epsilon)}{\partial\epsilon\partial\Omega} \simeq \frac{3}{16\pi} c\sigma_{\rm T} \int_{\epsilon_{0,m}(\gamma,\theta_{\rm IC})} \frac{n_{\epsilon_0}}{\epsilon_0\gamma^2} f(\epsilon, \epsilon_0, \theta_{\rm IC}, \gamma)\, {\rm d}\epsilon_0, \tag{2.6}$$

where ϵ is the energy of the scattered photon in units of $m_e c^2$,

$$\epsilon_{0,m}(\gamma, \theta_{\rm IC}) = \frac{\epsilon}{2(1 - \cos\theta_{\rm IC})\gamma^2[1 - \epsilon/\gamma]},$$

is the minimum seed photon energy for an electron of energy γ to upscatter it up to an energy ϵ, and

$$f(\epsilon, \epsilon_0, \theta_{\rm IC}, \gamma) = 1 + \frac{z^2}{2(1-z)} - \frac{2z}{b_\theta(1-z)} + \frac{2z^2}{b_\theta^2(1-z)^2}, \tag{2.7}$$

where $b_\theta = 2(1-\cos\theta_{\rm IC})\kappa_0$ and $z = \epsilon/\gamma$. Equation (2.6) provides an accuracy better than 3% for $\epsilon \gg \epsilon_0$ and $\gamma \gg 1$. For a given seed photon distribution, the shape of the resulting emitted spectrum only depends on the parameter b_θ and the relativistic electron energy distribution.

As can be seen from the definition of b_θ and Eqs. (2.6) and (2.7), the upscattering of a directed photon beam is notably anisotropic. This will have an important effect in the calculation of IC emission from astrophysical sources where the seed photons are originated in a compact source. This will be the case in gamma-ray binaries, where the dominant radiation field is the black body emission from the young star. The movement of the compact object and, presumably, the emitter, around the companion star is a source of modulation of the angle $\theta_{\rm IC}$ that is necessary to take into account when computing the IC emission from these sources. As can be seen in Figure 2.1, IC

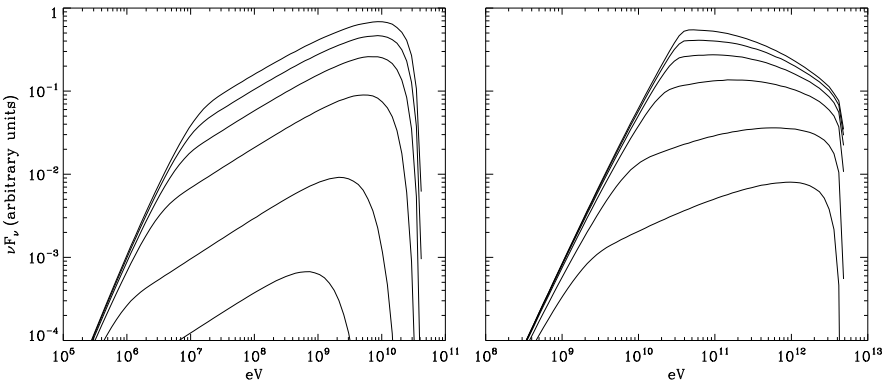

Figure 2.1: Inverse Compton spectra for different values of the interaction angle $\theta_{\rm IC}$. The scattered spectra were computed from an $\alpha = 2$ power-law electron distribution and considering a blackbody seed photon distribution at temperature $kT = 1$ eV. The left panel shows the variation for interactions the Thomson regime (electron energy $10^3 < E/(m_e c^2) < 10^5$) and the right panel for interactions in the Klein-Nishina regime (electron energy $10^5 < E/(m_e c^2) < 10^7$). The shown interaction angles are $\theta_{\rm IC} = 15^\circ$ (bottom), 30°, 60°, 90°, 120° and 180° (top). Figure adapted from Dubus et al. (2008).

emission is higher when the interaction takes place head-on ($\theta_{\rm IC} = \pi$) and decreases for decreasing values of $\theta_{\rm IC}$. The angular dependence is stronger at lower energies when the interaction is in the Thomson regime, whereas in the Klein-Nishina regime the angular dependence is much weaker.

For the case of an isotropic seed photon distribution and a power law distribution of electrons with index α, Eq. (2.6) can integrated over $\theta_{\rm IC}$ and the parent electron energy distribution to obtain the isotropic scattered photon spectrum. For this case, the emitted spectrum will be a power-law with photon index $(\alpha+1)/2$ in the non-relativistic regime ($\kappa_0 \ll 1$) and a steeper spectrum, proportional to $\epsilon^{-(\alpha+1)}(\ln 4\kappa_0 + \text{const})$, in the ultrarelativistic regime ($\kappa_0 \gg 1$). The integration of the emitted spectrum for the interaction of relativistic electrons with a monoenergetic photon field of energy ϵ_0 and density $n_{\rm ph}$ yields the total energy-loss rate of the electrons (Aharonian & Atoyan, 1981):

$$-\left.\frac{{\rm d}E}{{\rm d}t}\right|_{\rm IC} = \frac{3\sigma_{\rm T} c n_{\rm ph}}{4\epsilon_0 b}\left[\left(6+\frac{b}{2}+\frac{6}{b}\right)\ln(1+b) - \ln^2(1+b) - 2{\rm Li}\left(\frac{1}{1+b}\right) - \frac{(11/12)b^3+8b^2+13b+6}{(1+b)^2}\right],$$

where $\mathrm{Li}(x) = \int_x^0 y^{-1}\ln(1-y)\mathrm{d}y$, and $b = 4\kappa_0$. The energy-loss rate expression reduces to the well known expressions in the Thomson regime

$$-\left.\frac{\mathrm{d}E}{\mathrm{d}t}\right|_{\mathrm{IC,Th}} \approx \frac{4}{3}\sigma_{\mathrm{T}} c u_{\mathrm{rad}} \gamma^2, \tag{2.8}$$

where $u_{\mathrm{rad}} = \epsilon_0 n_{\mathrm{ph}}$ is the radiation energy density, and in the Klein-Nishina regime

$$-\left.\frac{\mathrm{d}E}{\mathrm{d}t}\right|_{\mathrm{IC,KN}} \approx \frac{3}{8}\frac{\sigma_{\mathrm{T}} m_e^2 c^5}{\epsilon_0} n_{\mathrm{ph}}(\ln b - 11/6). \tag{2.9}$$

The different dependence the energy-loss rates have on the electron energy have implications on the shape of the steady-state electron spectrum for dominant IC losses. Whereas in the Thomson regime the energy loss-rate is proportional to γ^2, the loss-rate is almost energy independent in the Klein-Nishina regime. In the former, the electron spectrum will become steeper, whereas in the latter case it will become harder.

The comparison of Eqs. (2.4) and (2.8) shows that the energy loss rates owing to synchrotron and IC in the Thomson regime are equivalent when interchanging the energy density of the magnetic field u_{mag} and of the radiation field u_{rad}. For gamma-ray sources where radiation is dominated by a leptonic accelerated population, this provides a powerful tool to probe the magnetic field in the emitter. Given that $L \propto |\mathrm{d}E/\mathrm{d}t|$, the ratio of observed gamma-ray and X-ray luminosities corresponds to the ratio of radiation and magnetic field energy densities, i.e,

$$\frac{L_\gamma}{L_{\mathrm{X}}} \simeq \frac{u_{\mathrm{rad}}}{u_{\mathrm{mag}}} = 8\pi u_{\mathrm{rad}} B^{-2}.$$

In gamma-ray binaries the only unknwon quantity required to obtain the magnetic field of the emitter is its distance from the star. In other sources where the seed photon field for IC emission is the cosmic microwave background (CMB), such as most plerions, the radiation energy density is universal, $u_{\mathrm{CMB}} = 0.25\,\mathrm{eV/cm^{-3}}$, and the magnetic field can be directly inferred.

2.3.2 Photon-photon pair production

The intense radiation field found in gamma-ray binaries can also absorb VHE gamma-ray emission through pair production $\gamma\gamma \rightarrow \mathrm{e}^+\mathrm{e}^-$ (Gould & Schréder, 1967). The differential opacity for an emitted gamma-ray of energy ϵ is given by

$$\mathrm{d}\tau_{\gamma\gamma} = (1-\cos\psi)\sigma_{\gamma\gamma} n_{\epsilon_0}\,\mathrm{d}l\,\mathrm{d}\epsilon_0, \tag{2.10}$$

where l is the distance along the line-of-sight, ϵ_0 is the energy of the target photon, ψ is the interaction angle and the absorption cross section can be represented in the form:

$$\sigma_{\gamma\gamma} = \frac{\pi r_e^2}{2}(1-\beta^2)\left[2\beta(\beta^2-2) + (3-\beta^4)\ln\left(\frac{1+\beta}{1-\beta}\right)\right], \tag{2.11}$$

where $\beta = (1-1/s)^{1/2}$, and $s = \epsilon\epsilon_0(1-\cos\psi)/2$. The cross section maximum takes place for $s \simeq 3.5$, with a value of $\sigma_{\gamma\gamma} \simeq 0.2\sigma_{\rm T}$, and then decreases for $s \gg 1$ approximately as $\sigma_{\gamma\gamma} \propto s^{-1}\ln(s)$. Pair production can only occur for $s > 1$, when the centre of mass energy of the incoming photons is sufficiently high to create an electron positron pair. Therefore, for a head-on collision, the energy threshold above which pair production will act is $\epsilon_{\rm TeV} \approx 0.26\epsilon_{0,\rm eV}$, where $\epsilon_{\rm TeV}$ is the gamma-ray photon energy in TeV and $\epsilon_{0,\rm eV}$ the target photon energy in eV. We can see that for stellar target photons of a few eV the pair production energy threshold will bwill bearound 100 GeV.

The energy dependent gamma-ray attenuation factor owing to pair production may be computed as $\exp[-\tau_{\gamma\gamma}(\epsilon)]$. The optical depth $\tau_{\gamma\gamma}(\epsilon)$ is the result of the integration of the differential opacity (Eq. 2.10) over the target photon energy distribution and line-of-sight path.

It is worth noting that pair production opacity is not only significant in environments with dense radiation fields, such as binary systems, but also when radiation travels long distances in an relatively faint ambient radiation field. The gamma-ray photons emitted by distant AGNs interact with the Extragalactic Background Light (EBL), which consists in the optical light from stars and the infrared emission from dust, eventually precluding the detection of gamma-ray emitting AGNs at high redshifts.

The pairs generated through pair production absorption retain the high energy of the original photon. If synchrotron losses are dominant, i.e., the magnetic field is strong, they will rapidly radiate their energy through synchrotron radiation. If, on the other hand, the magnetic field is low, they may interact with the radiation field through IC and generate another high-energy gamma-ray, albeit of lower energy than the original one. This process could repeat itself until the energy of the secondary gamma-ray is below the pair production threshold and is known as electromagnetic cascading (Aharonian & Vardanian, 1985). The impact of efficient electromagnetic cascading on the emitted spectrum consists of a redistribution of a fraction of the emitted luminosity in the range $\epsilon \gtrsim 100\,$GeV into lower energies, mainly down to the order of 1 GeV but also in the X-ray domain as synchrotron radiation.

2.4 Interaction with matter

2.4.1 Relativistic Bremsstrahlung

When a charged particle is accelerated, it radiates. In the case of synchrotron radiation the origin of the acceleration is the Lorentz force, but charged particles may also be accelerated by the electrostatic forces of neighboring atoms and ions. When considering a relativistic electron moving through a medium of non-relativistic ions, the emission from a relativistic electron of energy E may be computed through the Bremsstrahlung cross-section (see, e.g., Heitler, 1954)

$$\sigma_{\rm Br}(E,\epsilon) = 4\alpha r_e^2 Z^2 \frac{{\rm d}\epsilon}{E} F(E,\epsilon),$$

where, for the case of a bare nucleus,

$$F(E,\epsilon) = \left[1 + \left(1-\frac{\epsilon}{E}\right)^2 - \frac{2}{3}\left(1-\frac{\epsilon}{E}\right)\right]\left[\ln\left(\frac{2E(E-\epsilon)}{m_e c^2 \epsilon}\right) - \frac{1}{2}\right],$$

and, for the case of a fully screened nucleus,

$$F(E,\epsilon) = \left[1 + \left(1-\frac{\epsilon}{E}\right)^2\right]\ln\left(\frac{191}{Z^{1/3}} - \frac{1}{2}\right) + \left(1-\frac{\epsilon}{E}\right)\left[-\frac{2}{3}\left(1-\frac{\epsilon}{E}\right)\right],$$

where ϵ is the energy of the emitted photon, r_e is the classical electron radius and Z is the atomic number of the nucleus. Even though the bremsstrahlung cross-section presents a singularity at $E \to 0$, bremsstrahlung losses are essentially catastrophic and the high-energy electron will radiate all its energy in the first interaction. However, for the sake of the calculation of the evolution of the energy distribution of the particle population, a continuous average energy loss rate may be computed as

$$-\left.\frac{{\rm d}E}{{\rm d}t}\right|_{\rm br} = 4Z^2 r_e^2 \alpha c n E\left[\ln\left(\frac{2E_e}{m_e c^2}\right) - \frac{1}{3}\right],$$

and

$$-\left.\frac{{\rm d}E}{{\rm d}t}\right|_{\rm br} = 4Z^2 r_e^2 \alpha c n E\left[\ln\left(\frac{183}{Z^{1/3}}\right) - \frac{1}{18}\right],$$

for the case of bare nucleus and completely screened nucleus, respectively.

2.4.2 Neutral pion decay

The radiation process from which we can gain a better insight of the hadronic component of relativistic particle populations is neutral pion decay. The interaction of relativistic protons and nuclei with the ambient gas results in the production of secondary pions, kaons and hyperions. The main channel of conversion of proton kinetic energy to gamma rays is the production of neutral pions, for which there is a proton kinetic energy threshold of $E_{\rm th} = 2m_\pi c^2(1 + m_\pi/4m_{\rm p}) \approx 280\,{\rm MeV}$. At high energies, the interaction may result equiprobably in any of the following reactions

$$p + p \to p + p + a\pi^0 + b(\pi^+ + \pi^-)$$
$$p + p \to p + n + \pi^+ + a\pi^0 + b(\pi^+ + \pi^-)$$
$$p + p \to n + n + 2\pi^+ + a\pi^0 + b(\pi^+ + \pi^-),$$

where a and b are integers. Charged pions decay into muons which eventually decay into electron-positron pairs and neutrinos. These secondary pairs may also contribute to the emitted spectrum through bremsstrahlung, synchrotron or IC emission. The resulting neutral pions π^0 have a mean lifetime of 8.4×10^{-17} s, and decay with a probability of 98.8% into two photos: $\pi^0 \to \gamma + \gamma$. The decay spectrum of a monoenergetic distribution of π^0 is flat and centered around $\epsilon = 0.5m_\pi c^2 \approx 67.5\,{\rm MeV}$. For a given proton energy distribution density $N_{\rm p}(E_{\rm p})$, the resulting gamma-ray emissivity (radiation output per unit volume) is given by (Aharonian & Atoyan, 2000)

$$q(\epsilon) = 2\int_{E_{\rm min}}^{\infty} \frac{q_\pi(E_\pi)}{\sqrt{E_\pi^2 - m_\pi^2 c^4}} {\rm d}E_\pi,$$

where $E_{\rm min} = \epsilon + m_\pi^2 c^4/4E_\pi$, and $q_\pi(E_\pi)$ is the π^0-emissivity

$$q_\pi(E_\pi) = cn_{\rm H}\int \delta(E_\pi - \kappa_\pi E_{\rm kin})\sigma_{\rm pp}(E_{\rm p})N_{\rm p}(E_{\rm p}){\rm d}E_{\rm p}$$
$$= \frac{cn_{\rm H}}{\kappa_\pi}\sigma_{\rm pp}\left(m_{\rm p}c^2 + \frac{E_\pi}{\kappa_\pi}\right)N_{\rm p}\left(m_{\rm p}c^2 + \frac{E_\pi}{\kappa_\pi}\right),$$

where $n_{\rm H}$ is the density of the target ambient nuclei, κ_π is the mean fraction of the kinetic energy of the proton ($E_{\rm kin} = E - m_{\rm p}c^2$) transfered to the secondary leading pion per collision. The total cross-section $\sigma_{\rm pp}(E)$ can be estimated for $E_{\rm kin} \geq 1\,{\rm GeV}$ as

$$\sigma_{\rm pp}(E) \approx 30[0.95 + 0.06\ln(E_{\rm kin}/1\,{\rm GeV})]\,{\rm mb}.$$

The values of the cross-section ($\sigma_{\rm pp} \approx 40\,{\rm mb}$) and inelasticity ($f \approx 0.45$) of pp interactions do not significantly change in a broad energy range from

a few GeV to hundreds of TeV, so the cooling timescale will be energy independent and of the order of (Aharonian & Atoyan, 1996)

$$t_{\rm pp} = (ncf\sigma_{\rm pp})^{-1} \approx 6 \times 10^{-7} (n_{\rm H}/1\,{\rm cm}^{-3})\,{\rm yr}.$$

The energy-loss rate can be derived from the above cooling time as

$$-\left.\frac{{\rm d}E}{{\rm d}t}\right|_{\rm pp} = \frac{E}{t_{\rm pp}}.$$

For low gas densities, such as the one of the interstellar medium (ISM), $n_{\rm H} \leq 1\,{\rm cm}^{-3}$, the proton lifetime will be longer than the dynamical timescales of most known astrophysical accelerators. However, for dense regions, such as molecular clouds with $n_{\rm H} \sim 10^2$–$10^4\,{\rm cm}^{-3}$, a significant fraction of the accelerator power could be radiated as gamma-rays through pp interactions.

2.4.3 Photoelectric absorption

While not properly a high-energy process, photoelectric absorption is the main interaction process of photons with matter at low energies, $\epsilon \ll m_e c^2$. A photon interacting with an atom can free bound electrons if its energy is larger than their ionising energy. The highest probability of interaction is for photons with the same energy as the ionising energy of a given electron shell, and decreases as ϵ^{-3} above it, so the cross-section presents so-called absorption edges at the ionising energies of the electron shells. The total absorption cross-section depends on the element abundance of the matter and its state of ionisation. For cold, solar abundance matter, the optical depth to photoelectric absorption may be approximated as (Longair, 1992)

$$\tau_{\rm ph}(\epsilon) \simeq 2 \times 10^{-26} \left(\frac{\epsilon}{1\,{\rm keV}}\right)^{-\frac{8}{3}} N_{\rm H},$$

where $N_{\rm H}$ is the neutral hydrogen column density and corresponds to the integration of the neutral hydrogen density over the line-of-sight path. The strong dependence of the optical depth on the photon energy indicates that its effect above ~1 keV will be very limited. However, it will play an important role in the X-ray observations of gamma-ray binaries presented in the following chapters given that, typically, soft X-ray observations are performed in the range 0.2–10 keV.

2.5 Particle acceleration

The radiation of the very hot matter found in some astrophysical scenarios, such as accretion discs, will only reach photon energies of up to a few hun-

dreds of keV. The fact that gamma-ray radiation at energies above 1 MeV has been detected from an ever-growing number of sources indicates the existence of a physical process that may accelerate particles much beyond the thermal tail.

The most common process of particle acceleration in astrophysical sources is the so-called Fermi or diffusive shock mechanism. Here we will briefly sketch its properties, and deeper treatments of this and other relevant acceleration mechanisms may be found in the works by, e.g., Scott & Chevalier (1975), Bell (1978a,b), Drury (1983), Derishev et al. (2003), and Rieger & Duffy (2004).

The basic requirement for particle acceleration through the diffusive shock mechanism is the presence of a shock moving through the upstream or unshocked medium. High-energy particles scatter off the turbulent magnetic fields on both sides of the shock and may diffuse through the shock several times. In each shock traversal the particle will gain an energy of the order of $\Delta E/E \approx u/c$, where u is the upstream material velocity in the reference frame of the shock. In each cycle there is a finite probability that the particles escape into the downstream flow, thus creating a power-law distribution of accelerated particles, $Q(E) \propto E^{-\alpha}$, with $\alpha \approx (r+2)/(r+1)$, where r is the compression factor of the shock. For strong shocks, $r = 4$ and $\alpha \approx 2$. The maximum acceleration energy will be determined either by the radiative losses of the particles in the accelerator or the finite lifetime of the shock. This mechanism corresponds to the so-called first order Fermi acceleration, while in the case that particles also increase their energy through scattering on the upstream medium particles it is known as second order Fermi acceleration. This acceleration mechanism is effective in accelerating particles up to very high energies, but only when the initial energy of the particles is already beyond the thermal tail. Otherwise, the chance of diffusing through the shock in the first place is very low. Progress has been recently made to overcome this problem in diffusive shock acceleration through numerical simulations (see, e.g., Kirk & Dendy, 2001, for a review). However, this does not pose an energy budget problem on high energy emission given that practically all the energy of accelerated particles is provided by the shock.

The precise knowledge of the acceleration rate requires a numerical modeling of the acceleration mechanism, and the shape at the high-energy cutoff is particularly sensitive to the mechanism, the energy losses, and the diffusion coefficient. However, it is possible to do a quite robust estimate of the cutoff energy E_0 from the balance of the radiative and non-radiative cooling

timescales and the acceleration time. The particle acceleration time can be parametrized as follows

$$t_{\rm acc} = \eta(E)\frac{E}{ecB_\perp}, \tag{2.12}$$

where $\eta(E) \geq 1$ gauges the effectiveness of acceleration and $E/(ecB_\perp)$ is the maximum energy gain rate allowed by classical electrodynamics. For the case of diffusive shock acceleration in a non-relativistic shock, the parameter $\eta(E)$ is related to the shock properties as

$$\eta \approx 10\frac{D(E)}{r_g c}\left(\frac{c}{v_s}\right)^2 \approx \frac{10}{3}\left(\frac{c}{v_s}\right)^2,$$

where $D(E)$ is the diffusion coefficient, $r_g = E/(eB_\perp)$ is the particle gyroradius, and v_s is the shock velocity. In the last equality, diffusion in the Bohm regime has been assumed, for which $D(E) = r_g c/3$.

The electron cutoff energy can then be found from the balance of Eq. (2.12) with the cooling time of the dominant process at high energies, i.e., $t_{\rm acc}(E_0) = t_{\rm cool}(E_0)$. We will consider the possibilities that the dominant process at high energies is synchrotron, IC or adiabatic losses, and derive the cutoff energy.

Synchrotron The cooling timescale of electrons through synchrotron radiation at very high energies can be described by Eq. (2.5), and from the balance with Eq. (2.12) results the following electron cutoff energy for synchrotron dominated cooling

$$E_0^{\rm sy} = \left(\frac{3}{2}\right)^{\frac{3}{4}}\frac{m_e^2 c^4}{\sqrt{\eta e^3 B}} \approx 60(\eta B_{\rm G})^{-1/2}\ {\rm TeV}, \tag{2.13}$$

where $B_{\rm G}$ is the magnetic field in Gauss. It is also interesting to note that the emitted synchrotron spectrum maximum energy does not depend on the ambient magnetic field, as can be seen by introducing Eq. (2.13) into Eq. (2.2), and results in

$$\epsilon_{\rm max}^{\rm sy} = \frac{9}{4}\frac{m_e c^2}{\alpha\eta},$$

where $\alpha = e^2/\hbar c \approx 1/137$ is the fine-structure constant. The synchrotron radiation cutoff $\epsilon_{\rm max}^{\rm sy}$ will, however, depend on η as $\epsilon_{\rm max}^{\rm sy} \approx 100(\eta/10^3)^{-1}$ keV, and thus will provide valuable information on the efficiency of the accelerator.

Inverse Compton For very intense ambient radiation fields and low magnetic fields, IC losses may dominate over synchrotron losses at high energies. The cooling time for IC losses in the Klein-Nishina regime can be derived from Eq. (2.9) and written as (Khangulyan et al., 2007)

$$t_{\rm IC,KN} \approx 7 \times 10^3 u_0^{-1} E_{\rm TeV}^{0.3}\ s,$$

where u_0 is the energy density of the target photons in units of erg/cm^3, and $E_{\rm TeV}$ the particle energy in TeV. The corresponding maximum electron energy is then

$$E_0^{\rm IC} = 9 \times 10^5 \left(\frac{B}{u_0}\right)^{3.3} \left(\frac{\eta}{10^3}\right)^{-3.3}\ {\rm TeV}.$$

The unusual dependence of the maximum energy on the factor B/u_0 is a result of the scattering taking place deep in the Klein-Nishina regime.

Non-radiative losses In general, non-radiative losses are characterized by their cooling timescale. In the case of adiabatic losses, it will be energy independent and may be interpreted as $t_{\rm ad} = R/v_{\rm exp}$, where R is the typical size of the emitter and $v_{\rm exp}$ its expansion velocity. For escape losses, the cooling time is the time particles take to escape from the source. However, it must be noted that in general both the adiabatic and escape losses are not most efficient in the accelerator region but in the emitter region, so they will not affect so much the acceleration of particles. The following electron maximum energy can then be taken as a lower limit

$$E_0^{\rm ad,esc} \approx 9 B_{\rm G} \eta^{-1} t_{\rm ad,esc}\ {\rm TeV}.$$

References

Aharonian, F. A. 2004, Very high energy cosmic gamma radiation : a crucial window on the extreme Universe (River Edge, NJ: World Scientific Publishing)

Aharonian, F. A., & Atoyan, A. M. 1981, Ap&SS, 79, 321

—. 1996, A&A, 309, 917

—. 2000, A&A, 362, 937

Aharonian, F. A., & Vardanian, V. V. 1985, Ap&SS, 115, 31

Bell, A. R. 1978a, MNRAS, 182, 147

—. 1978b, MNRAS, 182, 443

Blumenthal, G. R., & Gould, R. J. 1970, Reviews of Modern Physics, 42, 237

Coppi, P. S., & Blandford, R. D. 1990, MNRAS, 245, 453

Derishev, E. V., Aharonian, F. A., Kocharovsky, V. V., & Kocharovsky, V. V. 2003, Phys. Rev. D, 68, 043003

Drury, L. O. 1983, Reports on Progress in Physics, 46, 973

Dubus, G., Cerutti, B., & Henri, G. 2008, A&A, 477, 691

Ginzburg, V. L., & Syrovatskii, S. I. 1964, The Origin of Cosmic Rays (New York: Macmillan)

—. 1965, ARA&A, 3, 297

Gould, R. J., & Schréder, G. P. 1967, Physical Review, 155, 1404

Heitler, W. 1954, Quantum theory of radiation (Oxford: Clarendon)

Khangulyan, D., Hnatic, S., Aharonian, F., & Bogovalov, S. 2007, MNRAS, 380, 320

Kirk, J. G., & Dendy, R. O. 2001, Journal of Physics G Nuclear Physics, 27, 1589

Longair, M. S. 1992, High energy astrophysics. Vol. 1: Particles, photons and their detection (Cambridge, UK: Cambridge University Press)

—. 1994, High energy astrophysics. Vol. 2: Stars, the galaxy and the interstellar medium (Cambridge, UK: Cambridge University Press)

Melrose, D. B. 1980, Space Sci. Rev., 26, 3

Pacholczyk, A. G. 1970, Radio astrophysics. Nonthermal processes in galactic and extragalactic sources (San Francisco: Freeman)

Rieger, F. M., & Duffy, P. 2004, ApJ, 617, 155

Rybicki, G. B., & Lightman, A. P. 1979, Radiative processes in astrophysics (New York: Wiley-Interscience)

Scott, J. S., & Chevalier, R. A. 1975, ApJ, 197, L5

Vila, G. S., & Aharonian, F. A. 2009, in AAABS, Vol. 1, Compact Objects and their Emission, ed. Romero, G. E. and Benaglia, P.

3

Correlated X-ray and Very High Energy emission in the gamma-ray binary LS I +61 303

3.1 Introduction

LS I +61 303 is one of the few X-ray binaries (with PSR B1259−63, LS 5039, and HESS J0632+057, see Section 1.3) that have been clearly detected in very high energy (VHE) gamma rays. This source is a high-mass X-ray binary located at a distance of 2.0 ± 0.2 kpc (Frail & Hjellming, 1991) and contains a compact object with a mass between 1 and 4 $M_\odot$ orbiting the main Be star every 26.4960 ± 0.0028 d (Gregory, 2002) in an eccentric orbit (see Aragona et al., 2009, and Fig. 4.1). The B0 Ve star has a mass of $M_\star = (12.5 \pm 2.5)\, M_\odot$, a radius of $R_\star \approx 10\, R_\odot$ and a bolometric luminosity of 10^{38} erg s^{-1} (Casares et al., 2005). As most Be stars, it is though to present a decretion disc, which may be thought of as a dense, slow equatorial wind, that could account for up to half of the mass loss rate of the star. Observations of persistent jet-like features in the radio domain at ~100 milliarcsecond (mas) scales prompted a classification of the source as a microquasar (Massi et al. 2004; see also Massi & Kaufman Bernadó 2009 for a radio spectral discussion), but later observations at ~1–10 mas scales, covering a whole orbital period, revealed a rotating elongated feature that was interpreted as the interaction between a pulsar wind

and the stellar wind (Dhawan et al., 2006). In the X-ray domain, LS I +61 303 shows an orbital periodicity (Paredes et al., 1997) with quasi-periodic outbursts in the phase range 0.4–0.8. The source also shows short-term flux and spectral variability on time scales of kiloseconds (Sidoli et al., 2006; Rea et al., 2010). LS I +61 303 has been detected in the VHE domain by MAGIC (Albert et al., 2006) and VERITAS (Acciari et al., 2008). It shows a periodic behaviour (Albert et al., 2009) with maxima occurring around phase 0.6–0.7 and non-detectable flux around periastron ($\phi_{\rm per}$ = 0.275). However, it must be noted that since the beginning of 2008 there have been no reports of VHE detection around apastron even though VERITAS performed several observation campaigns (Holder, 2010). A recent detection of the source around periastron (Ong et al., 2010) indicates that its VHE orbital light curve might not be stable over long periods. LS I +61 303 was also detected by the high-energy (HE) gamma-ray instrument *Fermi*/LAT (Abdo et al., 2009). Its emission at GeV energies was found to be roughly anti-correlated in phase with the X-ray and VHE emission and presented a spectrum compatible with a power law and an exponential cutoff at ~6 GeV. This spectrum is reminiscent of pulsar magnetospheric emission, but no pulsations were found and no orbital variability would in principle be expected from this kind of emission. Since March 2009 the source shows a higher phase-averaged flux than before and the orbital modulation has significantly diminished (Dubois, 2010). This change in GeV behaviour, as well as the change in the VHE light curve, indicates that a long term variability effect may be at play. It is not yet clear, however, whether there is any relation to the ~4.6 yr superorbital modulation of the radio peak (Paredes, 1987; Gregory, 1999).

Two scenarios have been proposed to account for the observational features of LS I +61 303, as presented in Section 1.3.1 in the introduction chapter. The microquasar scenario requires accretion onto the compact object and the formation of a jet in which particles are accelerated and emit up to VHE gamma-rays through upscattering of stellar photons (e.g. Bosch-Ramon & Paredes, 2004; Bosch-Ramon et al., 2006). In the pulsar wind zone scenario, the compact object is a young pulsar and particles are accelerated at the interaction zone between the pulsar wind and the stellar wind (Maraschi & Treves, 1981; Dubus, 2006b). The stellar wind is thought to be formed by a fast, low-density polar wind and a slow, high-density equatorial decretion disc, which may be strongly truncated and have its properties disturbed by the compact object (Romero et al., 2007). On the other hand, the characteristics of the interaction of pulsar winds or microquasar jets with a massive star wind are not well constrained (but see the studies by, e.g, Bogovalov et al., 2008; Perucho & Bosch-Ramon, 2008). A broadband model by

Chernyakova et al. (2006) could explain the Spectral Energy Distribution (SED) from X-ray to HE gamma-ray bands through IC emission, but required an additional hadronic component to account for the MAGIC VHE emission. Doppler boosting effects could be present both for a microquasar jet and a shocked pulsar wind outflow (e.g. Khangulyan et al., 2008; Dubus et al., 2010), but its effects in both scenarios are difficult to assess because of our lack of knowledge on the geometry and orientation of the emitter. Finally, the uncertainty in the orbital geometry, in particular the inclination, also affects the ability of models to recover the physical parameters of the emitter (Sierpowska-Bartosik & Torres, 2009). All this shows the difficulties of the study of gamma-ray binaries.

The lack of a systematic behavior from cycle to cycle at X-ray and VHE bands, and the occurrence of short-term variability in the X-ray flux, has hampered the definitive detection of an X-ray/VHE correlation from the comparison of non-simultaneous data. We therefore conducted a multiwavelength campaign in 2007 September, covering the epoch of maximum VHE emission. Here, we report the first simultaneous VHE and X-ray observations of LS I +61 303 obtained with the MAGIC Cherenkov telescope and the *XMM-Newton* and *Swift* X-ray satellites that show correlated emission in both energy bands.

3.2 Observations and data analysis

3.2.1 VHE gamma rays[*]

The VHE gamma-ray observations were performed from 2007 September 4 to 21 using the MAGIC telescope on the Canary Island of La Palma (28.75°N, 17.86°W, 2225 m a.s.l.), from where LS I +61 303 is observable at zenith angles above 32°. At the time of the observations MAGIC consisted of a single 17 m diameter segmented mirror of parabolic shape, an f/D of 1.05, and an hexagonally shaped camera of 576 hemispherical photo multiplier tubes with a field of view of 3.5° diameter. MAGIC can detect gamma rays from 60 GeV to several TeV, and its energy resolution is $\Delta E/E = 20\%$ above energies of 200 GeV. The stand-alone telescope sensitivity is 1.6% of the Crab Nebula flux for a 5σ detection in 50 hr of on-source time. See Appendix A for a detailed account of the detection technique and the current status of the MAGIC telescopes.

[*] The data reduction of the MAGIC VHE gamma ray observations of LS I +61 303 presented in this chapter was performed by Neus Puchades and Tobias Jogler within the MAGIC Collaboration.

MJD[a]	Obs. Time	Phase Range	$N(>300\ \mathrm{GeV})^b$	UL[c]
	(minutes)		(10^{-12} cm^{-2} s^{-1})	
54348.148	203.0	0.470–0.476	1.1 ± 1.7	4.6
54349.157	210.1	0.508–0.514	-1.9 ± 2.0	2.5
54350.136	214.5	0.544–0.551	0.2 ± 2.1	4.4
54351.160	219.8	0.584–0.590	-0.1 ± 2.2	4.2
54352.161	221.1	0.621–0.627	15.7 ± 2.4	⋯
54353.163	224.2	0.659–0.665	7.7 ± 2.1	⋯
54354.166	212.5	0.697–0.703	2.8 ± 2.2	7.1
54355.153	172.4	0.734–0.741	0.3 ± 2.3	4.8
54356.139	148.7	0.771–0.777	0.1 ± 2.5	5.1
54357.153	178.1	0.809–0.816	6.4 ± 2.3	⋯
54358.155	179.3	0.847–0.854	8.1 ± 2.4	⋯
54359.154	184.4	0.885–0.892	2.9 ± 2.4	7.7
54360.154	177.3	0.923–0.929	5.7 ± 2.5	⋯
54361.154	183.1	0.960–0.967	5.3 ± 2.4	⋯
54362.153	188.7	0.998–0.005	-0.6 ± 2.4	4.2
54363.156	138.6	0.036–0.043	7.5 ± 2.8	⋯
54364.149	195.7	0.073–0.081	3.8 ± 1.9	⋯

Table 3.1: Log of the VHE Gamma-ray Observations. Notes: [a] The central MJD of each observation is quoted. [b] Uncertainties are given at 68% confidence level. [c] Upper limits are computed at the 95% confidence level.

The total observation time was 58.8 hr, including 39.6 hr in dark conditions and 19.2 hr under moonlight or twilight (Britzger et al., 2009). The range of zenith angles for these observations was $[32°, 50°]$, with 96% of the data having zenith angles below 43°. The final effective total observation time is 54.2 hr. Table 3.1 gives the MJD, the effective observation time, and the orbital phase for each of the MAGIC observations. The observations were carried out in wobble mode (Fomin et al., 1994), i.e., by alternately tracking two positions at 0.4° offset from the source position. This observing mode provides a reliable background estimate for point-like sources such as LS I +61 303.

The data analysis was performed using the standard MAGIC analysis and reconstruction software (Albert et al., 2008b, see also App. A.3). The quality of the data was checked and data taken with anomalous event rates (very low atmospheric transmission, car light flashes, etc.) were rejected following the standard procedure, as previously done in Albert et al. (2009). From the remaining events, image parameters were calculated (Hillas, 1985). In addition, the time parameters described in Aliu et al. (2009) were calculated as well. For

the gamma/hadron separation, a multidimensional classification procedure based on the image and timing parameters with the Random Forest method was used (Albert et al., 2008a). We optimized the signal selection cuts with contemporaneous Crab Nebula data taken at the same zenith angle range. The energy of the primary gamma-ray was reconstructed from the image parameters using also a Random Forest method. The differential energy spectrum was unfolded taking into account the full instrumental energy resolution (Albert et al., 2007). We estimate the systematic uncertainty to be about 30% for the derived integral flux values and ±0.2 for the obtained photon index. For more details on the systematic uncertainties present in the MAGIC data, see Albert et al. (2008b). In Table 3.1 we also show the flux upper limit for those observations with a flux significance below 2σ. The flux upper limits were computed by Jogler (2009) following the method of Rolke et al. (2005), see also Sec. A.3.1 for an account of upper limit calculation.

3.2.2 X-rays

We observed LS I +61 303 with *XMM-Newton* during seven runs from 2007 September 4 to 11, lasting from 12 to 18 ks (see Table 3.2), amounting to a total observation time of 104.3 ks. The EPIC pn detector used the Large Window Mode, while the EPIC MOS detectors used the Small Window Mode. All detectors used the medium thickness optical blocking filter. Data were processed using version 8.0.0 of the *XMM-Newton* Science Analysis Software (SAS). Known hot or flickering pixels were removed using the standard SAS tasks. Further cleaning was necessary to remove from the data set periods of high background corresponding to soft proton flares, reducing the net good exposure durations to 67.0 and 92.6 ks for the pn and MOS detectors, respectively.

Clean pn and MOS event files were extracted for spectral analysis. Source spectra were extracted from a ~70″ radius circle centered on the source (as suggested by the tool `eregionanalyse` and taking into account the 15″ point-spread function of the instrument) while background spectra were taken from a number of source-free circles with ~150″ radius (three for the pn detector, four for MOS1, and five for MOS2). The extracted spectra were analyzed with XSpec v12.3.1 (Arnaud, 1996). The spectra were binned so that a minimum of 20 counts per bin were present and energy resolution was not oversampled by more than a factor 3. An absorbed power-law function (`wabs*powerlaw`) yielded satisfactory fits for all observations. De-absorbed fluxes in the 0.3–10 keV range were computed from the spectral fits and its

	MJD[a]	Exposure Time Total (ks)	pn (ks)	MOS (ks)	Phase Range	$F(0.3-10\,\mathrm{keV})$[b] (10^{-12} erg cm^{-2} s^{-1})	Γ	N_{H} (wabs) (10^{22} cm^{-2})	χ^2/d.o.f.	Variab./Signif. (%)/(σ)
XMM-Newton	54347.202	12.4	10.8	12.4	0.434–0.440	13.8 ± 0.2 (± 2.4)	1.87 ± 0.03	0.517 ± 0.014	446.2/382	17.1/22.5
	54349.140	13.1	5.6	9.1	0.507–0.513	12.4 ± 0.2 (± 2.1)	1.66 ± 0.03	0.504 ± 0.019	379.8/352	16.8/15.1
	54350.199	18.3	10.5	17.1	0.546–0.554	13.3 ± 0.2 (± 1.6)	1.66 ± 0.02	0.514 ± 0.013	536.5/422	11.8/13.8
	54351.160	17.1	10.9	12.1	0.583–0.590	13.4 ± 0.2 (± 1.6)	1.68 ± 0.03	0.525 ± 0.015	431.6/400	12.1/12.8
	54352.146	14.7	5.8	13.2	0.621–0.627	22.9 ± 0.2 (± 1.6)	1.54 ± 0.02	0.538 ± 0.012	496.7/447	6.8/ 5.9
	54353.167	14.5	11.9	14.5	0.659–0.665	18.6 ± 0.2 (± 1.1)	1.58 ± 0.02	0.529 ± 0.013	467.5/429	5.9/ 1.9
	54354.144	14.2	11.5	14.2	0.696–0.702	12.6 ± 0.2 (± 1.3)	1.65 ± 0.03	0.520 ± 0.015	439.5/407	10.0/ 8.0
Swift/XRT	54354.663	3.3			0.716–0.722	10.3 ± 0.7 (± 2.0)	1.71 ± 0.16	0.5 (fixed)	5.38/14	18.4/ 1.1
	54355.670	2.7			0.754–0.759	12.4 ± 0.9 (± 1.6)	1.38 ± 0.14	0.5 (fixed)	8.83/15	10.7/ 0.3
	54356.671	3.3			0.792–0.797	17.6 ± 1.0 (± 2.0)	1.36 ± 0.10	0.5 (fixed)	9.83/26	9.9/ 0.4
	54357.674	3.3			0.830–0.835	13.9 ± 0.9 (± 2.3)	1.49 ± 0.14	0.5 (fixed)	13.07/20	15.3/ 1.2
	54358.178	3.8			0.848–0.855	17.7 ± 0.9 (± 1.5)	1.47 ± 0.09	0.5 (fixed)	20.46/32	6.3/ 0.1
	54359.951	5.3			0.911–0.926	19.5 ± 0.8 (± 2.6)	1.54 ± 0.07	0.5 (fixed)	34.52/50	12.7/ 0.4
	54362.247	2.1			0.996–0.014	13.7 ± 1.1 (± 3.6)	1.78 ± 0.19	0.5 (fixed)	5.45/11	25.0/ 1.7
	54363.121	2.5			0.034–0.042	12.3 ± 1.0 (± 1.5)	1.53 ± 0.16	0.5 (fixed)	9.71/13	9.3/ 0.1
	54365.530	2.2			0.127–0.130	13.3 ± 1.1 (± 1.7)	1.46 ± 0.15	0.5 (fixed)	10.14/12	10.1/ 0.5

Table 3.2: Log of the *XMM-Newton* (Top) and *Swift*/XRT (Bottom) X-ray Observations. Notes: [a] The central MJD of each observation is quoted. [b] Fluxes are de-absorbed. The uncertainties in parentheses include the uncertainties due to intrinsic X-ray variability during the observations.

uncertainty ranges obtained through the use of the `cflux` convolution model in Xspec.

Additional observations of 2–5 ks each, consisting of several pointings of 0.2–1.0 ks, were obtained with the *Swift*/XRT from 2007 September 11 to 22. The total observation time was 28.5 ks. The *Swift* data were processed using the FTOOLS task `xrtpipeline` (ver. 0.12.1 under HEASoft 6.6). The spectral analysis procedures were the same as those used for the *XMM-Newton* data. Since the hydrogen column density was poorly constrained, with typical values of $(0.5 \pm 0.2) \times 10^{22}$ cm^{-2}, we fixed it to 0.5×10^{22} cm^{-2}, a common value for previous X-ray observations of LS I +61 303, also found in the *XMM-Newton* fits and close to the average value for the *Swift* fits.

To search for short-term X-ray variability, we also extracted 0.3–10 keV background-subtracted light curves for each observation, binned to 100 s for *XMM-Newton* and at half-time of the sparse 0.2–1.0 ks *Swift* pointings within each observation. For *XMM-Newton*, we considered the sum of the count rate in the three detectors. From these light curves, we computed the degree of variability as the 1σ dispersion around the count rate mean divided by the mean. The significance of the variability was computed from the χ^2 probability of the count rate being constant. We also computed hardness ratios as the fraction between the count rates above and below 2 keV.

3.3 Results

3.3.1 VHE Gamma Rays

The measured fluxes of LS I +61 303 at energies above 300 GeV are listed in Table 3.1, and the corresponding light curve is shown in Figure 3.1 (top). The periodically modulated peak emission (Albert et al., 2009) is prominently seen as the highest flux value of these observations at phase 0.62 (followed by a lower flux at phase 0.66). In addition to this established feature we measured, as in 2006 December, significant flux on a nightly basis at phase 0.85. We note that there is significant flux in the phase range 0.8–1.0 at the level of $(5.2 \pm 1.0) \times 10^{-12}$ cm^{-2} s^{-1}, which is compatible with the 2σ upper limit we obtained for the shorter 2006 observations (Albert et al., 2009).

We also determined the differential energy spectrum from the ~10 hr of observations conducted in the orbital phase range 0.6–0.7. A power-law fit yields:

$$\frac{dN}{dE} = \frac{(2.0 \pm 0.3_{\rm stat} \pm 0.6_{\rm syst}) \times 10^{-12}}{\rm cm^2\ s\ TeV} \times \left(\frac{E}{1\ \rm TeV}\right)^{-2.7 \pm 0.3_{\rm stat} \pm 0.2_{\rm syst}}, \quad (3.1)$$

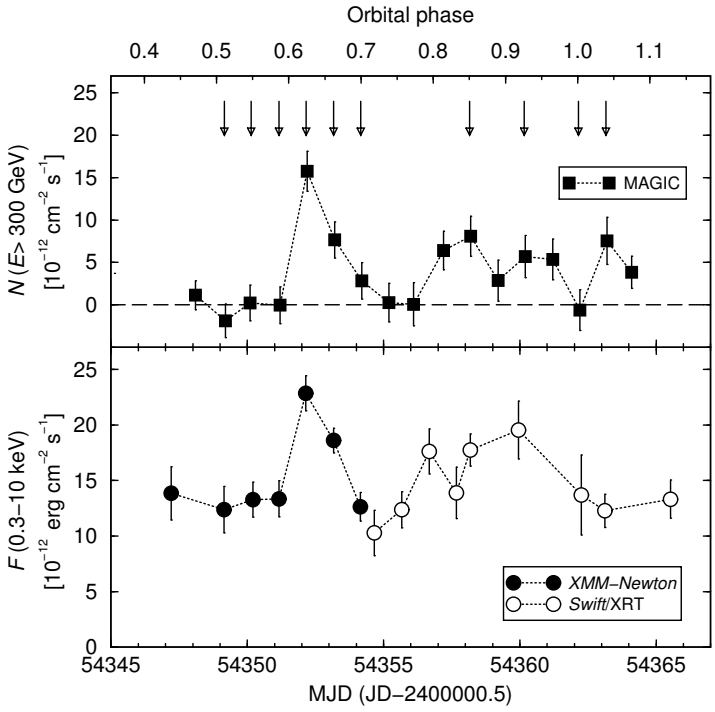

Figure 3.1: VHE gamma-ray and X-ray light curves of LS I +61 303 during the multi-wavelength campaign of 2007 September. *Top*: flux above 300 GeV vs. the observation time in MJD and the orbital phase. The horizontal dashed line indicates zero flux. The vertical arrows mark the times of simultaneous VHE gamma-ray and X-ray observations. *Bottom*: de-absorbed flux in the 0.3–10 keV energy range for the seven *XMM-Newton* observations (filled circles) and the nine *Swift* ones (open circles). Error bars correspond to a 1σ confidence level in all cases and include the intra-observation variability for the X-ray observations. Dotted lines join consecutive data points to help following the main trends of the light curves. The sizes of the symbols are larger than the time span of individual observations.

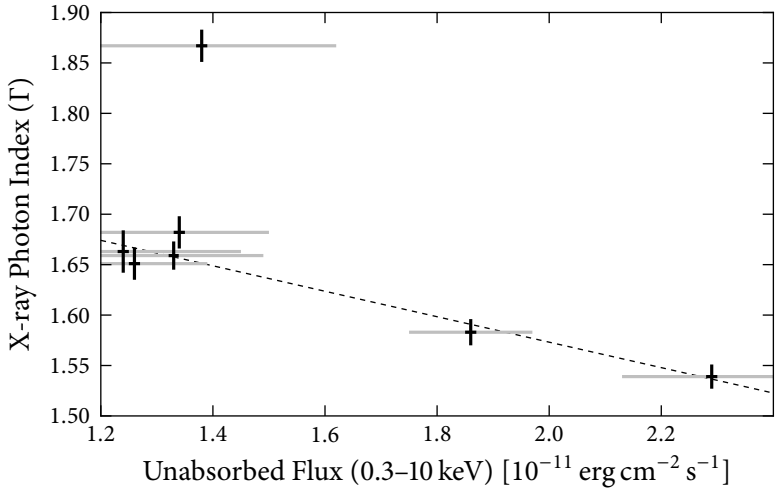

Figure 3.2: Unabsorbed flux in the 0.3–10 keV energy band versus measured power-law photon index for the *XMM-Newton* observations. The black errorbars are the flux and photon index uncertainties resulting from the spectral fits, whereas the gray errorbars correspond to the flux uncertainty when taking count-rate variability into account (see Sec. 3.3.2). The dashed line is plotted to guide the eye and indicate the anticorrelation present when excluding the observation with $\Gamma \simeq 1.87$.

compatible within errors with previous measurements (Albert et al., 2006, 2009).

3.3.2 X-rays

We summarize in Table 3.2 the parameters of the spectral fits and variability obtained for both the *XMM-Newton* and *Swift*/XRT data sets. All X-ray fluxes quoted hereafter are de-absorbed. We note that there is no significant hardness ratio change within each of the observations, in contrast to what was found in the *XMM-Newton* observations reported by Sidoli et al. (2006). In principle this implies that, for each observation, the flux and corresponding uncertainty obtained from the spectral fit is a good estimate of the flux during the whole observation. However, moderate count-rate variability on timescales of ks is present in most observations, ranging from 6% to 17% for the *XMM-Newton* data and from 9% to 25% for the *Swift* data (see last column in Table 3.2). The rms of this variability should be considered in addition to the statistical uncertainty when providing a flux measurement spanning several ks. We converted this count-rate variability into flux variability by

multiplying the degree of variability defined in Section 3.2.2 with the fluxes coming from the spectral fits. Since no spectral change is detected within each observation, we added this flux variability in quadrature to the spectral fits flux errors. This procedure provides the more realistic total flux uncertainties quoted in parentheses in Table 3.2, and used hereafter.

We show in Figure 3.1 (bottom) the 0.3–10 keV light curve of LS I +61 303. The source displays a steady flux during the first four observations and shows a steep increase at phase 0.62, which is followed by a slower decay up to phase 0.69 (*XMM-Newton*) and probably up to phase 0.72 (*Swift*). The behavior is very similar to the one seen at VHE gamma rays, although at X-ray energies the baseline has a significant flux. Later on there is a significant increase of the X-ray flux up to phase 0.8. This high flux is detected with a sparse sampling up to phase 0.9, and the source goes back to its baseline flux at phase 1.0. This increased X-ray flux between phases 0.8 and 1.0 occurs when the source is also detected at VHE gamma rays.

As shown in Figure 3.2, we recover the X-ray flux and photon index anti-correlation already seen by Sidoli et al. (2006). However, the observation performed on MJD 54347, corresponding to the orbital phase range 0.434–0.440, displays an abnormally soft X-ray spectrum given its unabsorbed flux. Other spectral fit parameters do not vary significantly with respect to the rest of observations, and in particular the neutral hydrogen column density remains compatible with a constant value around 5×10^{21} cm^{-2}. We note that this particular observation is not used on the X-ray/VHE correlation discussion below as simultaneous VHE observations were not available due to bad weather at the MAGIC site.

3.3.3 X-Ray/VHE Gamma-Ray Correlation

A clear correlation between the X-ray and VHE gamma-ray emissions is seen during the outburst, with a simultaneous peak at phase 0.62 (see Figure 3.1). To study the significance of this correlation, we selected the X-ray data sets that overlap with MAGIC observations. There are six data sets of overlapping MAGIC/*XMM-Newton* observations, for which strictly simultaneous observation times range from 3.3 to 3.9 hr. For the four overlapping MAGIC/*Swift* data sets, the strictly simultaneous observation times range from 2.2 to 4.1 hr (although the *Swift* runs have gaps). We plot in Figure 3.3 the X-ray fluxes against the VHE fluxes (from Tables 3.1 and 3.2) for all 10 simultaneous pairs, which are marked with arrows in Figure 3.1. The linear correlation coefficient for the six simultaneous MAGIC/*XMM-Newton* pairs that trace the outburst at phase 0.62 is $r = 0.97$. For the ten simultaneous pairs, we find $r = 0.81$ (a

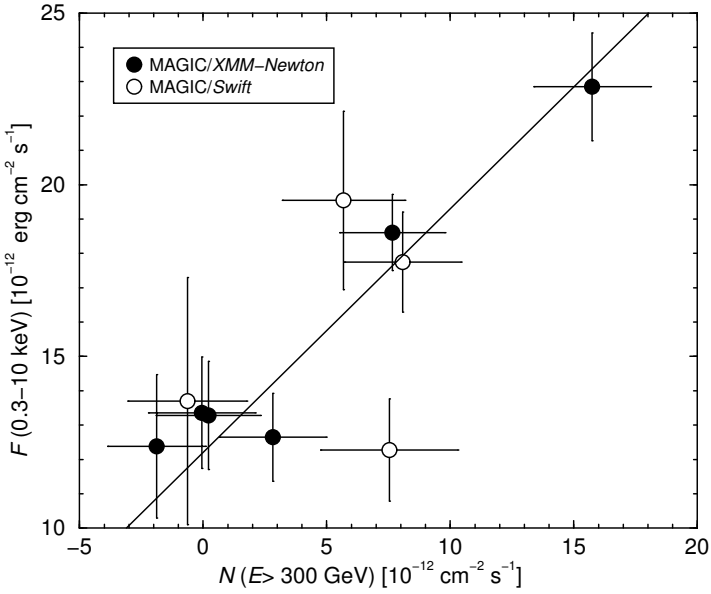

Figure 3.3: De-absorbed X-ray fluxes as a function of VHE gamma-ray fluxes. Only the 10 simultaneous fluxes, marked with arrows in Figure 3.1, have been considered. Error bars correspond to a 1σ confidence level in all cases. The solid line represents a χ^2 linear fit to all data points.

$|r|$ larger than that has a probability of about 5×10^{-3} to be produced from independent X-ray and VHE fluxes). Minimizing χ^2 we obtain $\chi^2 = 7.68$ for 8 degrees of freedom and the following relationship:

$$\left[\frac{F(0.3\text{–}10\,\mathrm{keV})}{10^{-12}\,\mathrm{erg\,cm^{-2}\,s^{-1}}}\right] = 12.2^{+0.9}_{-1.0} + 0.71^{+0.17}_{-0.14} \times \left[\frac{N(E > 300\,\mathrm{GeV})}{10^{-12}\,\mathrm{cm^{-2}\,s^{-1}}}\right], \quad (3.2)$$

where the uncertainties are non-Gaussian. This fit is plotted as a solid line in Figure 3.3.

However, as can be seen in Figure 3.3, the flux uncertainties are relatively large. This calls for a test of the reliability of the correlation strength considering the errors of individual data points. To this end, we use the z-Transformed Discrete Correlation Function (ZDCF), which determines 68% confidence level intervals for the correlation coefficient from unevenly sampled data (see, e.g., Edelson & Krolik 1988; Alexander 1997). The Fisher z-transform of the linear correlation coefficient is used to estimate the 68% confidence level interval. Applying the ZDCF to the X-ray and VHE light curves reported here we obtain the following uncertainties for the linear correlation coefficient: $r = 0.81^{+0.06}_{-0.21}$. The sensitivity of the MAGIC telescope requires observation

times of several hours to be able to get few-sigma detections for the VHE fluxes from LS I +61 303. During such long periods, the X-ray fluxes have quite large intrinsic variability (see Table 3.2). This results in quite large uncertainties on both the VHE and X-ray fluxes that restrict the ability to determine a possible correlation out of the outburst.

3.4 Discussion

We have discovered an X-ray/VHE gamma-ray correlation in the gamma-ray binary LS I +61 303 based on simultaneous multiwavelength data obtained with MAGIC, *XMM-Newton*, and *Swift* during a single orbital cycle. The correlation is mainly due to the very similar trends of the detected flux during the outburst around orbital phase 0.62, while the uncertainties prevent to be sure about the existence of the correlation outside the outburst. Given the variability in the X-ray flux (up to 25% on hour scales), it is necessary to program strictly simultaneous observations to perform correlation studies in LS I +61 303. This conclusion was also reached by the VERITAS Collaboration, when reporting the lack of X-ray/VHE correlation based on contemporaneous data with a VHE sampling that is not dense enough (Acciari et al., 2009). Although a similar X-ray/VHE correlation has been obtained for the VHE gamma-ray emitting X-ray binary LS 5039, the result was based on non-simultaneous data acquired years apart (Aharonian et al., 2005, 2006; Takahashi et al., 2009). However, as opposed to LS I +61 303, LS 5039 appears to be quite stable over long periods, particularly in the X-ray domain (Kishishita et al., 2009).

The VHE emission within a binary system can suffer photon–photon absorption via pair creation, mainly with the stellar optical/ultraviolet photons. In LS I +61 303, this absorption is only expected to be significant toward the observer for $E > 300$ GeV just before periastron (see following chapter and, e.g., Dubus 2006a; Bednarek 2006; Sierpowska-Bartosik & Torres 2009), a phase range not explored here. In addition, the quoted X-ray fluxes are already de-absorbed (and the hydrogen column densities and the associated errors are low). Overall, there are no absorption effects to be considered. Therefore, the X-ray/VHE correlation we have found for LS I +61 303 cannot be an artifact due to variable absorption toward the source. This indicates that the emission processes at both wavelengths occur at the same time and are probably the result of a single physical mechanism. In this context, it is reasonable to assume that the X-ray and VHE emissions are produced by a single particle population.

It is interesting to note that the MAGIC integrated flux in the 0.6–0.7 phase range yields $\sim 11 \times 10^{-12}$ erg cm^{-2} s^{-1} for $E > 300$ GeV, whereas the X-ray flux is $\sim 19 \times 10^{-12}$ erg cm^{-2} s^{-1}. Therefore, the total X-ray flux is approximately twice the VHE flux. However, if we subtract an apparent baseline X-ray flux of 10×10^{-12} erg cm^{-2} s^{-1}, the resulting X-ray flux is similar to the total VHE flux in the phase range 0.6–0.7. If the radiation mechanisms are dominated by a single particle population, the X-ray/VHE correlation and the lower or similar VHE fluxes favor leptonic models. In hadronic models, the X-ray emitting $e^{\pm}$ and the VHE photons would come from the same protons (for reasonable values of the magnetic field), and the luminosity of the $e^{\pm}$ radiation should be $\lesssim$½ that of VHE gamma-rays (see Figure 5 of Kelner et al. 2006 for reasonable proton energy distributions) unlike it is observed. In addition, the IC cooling channel is less efficient than the synchrotron channel to produce the detected X-ray emission for reasonable values of the magnetic field (see the next chapter for a deeper discussion or, for the case of LS 5039, Takahashi et al. 2009). This clearly suggests that the X rays are the result of synchrotron radiation of the same electrons that produce VHE emission as a result of IC scattering of optical/ultraviolet stellar photons.

The observed photon indices of the simultaneous X-ray and VHE spectra are consistent with one population of electrons following a power-law energy distribution with index ~2.1. These electrons would produce X-rays via synchrotron and VHE photons via IC with an interaction angle $\lesssim \pi/2$. We note that an electron index of ~2.1 is too hard if synchrotron cooling dominates in the X-ray range, since it implies an injected electron index of 1.1. On the other hand, dominant adiabatic cooling implies an injection index of 2.1, a more reasonable value (see section 4.3.1). Although small changes in the VHE spectrum would be expected due to variations in the IC interaction angle or the electron index (as seen in X-rays), at present they are not detectable due to the large uncertainties of the VHE photon index.

Finally, we note that contemporaneous radio light curves obtained with RATAN, VLBA images, and Hα spectroscopy are consistent with previous results (Gregory, 2002; Dhawan et al., 2006; Zamanov et al., 1999). Therefore, the X-ray/VHE correlation occurred when the source was showing a standard behavior in both its outflow (radio) and decretion disk (Hα line).

We end noting that the reduced sensitivity of the VHE gamma-ray observations when compared to the X-ray observations forced us to derive the correlation from X-ray and VHE flux bins encompassing whole observations. Therefore, we had to artificially increase the obtained X-ray flux uncertainty in order for the two data sets to probe the same source emission timescales. An increased sensitivity in the VHE gamma-ray band would allow us to per-

form detailed studies of short-term correlation, probing the source behavior in both bands on similar timescales. Even though this is not possible at present, the future Cherenkov Telescope Array (CTA), currently under planning, is expected to provide such an increase in sensitivity. In Appendix C we explore the possibilities of CTA for simultaneous X-ray and VHE observations of gamma-ray binaries, taking LS I +61 303 as an example and based on the correlation discussed in this chapter. Additionally, we consider the ability of CTA to detect spectral variations from LS I +61 303 in case the source spectrum is indeed variable within the $2.7 \pm 0.3_{\rm stat} \pm 0.2_{\rm sys}$ uncertainty range presented here, and as would be expected given the X-ray photon index variability.

References

Abdo, A. A., et al. 2009, ApJ, 701, L123

Acciari, V. A., et al. 2008, ApJ, 679, 1427

—. 2009, ApJ, 700, 1034

Aharonian, F., et al. 2005, Science, 309, 746

—. 2006, A&A, 460, 743

Albert, J., et al. 2006, Science, 312, 1771

—. 2007, Nuclear Instruments and Methods in Physics Research A, 583, 494

—. 2008a, Nuclear Instruments and Methods in Physics Research A, 588, 424

—. 2008b, ApJ, 674, 1037

—. 2009, ApJ, 693, 303

Alexander, T. 1997, in Astrophysics and Space Science Library, Vol. 218, Astronomical Time Series, ed. D. Maoz, A. Sternberg, & E. M. Leibowitz, 163–+

Aliu, E., et al. 2009, Astroparticle Physics, 30, 293

Aragona, C., McSwain, M. V., Grundstrom, E. D., Marsh, A. N., Roettenbacher, R. M., Hessler, K. M., Boyajian, T. S., & Ray, P. S. 2009, ApJ, 698, 514

Arnaud, K. A. 1996, in Astronomical Society of the Pacific Conference Series, Vol. 101, Astronomical Data Analysis Software and Systems V, ed. G. H. Jacoby & J. Barnes, 17–+

Bednarek, W. 2006, MNRAS, 368, 579

Bogovalov, S. V., Khangulyan, D. V., Koldoba, A. V., Ustyugova, G. V., & Aharonian, F. A. 2008, MNRAS, 387, 63

Bosch-Ramon, V., & Paredes, J. M. 2004, A&A, 425, 1069

Bosch-Ramon, V., Romero, G. E., & Paredes, J. M. 2006, A&A, 447, 263

Britzger, D., Carmona, E., Majumdar, P., Blanch, O., Rico, J., Sitarek, J., Wagner, R., et al. 2009, in Proc. of the 31st ICRC (Łódź), arXiv:0907.0973

Casares, J., Ribas, I., Paredes, J. M., Martí, J., & Allende Prieto, C. 2005, MNRAS, 360, 1105

Chernyakova, M., Neronov, A., & Walter, R. 2006, MNRAS, 372, 1585

Dhawan, V., Mioduszewski, A., & Rupen, M. 2006, in VI Microquasar Workshop: Microquasars and Beyond

Dubois, R. 2010, in Proceedings of the VERITAS Workshop on High Energy Galactic Physics, Barnard College, Columbia University, New York, ed. E. Aliu, J. Holder & R. Mukherjee, eConf C1005281, 9

Dubus, G. 2006a, A&A, 451, 9

—. 2006b, A&A, 456, 801

Dubus, G., Cerutti, B., & Henri, G. 2010, A&A, 516, A18+

Edelson, R. A., & Krolik, J. H. 1988, ApJ, 333, 646

Fomin, V. P., Stepanian, A. A., Lamb, R. C., Lewis, D. A., Punch, M., & Weekes, T. C. 1994, Astroparticle Physics, 2, 137

Frail, D. A., & Hjellming, R. M. 1991, AJ, 101, 2126

Gregory, P. C. 1999, ApJ, 520, 361

—. 2002, ApJ, 575, 427

Hillas, A. M. 1985, in International Cosmic Ray Conference, Vol. 3, International Cosmic Ray Conference, ed. F. C. Jones, 445–448

Holder, J. 2010, in Proceedings of the VERITAS Workshop on High Energy Galactic Physics, Barnard College, Columbia University, New York, ed. E. Aliu, J. Holder & R. Mukherjee, eConf C1005281, 10

Jogler, T. 2009, PhD thesis, Technische Universität München

Kelner, S. R., Aharonian, F. A., & Bugayov, V. V. 2006, Phys. Rev. D, 74, 034018

Khangulyan, D. V., Aharonian, F. A., Bogovalov, S. V., Koldoba, A. V., & Ustyugova, G. V. 2008, International Journal of Modern Physics D, 17, 1909

Kishishita, T., Tanaka, T., Uchiyama, Y., & Takahashi, T. 2009, ApJ, 697, L1

Maraschi, L., & Treves, A. 1981, MNRAS, 194, 1

Massi, M., & Kaufman Bernadó, M. 2009, ApJ, 702, 1179

Massi, M., Ribó, M., Paredes, J. M., Garrington, S. T., Peracaula, M., & Martí, J. 2004, A&A, 414, L1

Ong, R. A., et al. 2010, The Astronomer's Telegram, 2948

Paredes, J. M. 1987, PhD thesis, University of Barcelona

Paredes, J. M., Marti, J., Peracaula, M., & Ribo, M. 1997, A&A, 320, L25

Perucho, M., & Bosch-Ramon, V. 2008, A&A, 482, 917

Rea, N., Torres, D. F., van der Klis, M., Jonker, P. G., Méndez, M., & Sierpowska-Bartosik, A. 2010, MNRAS, 405, 2206

Rolke, W. A., López, A. M., & Conrad, J. 2005, Nuclear Instruments and Methods in Physics Research A, 551, 493

Romero, G. E., Okazaki, A. T., Orellana, M., & Owocki, S. P. 2007, A&A, 474, 15

Sidoli, L., Pellizzoni, A., Vercellone, S., Moroni, M., Mereghetti, S., & Tavani, M. 2006, A&A, 459, 901

Sierpowska-Bartosik, A., & Torres, D. F. 2009, ApJ, 693, 1462

Takahashi, T., et al. 2009, ApJ, 697, 592

Zamanov, R. K., Martí, J., Paredes, J. M., Fabregat, J., Ribó, M., & Tarasov, A. E. 1999, A&A, 351, 543

4

On the origin of correlated X-ray/VHE emission from LS I +61 303

4.1 Introduction

The discovery of correlated X-ray and VHE gamma-ray emission from the gamma-ray binary LS I +61 303 presented in the previous chapter suggests that the emission in these two bands has its origin in a single particle population. A first physical interpretation is given in Section 3.4, but it is strictly based on the basic features of the emission and correlation detected, so its physical inference power is relatively limited. In this chapter we aim to probe deeper into the properties of the multiwavelength non-thermal emitter in LS I +61 303 through the development of a leptonic one zone radiation model to explain the X-ray and VHE data. Our goal is to obtain robust physical parameters of the emitter by making as few assumptions as possible.

4.2 Simultaneous X-ray/VHE observations

The properties of the observations presented in the previous chapter may be found in Sections 3.2.1 and 3.2.2. Although all X-ray observations resulted in a clear detection, some of the VHE flux measurements have a significance below 2σ. For these cases we will consider the 95% confidence level upper

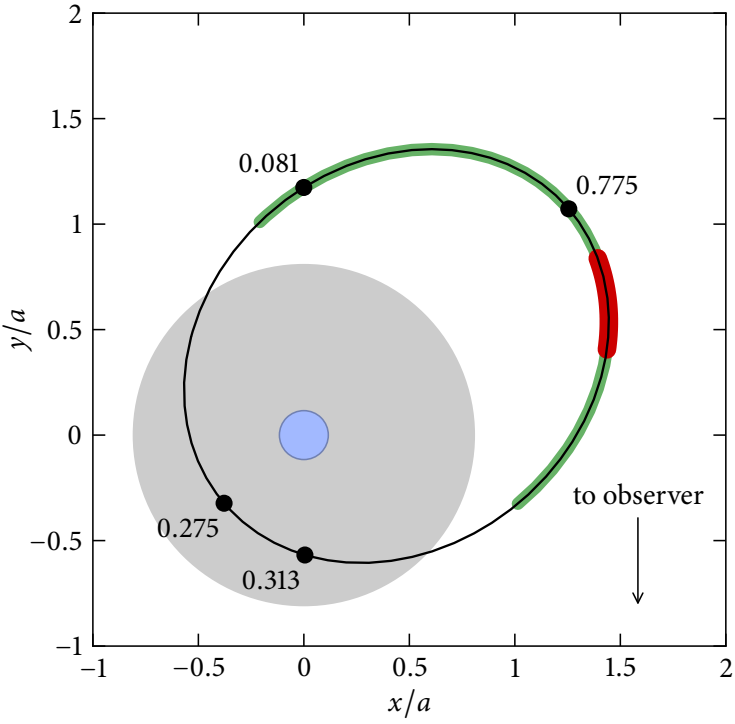

Figure 4.1: Orbital geometry of LS I +61 303 looking down on the orbital plane showing the orbit of the compact object around the Be star in units of the orbital semi-major axis. The positions labeled with the orbital phase correspond to periastron, apastron, and inferior and superior conjunctions. The X-ray/VHE multiwavelength campaign covered the phase range shown in green ($0.43 < \phi < 1.13$), while the phase range of the VHE emission outburst is shown in red ($0.6 < \phi < 0.7$). The Be star (blue circle) and the equatorial wind (grey circle) are shown assuming an equatorial disk radius of $r_d = 7R_\star$.

limits found in the last column of Table 3.1. These upper limits were computed following the method presented by Rolke et al. (2005) and assuming a 30% systematic uncertainty. The detailed fluxes, upper limits and uncertainties of the X-ray and VHE light curves may be found in Tables 3.1 and 3.2.

The sensitivity of VHE observations precludes obtaining nightly spectra, and only a spectrum combining the observations with phases between 0.6 and 0.7 could be obtained (see Sec. 3.3.1 and Eq. 3.1). In order to obtain a simultaneous SED, we extracted an *XMM-Newton* spectrum of the source for the three X-ray observations that correspond to the MAGIC spectrum. We filtered the data using SAS v10.0 and extracted three individual spectra from the pn instrument. We used the SAS tool `efluxer` to convert the spectra from counts vs. channel into physical units (flux density vs. energy), averaged the three unbinned spectra and then grouped the bins to a signal-to-noise ratio of 20. In order to compare the measured spectrum to the computed intrinsic spectrum, we deabsorbed the former using the `wabs` FORTRAN subroutine provided with Xspec v12.0 (Arnaud, 1996). We used a column density of $N_{\rm H} = 5 \times 10^{21}$ cm^{-2} obtained from the average of the individual fits of an absorbed power law to the three observations. This column density is consistent with that of the ISM alone (Paredes et al., 2007).

4.3 Model description

The discovery of a correlation between the X-ray and VHE bands points towards a common mechanism of emission modulation at both bands. In a leptonic scenario, the fast and simultaneous changes in flux in both bands indicate that the modulation mechanism has to directly affect the emission level of the Inverse Compton (IC) and synchrotron processes. Assuming constant injection, a way to obtain correlated X-ray and VHE emission is through a modulation of the number of emitting particles by dominant adiabatic losses, which would be related to the (magneto)hydrodynamical processes in the accelerator and emitter regions. These processes may be related, for instance, to the interaction of the pulsar wind or the black hole jet with the stellar wind of the massive companion. The hard X-ray spectrum with photon index $\Gamma \approx 1.5$ also points towards dominant adiabatic losses, which imply an injection electron index of $\alpha_{\rm e} \approx 2$, as already pointed out in Section 3.4. In the regime of dominant adiabatic losses the emitted X-ray flux is proportional to the number of emitting particles, so the orbital dependency of adiabatic losses can be inferred from the X-ray light curve. Dominant adiabatic losses are not uncommon when modelling gamma-ray binaries. They have also been invoked to explain the variations of the X-ray and VHE fluxes in the gamma-ray bi-

naries PSR B1259-63 and LS 5039 by Khangulyan et al. (2007) (see also Kerschhaggl 2011) and Takahashi et al. (2009), respectively. We note that the IC emission will be additionally modulated by the changes in seed photon density along the orbit as well as the geometrical effects of the location of the emitter along the orbit (see Sec. 2.3.1).

For the sake of simplicity, and given how little we know about the properties of the particle accelerator and the non-thermal emitter in LS I +61 303, we will here assume a constant particle injection spectrum and emitter magnetic field along the orbit. We will also adopt one leptonic population cooling down under variable adiabatic losses at the location of the emitter, which will be approximated as homogeneous and point-like.

The orbital parameters were adopted from Aragona et al. (2009) with an inclination angle of $i = 45°$. We will also discuss other possibilities regarding the inclination angle, in particular the extremes of the allowed range $15° \lesssim i \lesssim 60°$ considered by Casares et al. (2005). A sketch of the orbital configuration of LS I +61 303 can be seen in Fig. 4.1 with the phase ranges of the simultaneous X-ray/VHE campaign indicated. The equatorial wind disk in binaries of the characteristics of LS I +61 303 is expected to be truncated at a radius of $r_d = 5R_\star$ (Grundstrom et al., 2007). However, the variability in the equivalent width of the Hα line indicates that its radius can vary between $4.5R_\star$ and $7R_\star$ (Zdziarski et al., 2010; Sierpowska-Bartosik & Torres, 2009). A variable red shoulder in the Hα line (McSwain et al., 2010) could point towards the creation of a tidal stream in the equatorial disk because of the proximity of the compact object at periastron that eventually falls back onto the disk at later phases. Tidal disruption and eventual truncation of the equatorial disk was also seen in hydrodynamical simulations of the system by Romero et al. (2007). Even at its largest possible radius of $7R_\star$, as assumed in Fig. 4.1, the equatorial disk does not affect the phase ranges of the observations we are considering, and thus we will not include it in our model.

4.3.1 Adiabatic cooling

One of the remarkable features of the VHE light curve of LS I +61 303 is the lack of detectable emission during periastron (Albert et al., 2009). IC emission is very effective at this phase owing to the high stellar photon density, so the lack of emission means that either it is strongly absorbed or that the number of accelerated electrons falls drastically. However, the angular dependency of the pair production process, $\propto (1 - \cos\psi)$ for the interaction rate and $\propto (1 - \cos\psi)^{-1}$ for the gamma-ray energy threshold (where ψ is the interaction angle of the incoming photons, see Eq. 2.11), implies that ab-

sorption is very low for phases immediately after periastron even under the dense seed photon field of the star (see Section 2.3.2 for details on the calculation of pair production absorption). Inverse Compton emission also has a dependency on the angle between the seed photon and the accelerated electron and would be lower during these phases, but this effect is diminished at higher energies when scattering takes place in the deep Klein-Nishina regime (see Section 2.3.1 and Figure 2.1). Therefore, a reduction in the number of accelerated particles is required to explain the lack of VHE emission around periastron. Although the X-ray flux during periastron is around half of the peak flux during the periodic outbursts, the non-detection of VHE emission during periastron places an upper limit at only a 10% of the outburst peak VHE flux. Taking all this into account, we will assume that in the context of one electron population the X-ray/VHE correlation is only valid for the X-ray excess flux above a certain quiescent or pedestal emission. Therefore, the number of emitting particles responsible for this excess X-ray flux is lower and their VHE emission remains at non-detectable levels around periastron. This reasoning is supported by the X-ray/VHE correlation reported in the previous chapter, in which the constant term of the linear correlation (Eq. 3.2) is $(12.2^{+0.9}_{-1.0}) \times 10^{-12}\,\mathrm{erg\,cm^{-2}\,s^{-1}}$. Considering that some of the X-ray observations are below this constant term, we took the pedestal flux value to be $F_{\mathrm{ped}} = 11.5 \times 10^{-12}\,\mathrm{erg\,cm^{-2}\,s^{-1}}$.

As mentioned above, a scenario with dominant adiabatic losses is a very good candidate mechanism to explain the correlation characteristics of the source. When considering a system with constant magnetic field and constant injected electron spectrum, the only modulation in synchrotron radiation is due to the modulation of the dominant cooling process that results in a modulation of the (evolved) stationary electron distribution. For dominant adiabatic losses and a constant injection rate, the X-ray flux will be proportional to the adiabatic cooling time t_{ad}. A consistent calculation of t_{ad} would require knowledge of the exact nature of the source and the (magneto)hydrodynamical processes that take place there. One can however infer t_{ad} along the orbit by taking it proportional to the excess flux above the pedestal $F_{\mathrm{X}} - F_{\mathrm{ped}}$, which is independent of the electron energy. For the phases covered by the X-ray observations we derived a smooth curve following the behaviour of the X-ray fluxes. For the phases outside the campaign coverage we assumed a flat light curve consistent with the first four observations at phases 0.43 to 0.59 and the last observation at phase 0.13. Choosing the ratio $t_{\mathrm{ad}}/(F_{\mathrm{X}} - F_{\mathrm{ped}})$ as small as possible while keeping the adiabatic losses dominant allows us to put a lower limit on the injected luminosity budget. This choice of the ratio $t_{\mathrm{ad}}/(F_{\mathrm{X}} - F_{\mathrm{ped}})$ yields adiabatic loss time scales of

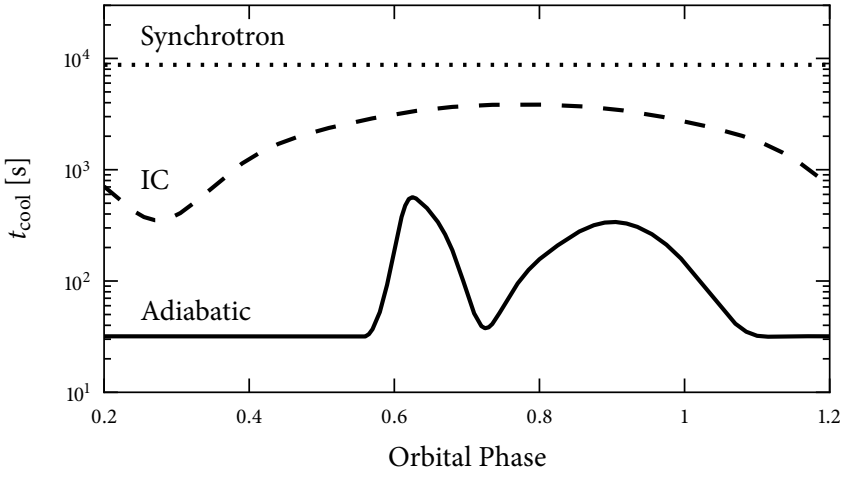

Figure 4.2: Cooling times along the orbit for adiabatic (solid), synchrotron (dotted) and IC (dashed). The synchrotron and IC cooling times are shown at $E_{\rm e} = 10^{12}$ eV. This energy corresponds to electrons that emit in the X-ray band through synchrotron and in the VHE band through IC.

between 35 and 500 seconds. Figure 4.2 shows the orbital evolution of the cooling time scales inferred for adiabatic and calculated for IC and synchrotron losses. The adiabatic cooling time is independent of the electron energy, but for synchrotron and IC the cooling time scales are given at $E_{\rm e} = 10^{12}$ eV. This energy corresponds to electrons that emit in the X-ray band through synchrotron and in the VHE band through IC.

4.3.2 Particle energy distribution and maximum energy

For LS I +61 303 the adiabatic and radiative cooling time scales of high-energy electrons are much shorter than the orbital period, and thus shorter than the time scales of variation of the ambient properties. Therefore, it is safe to assume the parent particle population evolves into the so-called steady-state electron energy distribution. A detailed account of how to compute the steady-state energy distribution is given in Section 2.1. Here we have assumed a constant injected particle spectrum $Q(\gamma)$ consisting of a power law function with a high-energy cutoff at an energy $E_{\rm e,max}$, obtained through the balance of the acceleration and energy loss rates. The resulting evolved steady-state electron energy distribution computed at each point along the orbit, $n(\gamma_{\rm e}, \phi)$, is then used to obtain the properties of the emitted radiation.

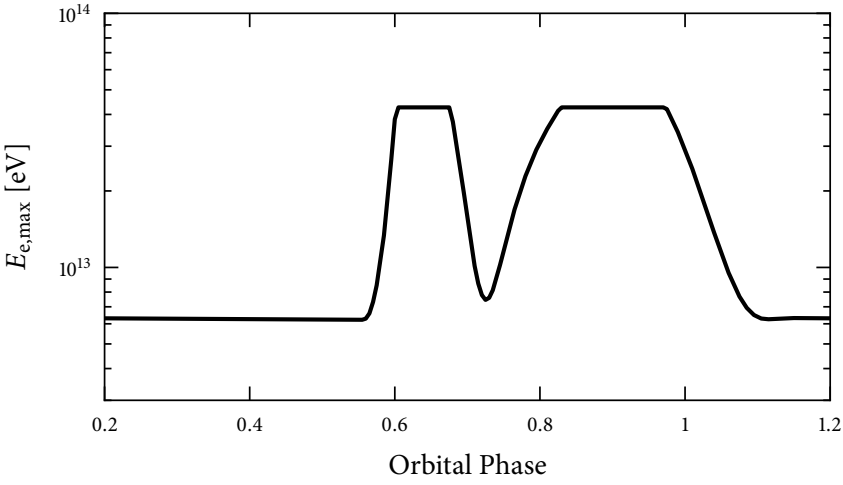

Figure 4.3: Maximum electron energy $E_{e,max}$ along the orbit taking $\eta = 10$ (see text for details).

The VHE gamma-ray energy spectrum of LS I +61 303 extends up to $E_\gamma \sim$ 10 TeV (see Acciari et al., 2009) without a break in the spectrum, indicating that electrons must be accelerated up to energies beyond 10 TeV. The acceleration of electrons has to be faster than the cooling times of the different cooling mechanisms so that the electrons can reach these very high energies. The maximum electron energy will be that for which $t_{acc} = t_{cool}$. The acceleration time of electrons may be parametrized as $t_{acc} = \eta E/(ecB)$, where $\eta \geq 1$ gauges the effectiveness of acceleration and $E/(ecB)$ is the maximum energy gain rate allowed by classical electrodynamics. The maximum energy resulting from the balance of this expression for the acceleration time and the energy loss time scales for synchrotron, IC and non-radiative losses may be found in Section 2.5. At each point along the orbit, all relevant time scales are evaluated and the corresponding $E_{e,max}$ is obtained. The adiabatic cooling times inferred from the X-ray light curve range from a few tens to a few hundred seconds. When considering the requirement that acceleration takes place up to electron energies of 10 TeV, we can see that the accelerator required must be quite efficient with $\eta \approx 7$–130 depending on the orbital phase. Since we are assuming that the injection is constant, we also expect the acceleration rate to be constant and have chosen a value of $\eta = 10$ to perform the energy cutoff calculations along the orbit, which would correspond to acceleration in a parallel diffusive shock with velocity of $\sim 0.8c$ (therefore favoring a mildly relativistic shock). The orbital dependency of the maximum electron energy

for $\eta = 10$ is shown in Fig. 4.3. During periods of low X-ray flux $E_{\mathrm{e,max}}$ has a behaviour proportional to t_{ad} (compare with Fig. 4.2). We note, however, that it is possible that adiabatic losses do not take place strictly at the acceleration region but rather at the emitter, and thus would not affect the maximum energy of accelerated particles. In this case, the required efficiency would be limited by synchrotron losses, and the required efficiency would likely be at the lower end of the range stated above, i.e., around $\eta \simeq 100$.

4.3.3 Radiation and absorption calculation

For each position along the orbit, we calculate the emitted synchrotron spectrum from the evolved particle distribution and the magnetic field through Eq. 2.3. Synchrotron emission in the X-ray range will be generally characterized by a photon index of $\Gamma_{\mathrm{X}} = (\alpha_{\mathrm{e}} + 1)/2 \approx 1.5$. The orbital dependence of the electron maximum energy will affect the shape of the spectrum, typically hardening (softening) it for high (low) fluxes, which correspond to lower (higher) adiabatic losses and therefore a higher (lower) maximum electron energy. However, since the cutoff in the particle distribution is located at energies significantly higher than those responsible for X-ray emission, this effect is small in the X-ray energy band ($\Delta\Gamma_{\mathrm{X}} \sim 0.2$).

We calculate the IC emission component following the expressions and anisotropic cross-section presented in Section 2.3.1. The stellar radiation field is used as the seed photon distribution of the IC process taking it as blackbody radiation at $kT = 2$ eV with a luminosity of $L_\star = 10^{38}\,\mathrm{erg\,s^{-1}}$.

The intense radiation field can also absorb very high energy γ-ray emission through pair production $\gamma\gamma \rightarrow \mathrm{e^+e^-}$ (Gould & Schréder, 1967). An exploration of the effects that this absorption can have on the observed spectrum of gamma-ray binaries can be found in Bosch-Ramon & Khangulyan (2009) and references therein. Here we compute the energy-dependent attenuation factor of VHE gamma-rays following the procedure outlined in Section 2.3.2. The attenuation factor $\exp(-\tau_{\gamma\gamma})$ is applied to the intrinsic IC spectrum (dashed line in Fig. 4.5) to obtain the spectrum emitted out of the binary system (solid line in Fig. 4.5).

4.4 Results

As seen in Fig. 4.4, we were able to reproduce the X-ray and VHE light curves obtained during the 2007 multiwavelength campaign. Although the good agreement with the X-ray light curve is expected because we derived the

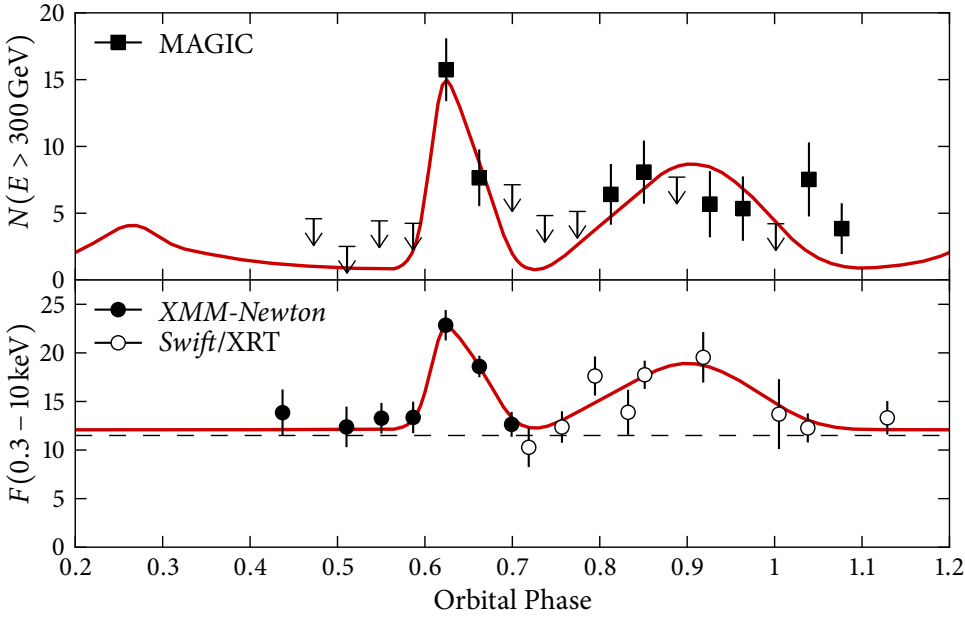

Figure 4.4: *Top:* Computed VHE light curve (red line) and observed VHE light curve by MAGIC in units of 10^{-12} ph/cm^2/s. Observations with a significance above 2σ are shown in filled squares, while 95% confidence level upper limits are shown otherwise. *Bottom:* Computed X-ray light curve (red line) and X-ray light curve observed during the multiwavelength campaign with *XMM-Newton* (filled circles) and *Swift*/XRT (open circles) in units of 10^{-12} erg/cm^2/s. The pedestal flux is indicated by a horizontal dashed line. All error bars correspond to 1σ uncertainties. The same parameters as in Fig. 4.5 are used for both panels.

dominant adiabatic losses from the observed X-ray fluxes, the VHE light curve is a prediction of the model taking into account the binary geometry, the stellar photon field, and the non-thermal particle distribution. Furthermore, the spectral indices in the X-ray and VHE energy bands for the outburst at phases $0.6 < \phi < 0.7$ are well reproduced, as can be seen in Fig. 4.5.

4.4.1 Electron population

We found that the best fit to the X-ray and VHE photon indices can be obtained by taking a particle energy distribution with slope $\alpha_e = 2.1$. As mentioned above, the photon index in the X-ray band directly depends on the particle index of the parent electron population. In the X-ray band, the observations show a photon index between 1.58 ± 0.02 and 1.66 ± 0.02 (plus a 1.85 ± 0.02 outlier) for the *XMM-Newton* observations, which was found to be anti-correlated with the X-ray flux (see Section 3.3.2). The time-dependent energy cutoff given by the variability of cooling time scales provides a small time dependent variation of the photon index through a modification of the shape of the spectrum. Regarding the VHE observations, the measured photon index is $2.7 \pm 0.3_{stat} \pm 0.2_{sys}$ for the three observations during the first outburst. Because absorption is low at the orbital phases of the maximum, the photon index is determined by α_e and the IC interaction angle. The parent particle population with $\alpha_e = 2.1$ results in computed X-ray photon indices in the range 1.55–1.67 and reproduces the observed anti-correlation between Γ_X and F_X (see Figure 3.2). In the VHE band the adopted α_e results in photon indices in the range 2.6–2.8 for high-flux phases, whereas the spectrum is much softer for low flux phases because of the lower energy cutoff. Figure 4.5 presents the SED averaged over the phase ranges of the three simultaneous observations during the first outburst (phases 0.62, 0.66 and 0.70), and shows that both the flux levels and the photon indices at X-ray and VHE are well reproduced.

The GeV spectrum and fluxes along the orbit appear incompatible with one leptonic population. Therefore, the one-zone model presented here does not account for the high fluxes detected by *Fermi*. Additionally, we found that the phase-averaged SED calculated using a power law with $\alpha_e = 2.1$ and a high-energy cutoff produces a flux too high in energies between 10 and 100 GeV when compared to the phase-averaged spectrum measured by *Fermi*/LAT (Abdo et al., 2009). A way to avoid this excess flux is to consider the electron injection spectrum described by a broken power law with a harder particle index below $E_e = 4 \times 10^{11}$ eV. We found that the softest particle index for which the computed GeV spectrum is compatible with the *Fermi*/LAT measure-

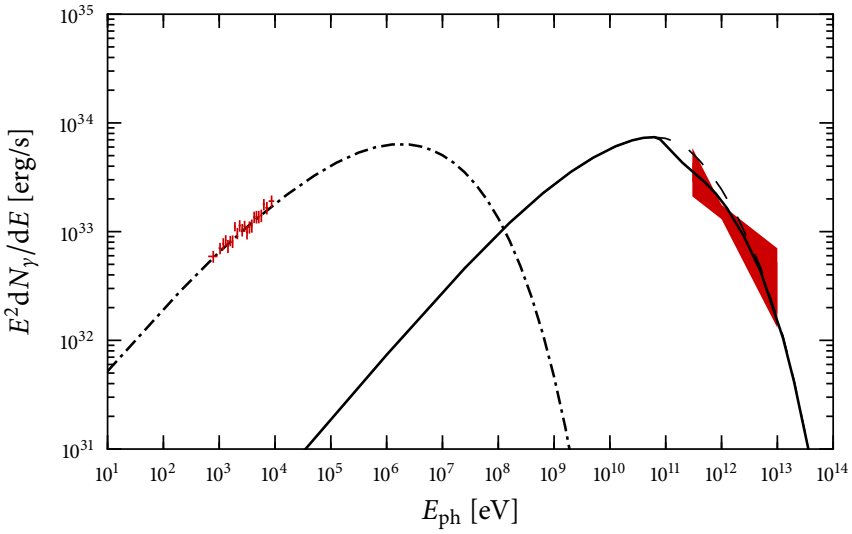

Figure 4.5: Computed SED averaged over the three observation periods during the first outburst (phases 0.62, 0.66 and 0.70), with synchrotron (dot-dashed), IC (solid) and non-absorbed IC (dashed) components. The calculations were performed with $i = 45°$ and $B = 0.22$ G. The red crosses show the *XMM-Newton* EPIC-pn spectrum averaged over three observations and deabsorbed taking $N_H = 5 \times 10^{21}$ cm^{-2}. To compare the measured flux to the excess computed X-ray flux, we subtracted a pedestal power law spectrum corresponding to a 0.3 – 10 keV flux of 11.5×10^{-12} erg cm^{-2} s^{-1}. The MAGIC simultaneous spectrum is shown as a red bow-tie.

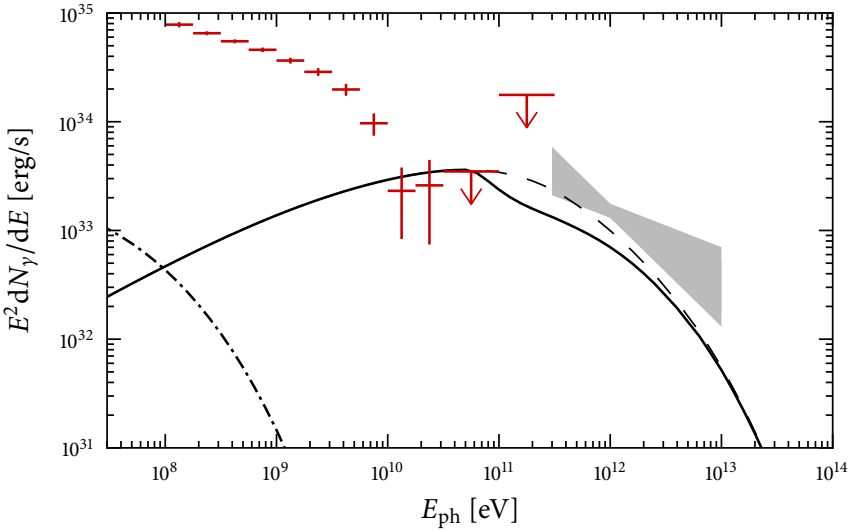

Figure 4.6: Computed SED averaged over the whole orbit with synchrotron (dot-dashed), IC (solid) and non-absorbed IC (dashed) components, calculated with the same parameters as in Fig. 4.5. The crosses and upper limits indicate the phase-averaged *Fermi*/LAT spectrum. The MAGIC VHE spectrum during the outburst is shown as a bow-tie. The MAGIC spectrum corresponds to different phases than the computed SED and is shown as a reference to Fig. 4.5. We note that the radiation model is not supposed to explain the high GeV fluxes as we expect HE gamma-ray emission to have its origin in a different particle population.

ment is $\alpha_e \lesssim 1.8$. It must be noted that this change in the particle index at low energies does not affect the spectrum of particles that emit in the X-ray and VHE bands through synchrotron and IC, respectively. The *Fermi*/LAT spectrum along with the computed phase averaged SED is shown in Fig. 4.6. The phase-averaged *Fermi*/LAT cannot be easily compared with the peak spectrum shown in Fig. 4.5 because the X-ray/VHE and GeV measurements are not simultaneous. Furthermore, the orbital variability of the GeV spectrum at higher energies (i.e., the shape of the cutoff) has not been clearly established by Abdo et al. (2009), and a phase-resolved spectrum cannot be derived from a phase averaged-spectrum.

4.4.2 Magnetic field

The X-ray/VHE flux ratio is a very sensitive indicator of the magnetic field in the emitter. We found the magnetic field that best describes the observed

light curves by performing a exploration of the parameter space of B and the normalization of the injected particle spectrum Q_0. For each (B, Q_0) pair we calculated the X-ray and VHE light curves and estimated the goodness-of-fit to the observed flux points using a χ^2 test. The observed light curves are best described using an ambient magnetic field of $B = 0.22$ G. It is not trivial to set a formal uncertainty range on this value because of the unknown number of constraints that should be considered (e.g., the shape used for the adiabatic cooling curve). However, we see that for variations of the order of 0.05 G around the best-fit value of $B = 0.22$ G the observed X-ray and VHE light curves are no longer well described by the computed ones.

4.4.3 *Injection energy budget*

The adopted luminosity in injected accelerated particles is $2 \times 10^{35}\,\mathrm{erg\,s^{-1}}$ along the whole orbit. The computed emission bolometric luminosity, on the other hand, varies between $\sim 10^{34}$ and $\sim 1.5 \times 10^{35}\,\mathrm{erg\,s^{-1}}$. Note that the adopted injected luminosity is only a lower limit because we arbitrarily chose the lowest ratio between the X-ray flux and the adiabatic cooling time scale. For higher adiabatic losses (while still proportional to X-ray emission), the emitted spectrum would be equivalent but the required injected luminosity would be higher.

The dominant energy band in the broad-band SED of LS I +61 303 is the MeV-GeV region. Using the gamma-ray spectrum measured by *Fermi*/LAT (Abdo et al., 2009) we can obtain a lower limit on the power available for particle acceleration. The observed energy flux above 100 MeV is $F_{100} \simeq 4.1 \times 10^{-10}\,\mathrm{erg\,cm^{-2}\,s^{-1}}$, resulting in an observed luminosity of $2 \times 10^{35}\,\mathrm{erg\,s^{-1}}$. Given this high luminosity, it is natural to think than the acceleration mechanism at play is able to provide a similar power to the X-ray and VHE emitting electrons.

4.5 Discussion

4.5.1 *Adiabatic time scales*

The orbital variability and range of adiabatic losses may be used to pose constraints on the hydrodynamical properties of the various scenarios proposed for LS I +61 303. Hydrodynamical calculations have been performed in the binary pulsar scenario (Romero et al., 2007; Bogovalov et al., 2008; Khangulyan et al., 2008) and for the interaction of a microquasar jet with the wind of a

young star (Acciari et al., 2008; Perucho et al., 2010). However, for LS I +61 303 it is difficult to calculate the adiabatic losses in each of the mentioned scenarios because of the uncertainties in the properties of the Be stellar wind and the relativistic outflows.

In our phenomenological framework, we find that the required adiabatic loss time scales range between 35 and 500 s, as seen in Fig. 4.2. Whereas it is difficult to relate these time scales to those arising from complex geometries (e.g. shocked pulsar wind or a microquasar jet), we can use the simple model of an expanding sphere to obtain insight on relevant emitter properties. The adiabatic loss time scale $t_{\rm ad}$ is related to the typical scale of the emitter $R_{\rm em}$ and its expansion velocity $v_{\rm exp}$ through $t_{\rm ad} = R_{\rm em}/v_{\rm exp}$. While the size of the emitting region is unknown, the fact that a one-zone emitter located at the compact object position can successfully explain the X-ray/VHE emission indicates that the region must be small compared with the orbital separation. Considering an emitting region with a radius 10% of the orbital separation we obtain a range of radii between $\sim 3 \times 10^{11}$ cm (at periastron) and $\sim 9 \times 10^{11}$ cm (at apastron). For these sizes, the maximum expansion velocities would be required for the shortest adiabatic cooling time scale, i.e. 35 s. At apastron the expansion would need to be highly relativistic, with a velocity of $0.85c$ (similar to the relativistic sound speed $c/\sqrt{3}$), corresponding to a Lorentz factor of $\Gamma = 1.89$, whereas for periastron it would be mildly relativistic at $0.29c$. For the longer adiabatic loss time scales of hundreds of seconds, the required expansion velocities would be much lower, of the order of $0.01c$–$0.06c$. A change in the size of the emitter could be caused by the change in external pressure from the stellar wind, resulting in a larger emitter at apastron (Takahashi et al., 2009). This would explain the location of the X-ray/VHE outbursts around apastron, but it is not clear which magnetohydrodynamical process is responsible for the variation of the adiabatic loss time scale of more than an order of magnitude in 20 h. Wind clumping can be considered as a source of pressure variability, as suggested by Zdziarski et al. (2010), but it would not explain the constant location of the X-ray/VHE outburst ($0.6 < \phi < 0.7$) orbit after orbit. On the other hand, a transition of the emitter from a region dominated by polar wind to a region dominated by equatorial wind, or vice versa, could give rise to such a fast change in wind pressure. In addition, there could be other yet unknown properties of the stellar wind, as shown by the recent detection of a variable red shoulder in the Hα line by McSwain et al. (2010), which could be related to a tidal stream in the equatorial wind falling back onto the disk.

4.5.2 Energetics

The energetics of the system, regardless of the acceleration mechanism, are able to provide the required injected power used in our model given the high flux in the MeV-GeV band (see Sec. 4.4.3).

The pulsar-like spectrum of LS I +61 303 in the GeV band (power law with exponential cutoff at a few GeV) prompted Abdo et al. (2009) to consider a magnetospheric origin for the HE gamma-ray emission. In this scenario we can gain some insight on the spin-down luminosity of the putative pulsar from the HE gamma-ray luminosity. The observed energy flux F_{100} from magnetospheric emission can be related to the emitted gamma-ray luminosity L_γ as

$$L_\gamma = 4\pi f_\Omega(\alpha, \zeta_{\rm E}) d^2 F_{100},$$

where f_Ω is a beaming correction factor that depends on the geometry of the emitter, the magnetic angle α and the Earth viewing angle $\zeta_{\rm E}$. The emitted gamma-ray luminosity is related to the pulsar spin-down luminosity through the gamma-ray efficiency $\eta_\gamma = L_\gamma(\dot{E})/\dot{E}$. A trend was found from EGRET observations that the efficiency scaled as $\dot{E}^{-1/2}$ (Thompson et al., 1999), and this was later confirmed (at least for $\dot{E} > 10^{34}$ erg s^{-1}) by *Fermi*/LAT arriving to $\eta_\gamma \simeq 0.034(\dot{E}/10^{36}\ {\rm erg\,s^{-1}})^{-1/2}$ (Abdo et al., 2010). Using this relation, $\dot{E}$ can be inferred from L_γ as $\dot{E} \simeq L_\gamma^2/(1.156 \times 10^{33}\ {\rm erg\,s^{-1}})$. From the LS I +61 303 phase-averaged gamma-ray spectrum measured by Abdo et al. (2009) we obtain $F_{100} \simeq 4.1 \times 10^{-10}$ erg cm^{-2} s^{-1}, from which $L_\gamma \simeq 2 \times 10^{35} f_\Omega$ erg s^{-1}. Following these considerations, the spin-down luminosity inferred from the *Fermi*/LAT observations is of $\dot{E} \simeq 3.3 \times 10^{37} f_\Omega^2$ erg s^{-1}. Traditionally (e.g. polar cap models) it was assumed that the gamma-ray beam covers a solid angle of 1 sr uniformly, so $f_\Omega = 1/(4\pi) \simeq 0.08$, which would result in a spin-down luminosity of $\dot{E} \simeq 2 \times 10^{35}$ erg s^{-1}. However, more modern pulsar beaming models (e.g. slot gap and outer gap models) have $f_\Omega \sim 1$ for many viewing angles (Watters et al., 2009), which would result in a more energetic pulsar with $\dot{E} \simeq 3 \times 10^{37}$ erg s^{-1}. The fact that the cutoff of the spectrum is located at high energies ($E_{\rm cutoff} = 6.3 \pm 1.1$ GeV) points to a high-altitude location for gamma-ray emission, since emission beyond a few GeV is very difficult close to the neutron star because of strong attenuation from $\gamma B \rightarrow e^+e^-$ absorption (Baring, 2004). The general trend in the *Fermi*/LAT pulsar sample (Abdo et al., 2010) also points towards a high-altitude location, so we favour slot gap or outer gap models for which the spin-down luminosity of the putative pulsar in LS I +61 303 would be of $\dot{E} \simeq 3 \times 10^{37}$ erg s^{-1}. Even though the *Fermi*/LAT observations do not completely constrain the spin-down lu-

minosity of the putative pulsar, the power available for particle acceleration is high. In the favoured scenario of $\dot{E} \simeq 3 \times 10^{37}\,\mathrm{erg\,s^{-1}}$, assuming that the power in injected electrons constitutes only a fraction 10^{-2} of the spin-down luminosity (e.g., Sierpowska-Bartosik & Torres, 2008), the power in relativistic electron would be larger than our requirement of $L_{\mathrm{inj}} = 2 \times 10^{35}\,\mathrm{erg\,s^{-1}}$.

Another possibility is that instead of a magnetospheric origin, the emission detected by *Fermi*/LAT has an IC origin. In this case the efficiency between the spin-down luminosity of the putative pulsar and the observed IC luminosity is expected to be of 1–10%. Considering the observed luminosity of a few times $10^{35}\,\mathrm{erg\,s^{-1}}$, the pulsar would need to have a spin-down luminosity of the order of $10^{37}\,\mathrm{erg\,s^{-1}}$.

The higher values of spin-down luminosities pose a problem for the binary pulsar scenario regarding the shape of the detected radio emission. Dhawan et al. (2006) strongly argued that the rotating cometary-like tail they detected in VLBA observations was related to the shocked pulsar wind contained by the stellar wind. Romero et al. (2007) already questioned the ability of the stellar wind to contain the pulsar wind from the results of three-dimensional hydrodynamical simulations even when considering a significantly lower spin-down luminosity of $10^{36}\,\mathrm{erg\,s^{-1}}$. The shape of the interaction region between the stellar and pulsar winds is determined by the ratio of wind momentum fluxes

$$\eta_{\mathrm{w}} = \frac{\dot{E}_{\mathrm{PSR}}/c}{\dot{M}_{\star} v_{\mathrm{w}\star}},$$

where $\dot{M}_{\star}$ and $v_{\mathrm{w}\star}$ are the mass-loss rate and wind velocity of the Be star and $\dot{E}_{\mathrm{PSR}}$ is the spin-down luminosity of the pulsar. For the polar wind, we can take $\dot{M}_{\star} = 10^{-8}\,M_{\odot}\,\mathrm{yr^{-1}}$ and $v_{\mathrm{w}\star} = 10^{3}\,\mathrm{km\,s^{-1}}$, resulting in a wind momentum flux ratio of $\eta_{\mathrm{w}} = 0.53(\dot{E}_{\mathrm{PSR}}/10^{36}\,\mathrm{erg\,s^{-1}})$ (Romero et al., 2007). Ignoring orbital motion (which on the other hand would give rise to small deviations in the inner region of the interaction, see Parkin & Pittard 2008), the opening half-angle of the interaction cone would be

$$\theta_{\mathrm{w}} = 180^{\circ}\frac{\eta_{\mathrm{w}}}{1+\eta_{\mathrm{w}}},$$

as seen in analytical models of wind interaction (e.g. Antokhin et al., 2004). For a spin-down luminosity of $10^{36}\,\mathrm{erg\,s^{-1}}$ the stellar wind would barely dominate the pulsar wind ($\eta_{\mathrm{w}} = 0.53$, $\theta_{\mathrm{w}} = 62^{\circ}$). Considering the favoured high-altitude location for gamma-ray production (i.e., slot gap or outer gap models) or an IC origin of the gamma-ray emission, the pulsar spin-down luminosity is of the order of $\dot{E}_{\mathrm{PSR}} \simeq 3 \times 10^{37}\,\mathrm{erg\,s^{-1}}$. Given this luminosity,

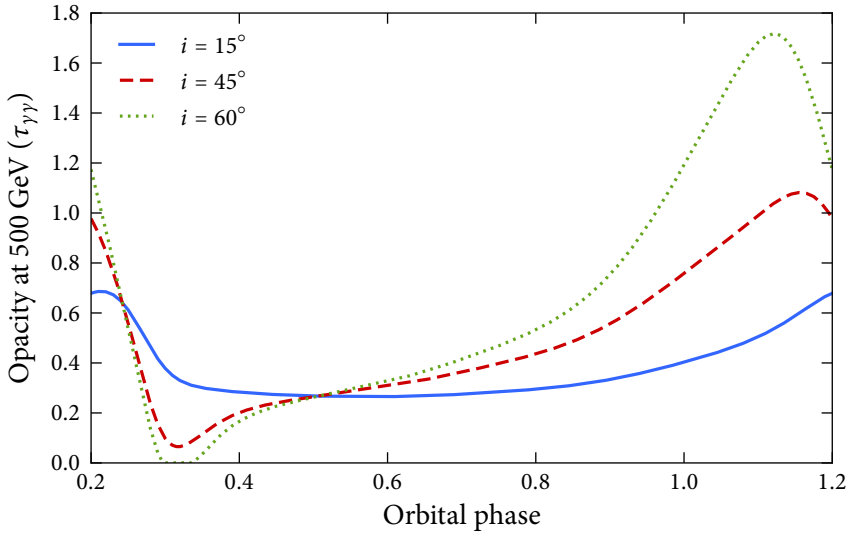

Figure 4.7: Opacity of 500 GeV gamma rays owing to pair production interactions with the stellar photon field as a function of orbital phase for different values of orbital inclination.

the pulsar wind would dominate the interaction and would not be contained by the stellar wind. The ratio of wind momentum fluxes would then be of $\eta_{\rm w} \simeq 16$ and the half-opening angle would approach 180°, posing a completely different scenario from that usually pictured by wind interaction models (e.g. Dubus, 2006; Sierpowska-Bartosik & Torres, 2009; Zdziarski et al., 2010). A lower value of the beaming correction factor f_Ω in the magnetospheric scenario could mean that the pulsar spin-down luminosity is as low as $\dot{E}_{\rm PSR} \simeq 2 \times 10^{35}\,{\rm erg\,s^{-1}}$ and thus contained by the stellar wind. However, given the high energy of the cutoff in the *Fermi*/LAT spectrum of LS I +61 303 we favour a high-altitude location for gamma-ray production, leading to the higher value of the spin-down luminosity.

4.5.3 Orbital inclination

Synchrotron emission will have no dependence on the orbital inclination because we are assuming isotropic particle distribution and a fully disordered magnetic field. For IC emission, on the other hand, there is a dependence with the angle $\theta_{\rm IC}$ between the line of sight and the direction of propagation of the seed photons (i.e., the connecting line between the star and the com-

pact object). Given the orbital configuration of LS I +61 303 (see Fig. 4.1), $\theta_{\rm IC}$ will not vary significantly with inclination for the phases around apastron, at which the source is detected in VHE. For $\gamma\gamma$ absorption, on the other hand, the dependency is on the angle between the directions of the VHE photon and the seed photon integrating along the line of sight out of the system. This means that absorption will show weaker orbital variability for low inclinations and stronger for high inclinations. For the flux peak observed at $\phi = 0.62$, the optical depth of $\gamma\gamma$ absorption is practically independent of inclination at $\tau_{\gamma\gamma} \approx 0.2$ for 500 GeV photons. However, the second, wider outburst at phases 0.8–1.1, does have an absorption dependency with inclination, with $\tau_{\gamma\gamma} \approx 1.4$ for $i = 60°$ but $\tau_{\gamma\gamma} \approx 0.3$ for $i = 15°$ (see Figure 4.7). The diminished absorption at low inclinations leads to a VHE flux higher than the observed values, particularly taking into account the upper limit measurement at phase 0.8. However, given the high uncertainties of the VHE nightly fluxes, the difference between the light curves computed for $i = 60°$ and $i = 15°$ is of less than 1σ. Even though we do not consider it significant given the present sensibilities, deeper VHE observations with firm detections at these phases could help to constrain the inclination of the orbit.

4.5.4 Magnetic field

The X-ray/VHE fluxes can be explained using a constant magnetic field of $B = 0.22$ G. A constraint on the accelerator maximum energy can be put by requiring that the Larmor radius of the accelerated electron ($r_{\rm L} = E_{\rm e}/eB$) is contained within the accelerator size. This translates to a maximum energy of $E_{\rm max} \simeq 300\, B_{\rm G} R_{12}$ TeV, where $B_{\rm G}$ is the magnetic field in Gauss and R_{12} the accelerator radius in units of 10^{12} cm. For the magnetic field we found and considering an accelerator size of the order of 10% of the orbital separation, the maximum energy is well above the required 10 TeV and radiative losses dominate at high energies (see Sec. 4.3.2). In the binary pulsar modelling approach of Dubus (2006), the magnetic flux was considered variable along the orbit as a consequence of the variation in the distance of the wind-shock region to the pulsar. In the shocked wind region, the magnetic field values obtained were as high as 10 G. Chernyakova et al. (2006) obtain a very similar magnetic field to ours, with $B = 0.25$ G ($B = 0.35$ G) for the low (high) flux state of the source. However, the model is based on an emitting particle spectrum very soft at high energies, resulting in a synchrotron component peaking in the radio band and an IC component dominating from soft X-ray to the MeV band. They require another hadronic component to explain the VHE emission. The magnetic field in this model traces the flux ratio between

radio and X-ray fluxes instead of ours, which traces the flux ratio between X-ray and VHE. On the other hand, in the microquasar approach used by Bosch-Ramon et al. (2006), the magnetic field at the base of the jet was taken as 1 G. Most of these approaches use higher magnetic fields than the one we found to best reproduce the observational features. An explanation for this is likely the need in these models to generate both the pedestal and X-ray flux that we considered independently.

4.6 Summary and concluding remarks

We presented a radiation model of a single leptonic population that can successfully describe the data obtained through a simultaneous X-ray/VHE campaign on LS I +61 303 performed by MAGIC in 2007. The X-ray/VHE emission correlation observed indicates both that the emission at these bands may come from a single particle population and that energy losses may be dominated by adiabatic losses. By assuming a constant magnetic field and injection along the orbit, we inferred the adiabatic loss rate from the X-ray light curve and the time dependent electron maximum energy as the balance between acceleration and energy loss time scales. We found that a quite efficient accelerator ($\eta \lesssim 100$) is required to obtain the observed VHE spectra because of the fast adiabatic cooling. The injected electron spectrum is constant along the orbit and initially taken as a power law with a high-energy cutoff, but the *Fermi*/LAT HE spectrum poses a constraint on the hardness of the spectrum at lower energies, which we estimate has to be harder than $\alpha_e \simeq 1.8$ for electron energies below 4×10^{11} eV. At higher energies, on the other hand, an index of $\alpha_e = 2.1$ matches the observed X-ray and VHE photon indices. The observed light curves are best reproduced using a magnetic field of $B = 0.22$ G. The general picture shows that the observed emission in X-ray and VHE is compatible with originating in the same parent particle population under dominant adiabatic losses.

The required luminosity budget in injected electrons for the computed X-ray and VHE emission is 2×10^{35} erg/s. Both the microquasar and binary pulsar scenarios are able to provide these levels of luminosity in accelerated electrons. The GeV luminosity of LS I +61 303 can also give us hints on the available power: independently of whether the detected emission is magnetospheric or IC emission, the injected power should be $\gtrsim 10^{37}$ erg/s. If it is magnetospheric emission, the high-altitude favoured scenario of gamma-ray production implies that the spin-down luminosity of the pulsar is $\dot{E} = 3 \times 10^{37}$ erg/s. This high spin-down luminosity poses problems for the binary pulsar scenario because the pulsar wind would not be contained by the stellar

wind, which would give rise to a completely different scenario from the one usually considered.

The VHE and X-ray light curves of LS 5039 and LS I +61 303 seem relatively similar, both peaking close to the apastron. For LS 5039 the maximum is also close to the inferior conjunction of the compact object, whereas this is not the case in LS I +61 303. If the light curve maxima are related to apastron rather than to the observer orientation with respect to the system, it may point to a similar physical origin for the X-ray and VHE modulation in both sources. On the other hand, the adiabatic losses could have a different cause. Recall the very different stellar winds in both sources.

We found that the X-ray and the VHE emission are consistent with a single parent particle population, whereas the HE gamma-ray emission detected by *Fermi*/LAT probably has a different origin. The orbital anti-correlation and the exponential cutoff spectrum suggest that several non-thermal emitting regions may be present in the system. This could also explain the presence of a pedestal emission in X-ray that is compatible with constant emission along the orbit.

We conclude noting that simultaneous observations at the X-ray and VHE bands provide a unique diagnostic tool to probe the emitter properties in galactic variable sources. Future observations, in particular by more sensitive next-generation VHE observatories, will allow us to better understand these peculiar systems. The physical interpretation performed in this chapter could greatly benefit from more sensitive VHE observations, as simulated in Appendix C for a simultaneous *Chandra* and CTA campaign.

References

Abdo, A. A., et al. 2009, ApJ, 701, L123

—. 2010, ApJS, 187, 460

Acciari, V. A., et al. 2008, ApJ, 679, 1427

—. 2009, ApJ, 700, 1034

Albert, J., et al. 2009, ApJ, 693, 303

Antokhin, I. I., Owocki, S. P., & Brown, J. C. 2004, ApJ, 611, 434

Aragona, C., McSwain, M. V., Grundstrom, E. D., Marsh, A. N., Roettenbacher, R. M., Hessler, K. M., Boyajian, T. S., & Ray, P. S. 2009, ApJ, 698, 514

Arnaud, K. A. 1996, in Astronomical Society of the Pacific Conference Series, Vol. 101, Astronomical Data Analysis Software and Systems V, ed. G. H. Jacoby & J. Barnes, 17–+

Baring, M. G. 2004, Advances in Space Research, 33, 552

Bogovalov, S. V., Khangulyan, D. V., Koldoba, A. V., Ustyugova, G. V., & Aharonian, F. A. 2008, MNRAS, 387, 63

Bosch-Ramon, V., & Khangulyan, D. 2009, International Journal of Modern Physics D, 18, 347

Bosch-Ramon, V., Paredes, J. M., Romero, G. E., & Ribó, M. 2006, A&A, 459, L25

Casares, J., Ribas, I., Paredes, J. M., Martí, J., & Allende Prieto, C. 2005, MNRAS, 360, 1105

Chernyakova, M., Neronov, A., & Walter, R. 2006, MNRAS, 372, 1585

Dhawan, V., Mioduszewski, A., & Rupen, M. 2006, in VI Microquasar Workshop: Microquasars and Beyond

Dubus, G. 2006, A&A, 456, 801

Gould, R. J., & Schréder, G. P. 1967, Physical Review, 155, 1404

Grundstrom, E. D., et al. 2007, ApJ, 656, 437

Kerschhaggl, M. 2011, A&A, 525, A80+

Khangulyan, D., Hnatic, S., Aharonian, F., & Bogovalov, S. 2007, MNRAS, 380, 320

Khangulyan, D. V., Aharonian, F. A., Bogovalov, S. V., Koldoba, A. V., & Ustyugova, G. V. 2008, International Journal of Modern Physics D, 17, 1909

McSwain, M. V., Grundstrom, E. D., Gies, D. R., & Ray, P. S. 2010, ApJ, 724, 379

Paredes, J. M., Ribó, M., Bosch-Ramon, V., West, J. R., Butt, Y. M., Torres, D. F., & Martí, J. 2007, ApJ, 664, L39

Parkin, E. R., & Pittard, J. M. 2008, MNRAS, 388, 1047

Perucho, M., Bosch-Ramon, V., & Khangulyan, D. 2010, A&A, 512, L4+

Rolke, W. A., López, A. M., & Conrad, J. 2005, Nuclear Instruments and Methods in Physics Research A, 551, 493

Romero, G. E., Okazaki, A. T., Orellana, M., & Owocki, S. P. 2007, A&A, 474, 15

Sierpowska-Bartosik, A., & Torres, D. F. 2008, ApJ, 674, L89

—. 2009, ApJ, 693, 1462

Takahashi, T., et al. 2009, ApJ, 697, 592

Thompson, D. J., et al. 1999, ApJ, 516, 297

Watters, K. P., Romani, R. W., Weltevrede, P., & Johnston, S. 2009, ApJ, 695, 1289

Zdziarski, A. A., Neronov, A., & Chernyakova, M. 2010, MNRAS, 403, 1873

5

Thermal X-ray emission from the shocked stellar wind of pulsar gamma-ray binaries

5.1 Introduction

The emission from the non-thermal particle population accelerated in the Pulsar Wind Shock (PWS) scenario has been widely studied in the radio, X-ray and HE and VHE gamma-ray bands (Maraschi & Treves, 1981; Tavani & Arons, 1997; Kirk et al., 1999; Dubus, 2006; Bogovalov et al., 2008, and references therein). Furthermore, the possibility of detecting the free pulsar wind from its spectral signature has also been discussed (Kirk et al., 1999; Khangulyan et al., 2007; Cerutti et al., 2009). However, one of the sources of emission that could provide valuable information on the characteristics of gamma-ray binaries has been previously overlooked: the thermal X-ray emission from the shocked stellar wind. Massive stellar binaries (of types O+O or O+WR) are known to produce powerful thermal X-ray emission in the Wind Collision Region (WCR), where the supersonic winds of the two young stars interact (see, e.g., Pittard et al., 2005, for a review). Even though it has been previously considered that the detection of X-ray emission lines could be an indication of accretion in gamma-ray binaries (e.g., Rea et al., 2010), similar lines can arise from the thermal X-ray emission of the shocked stellar wind in the WCR. The complexity of the stellar winds from the Be companion stars

in LS I +61 303 and PSR B1259−63 makes the analysis of the thermal emission from the shocked stellar wind difficult. The presence of both a polar wind and a decretion disk adds a large number of unknown free parameters. On the other hand, the radial and more powerful stellar wind from the O star in LS 5039 turns this source into an ideal candidate to study the observational impact of the thermal wind emission.

The system LS 5039 is located at 2.5 ± 0.1 kpc and contains a compact object with a mass between 1.4 and 5 $M_\odot$ orbiting an O6.5V((f)) donor star every 3.90603 ± 0.00017 days (Casares et al., 2005) in a mildly eccentric orbit ($e = 0.24 \pm 0.08$; Sarty et al., 2011). The detection of elongated asymmetric emission in high-resolution radio images was interpreted as mildly relativistic ejections from a microquasar jet and prompted its identification with an EGRET HE gamma-ray source (Paredes et al., 2000, 2002). However, recent VLBA observations by Ribó et al. (2008) show morphological changes on short timescales that might be consistent with a PWS scenario. LS 5039 shows variable periodic emission in the X-ray, HE gamma-ray and VHE gamma-ray bands. The X-ray lightcurve has an orbital modulation (Takahashi et al., 2009), superposed by short timescale features that are quite stable over the years (Kishishita et al., 2009). The maximum and minimum emission phases in the periodic lightcurve are located at the inferior and superior conjunctions, so a geometrical effect for the modulation has been suggested. However, inferior and superior conjunctions are located close to apastron and periastron, and the broadness of the peaks, well fitted by a sinusoidal function, makes it difficult to discern between a physical or geometric origin of the modulation. Whereas the VHE gamma-ray lightcurve has a modulation similar to the X-ray one (Aharonian et al., 2006), the HE gamma-ray flux is lower at the inferior conjunction ($0.45 < \phi < 0.9$) and higher at superior conjunction ($0.9 < \phi < 0.45$). In addition, at superior conjunction it shows a spectral cutoff at $E = 1.9 \pm 0.5$ GeV, not statistically required for inferior conjunction data (Abdo et al., 2009).

In the present chapter we present a model of the thermal X-ray emission from the shocked stellar wind of pulsar gamma-ray binaries from which the spin-down luminosity of the putative pulsar can be constrained. We apply it to the case of LS 5039, and obtain an upper limit on the spin-down luminosity of the putative pulsar within.

5.2 The dynamical model

In the PWS scenario the pulsar wind and the stellar wind collide forming an interaction region bounded on either side by the reverse shocks of the winds.

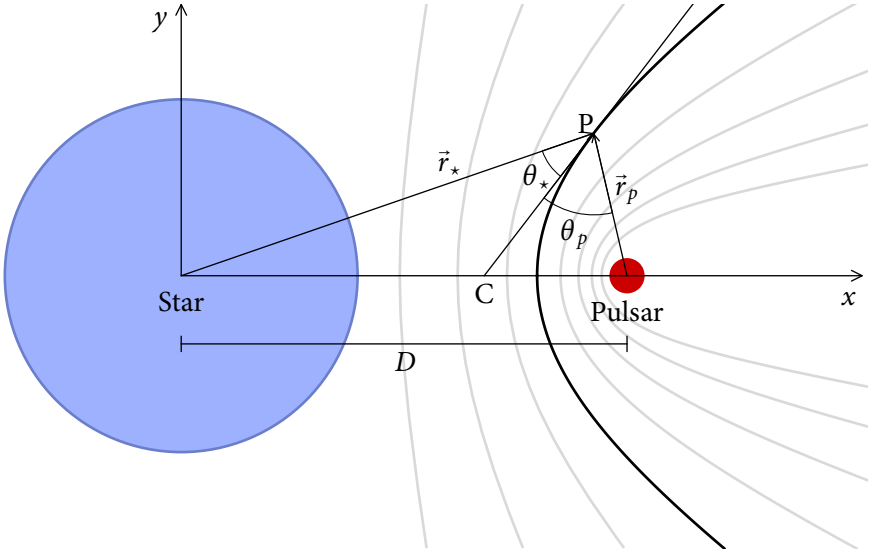

Figure 5.1: Illustration of the dynamical model at periastron. The star (but not the pulsar) is at scale. The thick black line indicates the shape of the CD for $\dot{M} = 4.25 \times 10^{-7}\,\mathrm{M}_\odot/\mathrm{yr}$ and $L_{\mathrm{sd}} = 7.5 \times 10^{36}\,\mathrm{erg\,s^{-1}}$, corresponding to $\eta_\infty = 0.04$. The line CP is tangent to the CD at the point P, for which the angles and radii used in the derivation of the CD are shown. The gray lines show the shape of the CD for values of η_∞ spaced logarithmically in the range 0.003–0.3.

The shocked winds are separated by a surface called contact discontinuity (CD), located where the ram pressure components perpendicular to this surface are in equilibrium: $p_{\star\perp} = p_{p\perp}$.

The ram pressure of the relativistic pulsar wind can be described at any point at a distance r_p from the pulsar as $p_p(r_p) = L_{\mathrm{sd}}/(4\pi c r_p^2)$, where L_{sd} is the spin-down luminosity of the pulsar. In the case of the stellar wind, we will assume a β-velocity law, $v(r_\star) = v_\infty(1 - R_\star/r_\star)^\beta$, where $r_\star$ is the distance to the center of the star, $R_\star$ is the radius of the star and v_∞ is the terminal velocity of the stellar wind. We have considered $\beta = 0.8$, which has been shown to be a good approximation of the outer structure of the winds of hot massive stars (Pauldrach et al., 1986). Assuming a constant mass-loss rate from the star $\dot{M}$, the density of the stellar wind is $\rho = \dot{M}/(4\pi r_\star^2 v(r_\star))$. The ram pressure of the stellar wind can then be described as $p_\star(r_\star) = \dot{M} v(r_\star)/(4\pi r_\star^2)$.

The balance of perpendicular components of the ram pressure that defines the position of the CD

$$\frac{\dot{M} v(r_\star)}{4\pi r_\star^2} \sin^2\theta_\star = \frac{L_{\mathrm{sd}}/c}{4\pi r_p^2} \sin^2\theta_p,$$

can be rearranged to obtain the dimensionless parameter η

$$\frac{r_p^2 \sin^2\theta_\star}{r_\star^2 \sin^2\theta_p} = \frac{L_{\rm sd}/c}{\dot{M} v(r_\star)} \equiv \eta(x,y), \tag{5.1}$$

where $\theta_\star$ and θ_p are the angles between the CD surface and the directions towards the center of the star and the pulsar, respectively. The coordinates x and y correspond to the position along the line of centers and the distance from it, respectively (see Fig. 5.1). Following Antokhin et al. (2004), we can obtain the differential equation that describes the shape of the CD as a function of η,

$$\frac{{\rm d}x}{{\rm d}y} = \frac{1}{y}\left[x - \frac{D r_\star^2(x,y)\sqrt{\eta(x,y)}}{r_\star^2(x,y)\sqrt{\eta(x,y)} + r_p^2(x,y)}\right], \tag{5.2}$$

where $x(y)$ is the function describing the shape of the CD and D is the binary separation. The boundary condition $({\rm d}x/{\rm d}y|_{y\to 0} \to 0)$ is $x_0 = D/(1+\sqrt{\eta})$, the location of pressure equilibrium along the symmetry axis, also known as stagnation radius. For the case of constant wind velocities, η will be constant and x_0 and $x(y)$ can be computed analytically. However, given the β-velocity law we adopted for the stellar wind, a numerical integration is required to obtain the shape of the CD since the stellar wind may not yet have reached its terminal velocity at the contact surface. Figs. 5.1 and 5.2 show the resulting shape of the CD in comparison to the star-pulsar system and for different positions along the orbit of LS 5039 as a function of $\eta_\infty \equiv (L_{\rm sd}/c)/(\dot{M} v_\infty)$.

Given the very high speed of the stellar wind, the role of orbital motion in the shape of the CD is not expected to be significant. The aberration or skew angle μ of the shock cap, defined as the angle between the axis of symmetry of the shock cap and the line of centers of the star and compact object, is given by $\tan\mu = v_{\rm orb}/v_{\rm w}$, where $v_{\rm orb}$ is the orbital velocity and $v_{\rm w}$ is the speed of the slowest wind (i.e., the wind of the star) at the contact surface. For the orbital parameters of LS 5039, the skew angle is below ~20° at all moments along the orbit.

5.3 Thermal X-ray emission

5.3.1 Cooling regime of the shocked stellar wind

On either side of the CD, the stellar and pulsar winds develop shocks. The shocked pulsar wind is the candidate location for particle acceleration that gives rise to the observed broadband non-thermal emission (Tavani & Arons,

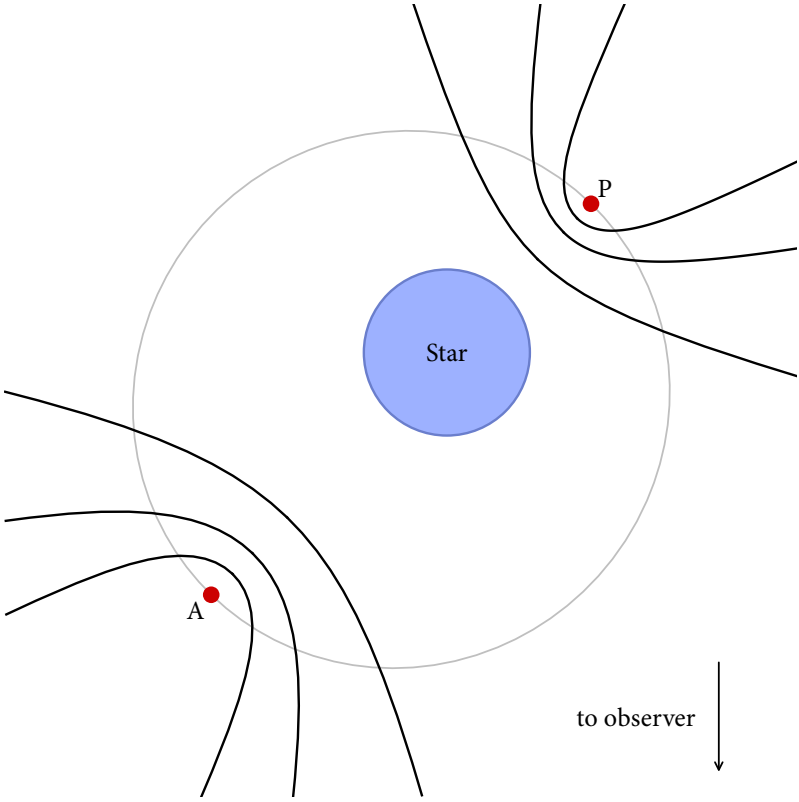

Figure 5.2: Sketch of the orbit of the compact object around the companion star in LS 5039. The star (but not the pulsar) is at scale. The two marked positions correspond to periastron (P) and apastron (A). For each of these positions the shape of the CD is shown for $\eta_\infty = 0.01, 0.04$ and 0.15

1997). On the other side of the CD, the stellar wind develops a strong shock where the wind material is slowed down and heated. The cooling efficiency of the gas determines the width of the cooling layer. On one extreme, if radiative cooling is very efficient, the gas will be rapidly cooled after the shock and will collapse into a thin dense layer on the CD. The rapid cooling assures that all the kinetic energy of the wind component perpendicular to the shock is transformed into thermal emission. On the other extreme, if radiative cooling is slow enough, the hot gas will flow along the CD and cool adiabatically through the expansion of the shocked gas layer far away from the apex of the CD. In the adiabatic regime, a smaller fraction of the kinetic energy of the stellar wind is emitted in the X-ray band. Stevens et al. (1992) proposed the parameter $\chi = t_{\rm rad}/t_{\rm esc}$ as a measure of the cooling regime of the shocked material in colliding wind binaries. Hydrodynamical simulations indicate that the wind collision regions are adiabatic for $\chi \gtrsim 3$, whereas for $\chi \lesssim 3$ they cool rapidly. Therefore, χ values around unity indicate that a significant fraction f of the incoming kinetic energy will be radiated away but the gas will not be compressed into a thin layer on the CD. For the case of LS 5039 the shocked gas cooling regime will generally be in between the two extremes, with χ values around unity, so we expect f to take values around ½.

5.3.2 Estimation of the expected X-ray luminosity

Before we enter into the details of the calculation of the thermal X-ray spectrum and luminosity, we will roughly derive the expected behaviour of the X-ray luminosity as a function of the parameters of the system. As mentioned above, we expect the X-ray luminosity to be a fraction of the perpendicular kinetic luminosity of the gas arriving onto the shock: $L_{\rm X} = f L_{\rm kin}^{\rm sh}$. Additionally, the kinetic luminosity deposited on the shock will be a fraction of the total kinetic luminosity of the stellar wind, determined by the fraction of the total solid angle of the stellar wind that is subtended by the shock, which on a first approximation can be considered to have a conical shape. For a cone with a half-opening angle of θ we obtain $L_{\rm X} \approx f\frac{1}{2}(1-\cos\theta)L_{\rm kin}^{\rm tot}$, which can be simplified up to $\mathcal{O}(\theta^4)$ as $L_{\rm X} \approx f\frac{1}{4}\theta^2 L_{\rm kin}^{\rm tot}$. Generally, the half-opening angle subtended by the shock for the stellar wind will be slightly smaller, but similar to, the half-opening angle of the CD. To obtain the estimate of the luminosity, we will here consider that the wind reaches the shock front at terminal velocity. The angle θ can then be derived from Equation (5.2) as $\pi\eta/(1+\eta)$, which on a first-order approximation for small values of η (i.e., dominance of the stellar wind) will be $\theta \approx \pi\eta$. Using these approximation we obtain $L_{\rm X} \approx f\frac{1}{4}\pi^2\eta^2 L_{\rm kin}^{\rm tot}$. Assuming constant stellar mass loss rate, η will only

depend on $L_{\rm sd}$ as $\eta \propto L_{\rm sd}$, as seen in Equation (5.1). Therefore, we expect the emitted thermal X-ray luminosity from the shocked stellar wind to behave roughly as $L_{\rm X} \propto L_{\rm sd}^2$. In addition, we can estimate the order of magnitude of the luminosity for the case of a dominant stellar wind:

$$L_{\rm X} \approx 1.2 \times 10^{32} \left[\frac{L_{\rm sd}}{10^{36}\,{\rm erg\,s^{-1}}}\right]^2 \left[\frac{\dot{M}}{10^{-7}\,{\rm M_\odot/yr}}\right]^{-1} {\rm erg\,s^{-1}}, \qquad (5.3)$$

where we have assumed that half of the kinetic energy is converted into X-ray luminosity, i.e., $f = 0.5$, and the wind terminal velocity is $v_\infty = 2400\,{\rm km/s}$. LS 5039 is an X-ray source with luminosities of several $10^{33}\,{\rm erg\,s^{-1}}$. Therefore, as Eq. (5.3) shows, pulsar spin-down luminosities moderately higher than $10^{36}\,{\rm erg\,s^{-1}}$ would imply a significant thermal component in the X-ray spectrum. In such a case, the observed X-ray spectrum should begin to deviate from an absorbed power law.

The above approximations will only hold for small values of η, i.e., for the case of a dominant stellar wind. When the ram pressure of the pulsar wind is similar to that of the stellar wind and η approaches unity, the half-opening angle of the CD will approach $\pi/2$. At this limit, the X-ray luminosity will be of the order of

$$L_{\rm X} \approx 3 \times 10^{34} \left[\frac{\dot{M}}{10^{-7}\,{\rm M_\odot/yr}}\right] {\rm erg\,s^{-1}},$$

which, for reasonable values of $\dot{M}$, is higher than the X-ray luminosity of LS 5039.

5.3.3 X-ray emission model details

Once we estimated that for reasonable values of $L_{\rm sd}$ the thermal component could be detected, we performed detailed calculations to obtain the thermal spectrum emitted by the shocked stellar wind. In the present Section we detail the approach we took to model the properties of the shocked gas and its emission.

We consider a strong, steady, standing shock with a compression ratio

$$\frac{\rho_0}{\rho_{\rm w}} = \frac{v_{\rm w\perp}}{v_{0\perp}} = 4,$$

where the subindices w and 0 indicate the properties of the gas immediately before and after the shock, respectively. The gas will then have an immediate postshock temperature of

$$kT_0 = \frac{3}{16}\mu m_p v_{\rm w\perp}^2 \approx 1.21 \left[\frac{\mu}{0.62}\right] \left[\frac{v_{\rm w\perp}}{1000\,{\rm km/s}}\right]^2 {\rm keV}, \qquad (5.4)$$

where $v_{w\perp}$ indicates the preshock speed of the wind component perpendicular to the shock front and μ is the average atomic weight. A value of $\mu = 0.62$ is appropriate for a fully ionized medium with solar abundances (Anders & Grevesse, 1989).

The X-ray emission of the shocked stellar gas is computed assuming that, in the emitting plasma, conditions are equal to those in the immediate postshock position, which is true as long as the gas remains subsonic. This will provide an estimate of how much of the kinetic energy of the incoming wind will be converted into X-ray emission. Assuming the shocked gas acts as a calorimeter, in which all the incoming perpendicular kinetic energy is either converted into X-ray emission or dissipated through adiabatic expansion, the fraction of the kinetic energy converted to X-ray emission will be

$$L_X = \frac{t_{rad}^{-1}}{t_{rad}^{-1} + t_{esc}^{-1}} L_{kin}, \tag{5.5}$$

where the t_{rad} is the radiative cooling timescale, t_{esc} is the escape or flow dynamics timescale and L_{kin} is the incoming kinetic energy. Given that $\dot{E} \propto t^{-1}$, the fraction of cooling times may be interpreted as the fraction of the radiated energy over the total lost energy owing to radiation and particle escape.

For a gas cooling with a volumetric emission rate $\Lambda(T)$, the radiative cooling timescale is given approximately by

$$t_{rad} = \frac{kT_0}{n_0 \Lambda(T_0)},$$

where n_0 is the postshock number density and in a strong shock will be four times the preshock wind number density. Instead of using a pre-calculated table for $\Lambda(T)$, we calculate it using the same MEKAL code we will use to compute the emitted spectrum.

The escape timescale is the time the heated gas takes to flow away from the postshock location. Assuming that the stellar wind overpowers the pulsar wind (see Sect. 5.4), we can use the distance from the CD to the pulsar as the radius of curvature of the shock front, and thus as a typical flow dynamics distance scale. The escape timescale can then be approximated as $t_{esc} = r_p/v_0$. We assume that the wind velocity component parallel to the shock is unaffected after traversing it, so that the immediate postshock speed may be found as $v_0^2 = (v_{w\perp}/4)^2 + v_{w\parallel}^2$.

We used the MEKAL code as implemented in the SPEX software package (Kaastra et al., 1996) to generate a look-up table of emission spectra for optically thin hot gas in collisional ionization equilibrium as a function of the gas temperature T. We populated the look-up table with emission spectra in

the 0.05–15 keV range for 250 logarithmically spaced temperatures from 10^4 to 10^9 K. Additionally, for each of the temperatures we computed the volumetric emissivity rate $\Lambda(T)$ by integrating the computed emission spectra between photon energies of 0.001 and 50 keV.

In order to compute the total cumulative emission from the shocked stellar wind we assumed that the X-ray emitter is infinitely thin and located on the CD defined through Equation (5.2). We defined a grid on the shock front of 2000 bins in the y direction, away from the line of centers, and 30 azimuthal bins. For each segment of the grid we computed the immediate post-shock temperature T_0 and X-ray luminosity through Equations (5.4) and (5.5). Using the X-ray emission look-up table, we obtained the intrinsic X-ray emission spectrum from each segment. Finally, we computed the neutral hydrogen column density from each of the positions of the segments on the shock front to the observer owing to the non-shocked stellar wind. To do so we assumed that neither the enhanced density of the shocked stellar wind nor the free pulsar wind contribute significantly to the total column density. The column density of former can be estimated to be two orders of magnitude below the wind column density (Szostek & Dubus, 2011) and the latter is too rarefied to absorb X rays. We then computed the energy-dependent attenuation factor corresponding to the found column density through the `wabs` subroutine provided with Xspec v12. In addition, the emission from those areal segments eclipsed by the star was discarded. The resulting absorbed emission from each of the areal segments was added together to compute the final emitted spectrum of the shocked stellar wind.

From the calculations described in this Section, we can see what the general characteristics of the shocked stellar wind emission will be. Along the line of centers of the system we will find both the highest temperatures and the highest densities. The hardest X rays will come from this location, but its volume is relatively small and their luminosity may not dominate the final emission. Away from this point temperatures will drop rapidly as the incoming wind will not be perpendicular to the shock, whereas the volume increases and density decreases. This region will produce a softer X-ray spectrum. The final spectrum will be a so-called multi-temperature X-ray spectrum resulting from the emission of the stratified temperature structure of the shocked gas.

5.3.4 Caveats of the model

The semi-analytic model detailed in the previous section is robust given that the assumptions made are fairly conservative. However, there are some fac-

tors that affect the wind collision region that cannot be accounted for in our semi-analytic framework. Detailed hydrodynamical simulations would be required to take into account effects such as:

- In the radiative cooling regime the CD may be disrupted by thin-shell instabilities (Stevens et al., 1992; Pittard, 2009). Additionally, stellar wind clumping would likely disturb the CD to some extent. This would have implications for both the thermal and non-thermal emission.
- We modeled the radiative output of the post-shock gas through the ratio of radiative cooling timescale to total cooling timescale in Eq. (5.5), and assumed an infinitely thin cooling layer. Both the intrinsic X-ray luminosity and cooling layer width could be calculated self-consistently through hydrodynamical simulations. Whereas the results are likely to be very similar in the radiative cooling regime limit, they will probably differ in the adiabatic limit. In the adiabatic limit of the posthock flow, the flow may become supersonic at a distance smaller than $r_{\rm p}$, cooling the gas and reducing the radiative outcome. This effect would not be important at scales similar to x_0, but could affect the contribution produced at the perifery of the system.

5.4 Stellar mass-loss rate and pulsar spin-down luminosity in LS 5039

As explained in Sect. 5.2, the shape of the CD depends only on the parameter η, which in turn depends only on the ram pressure of the winds on either side of the CD. Casares et al. (2005) derived that the O6.5V((f)) star in LS 5039 has a stellar radius of $R_\star = 9.3\,{\rm R}_\odot$, its wind has a terminal velocity of $v_\infty = 2400$ km/s and the orbital inclination is in the range 20°–70°. Therefore, the only parameters still unknown that affect the shape of the CD are the stellar mass-loss rate, $\dot{M}$, and the pulsar spin-down luminosity, $L_{\rm sd}$.

Sarty et al. (2011) performed an optical photometric and spectroscopic campaign on LS 5039, and determined the mass-loss rate of the star to be in the range 3.7 to $4.8 \times 10^{-7}\,{\rm M}_\odot$/yr from H$\alpha$ line measurements. However, Hα line fitting is a diagnostic known to be affected by wind clumping, and owing to its ρ^2 dependence could easily overpredict mass-loss rates by a factor ~2 (Markova et al., 2004). The lack of variability of the column density measured in X-ray observations along the orbit may also be used to constrain the maximum value of mass-loss rate. Bosch-Ramon et al. (2007) concluded that, considering a non-thermal X-ray emitter inside the binary system, the mass-loss rate could not exceed a few $10^{-8}\,{\rm M}_\odot$/yr. If the non-thermal source is

taken to be extended located along the CD, as would be expected in the pulsar wind scenario, this upper limit is relaxed up to 1.5×10^{-7} $M_\odot$/yr (Szostek & Dubus, 2011). In the following calculations we considered the whole range of mass-loss rates discussed here, i.e., from 5×10^{-8} $M_\odot$/yr to 4.8×10^{-7} $M_\odot$/yr. For some cases where a single representative mass-loss rate is used to test other properties of the thermal emission, we chose the midpoint of the range: $\dot{M} = 2.65 \times 10^{-7}$ $M_\odot$/yr.

The spin-down luminosity of the putative pulsar in LS 5039 is not known as it has never been measured directly. A lower limit may be derived from efficiency considerations taking into account the HE gamma-ray emission detected by *Fermi*/LAT (Abdo et al., 2009). The detected flux above 100 MeV of 2.55×10^{-10} erg cm^{-2} s^{-1} implies, if the HE gamma-ray emission has a magnetospheric origin, a spin-down luminosity of between 0.2 and 30×10^{36} erg s^{-1} depending on the beaming model (see Section 4.5.2 for an explanation of the derivation of these values for the case of LS I +61 303). However, the observed orbital modulation of the HE gamma-ray emission, and the lack of pulsations, might indicate that its origin is not magnetospheric but rather IC.

The minimum non-thermal luminosity required for the *Fermi* emission of LS 5039 can also be estimated in the context of IC radiation. To obtain a conservative estimate, one can assume that electrons are injected only in the relevant energy range, ~1–100 GeV, emit isotropically, and have time to cool down only through IC. Stellar IC leading to photons in the *Fermi* band occurs in the Thomson regime. Since this process is strongly anisotropic ($L_{\rm IC} \propto (1 - \cos\theta_{\rm IC})^{(p+1)/2}$ with p being the electron power-law index; e.g. Dermer et al. 1992), one needs to account for the IC interaction angle $\theta_{\rm IC}$. Under these conditions, the injection luminosity of electrons can be written as:

$$L_{\rm e} \approx 1.7 \, \frac{2^{\alpha+1} \, L_{\rm GeV}}{2(\alpha+1)(1-\cos\theta_{\rm IC})^{\alpha}} \, ,$$

where the factor 1.7 accounts for the luminosity radiated $\lesssim$ 100 MeV, $\alpha = (p+1)/2$, and $\theta_{\rm IC} \leq \pi/2$ for phases around the inferior conjunction. Taking $L_{\rm GeV} \approx 2 \times 10^{35}$ erg s^{-1} (Abdo et al., 2009) during those orbital phases, $p \sim 3$ to explain the *Fermi* spectrum, and a rather large $\theta_{\rm IC} \approx 60°$, one obtains $L_{\rm e} \approx 2 \times 10^{36}$ erg s^{-1}. However, escape, adiabatic and perhaps synchrotron losses could easily increase $L_{\rm e}$ by a factor of several. In addition, not all the $L_{\rm sd}$ will go to non-thermal particles*, and the injection electron distribution is expected to be broader than ~1–100 GeV. From all this, $L_{\rm sd} \gtrsim 2 \times 10^{37}$ erg s^{-1}

* Not only is the acceleration efficiency unlikely to be 100%, but for higher spin-down luminosities the opening angle of the CD will increase and only around half of the pulsar wind luminosity will be shocked.

seems more realistic. Doppler boosting has not been accounted for but, although it can reduce the required energy budget in certain orbital phases, it will increase it in others. Note that for $\theta_{\rm IC} \approx 90^\circ$ and phases between inferior and superior conjunction, i.e. with the flow bulk motion unlikely pointing to us, still $L_{\rm e} \gtrsim 10^{36}\,{\rm erg\,s^{-1}}$, and thus $L_{\rm sd} \gtrsim 10^{37}\,{\rm erg\,s^{-1}}$. The GeV emitter may be extended, but it should not change significantly our conclusion.

5.5 Comparison to X-ray data

5.5.1 X-ray observations

LS 5039 has been observed at different positions along its orbit by many X-ray observatories (see Zabalza et al., 2008, for a summary). Recently, a very long observation with *Suzaku* provided an uninterrupted lightcurve of the source during an orbit and a half (Takahashi et al., 2009), and a comparison with previous observations indicated that it was quite stable over periods of up to a decade (Kishishita et al., 2009). The *Suzaku* observation provides a very good orbital coverage, but we have chosen, to compare the output of our numerical model, two *XMM-Newton* observations performed in 2005 (Bosch-Ramon et al., 2007). The superior effective area of *XMM-Newton* gives us the possibility to extract very good soft X-ray spectra in relatively short observations. These short observations ($\Delta\phi \sim 0.05$) assure that the ambient conditions do not vary significantly and the measured spectra can be accurately compared to spectra calculated for a given phase. These two ~15 ks observations were performed at periastron (obsid 0202950301, orbital phases 0.02–0.05) and apastron (obsid 0202950201, orbital phases 0.49–0.53) during the same orbital period, thus probing the two extreme separations between the star and the compact object.

For each of the two observations we processed the data trough the standard procedure with version 10.0 of the *XMM-Newton* Science Analysis Software (SAS). We filtered out the periods of high particle background for each of the three detectors aboard *XMM-Newton* and extracted source and background spectra from the clean event files, as well as the corresponding redistribution matrix (RMF) and ancillary response (ARF) files. We binned the extracted source spectra to a minimum of 20 counts per bin avoiding an oversampling of the detector energy resolution by more than a factor 3.

Before introducing the model corresponding to our calculations of the thermal X-ray emission of the shocked stellar wind, we performed a fit of the data to an absorbed power-law using the spectral analysis package *Sherpa*

Orb. phase	Parameter	Source model	
		$A_{\rm ISM} \times P$	$A_{\rm ISM} \times (P + Th)$
Periastron	$N_{\rm H}$[a]	0.67 ± 0.02	0.60 ± 0.03
	Γ	1.57 ± 0.04	1.44 ± 0.04
	$F(P)$[b]	7.1 ± 0.6	6.1 ± 0.6
	$F(Th)$[b]	···	0.53
Apastron	$N_{\rm H}$[a]	0.67 ± 0.02	0.75 ± 0.02
	Γ	1.47 ± 0.03	1.43 ± 0.03
	$F(P)$[b]	11.4 ± 0.7	10.7 ± 0.7
	$F(Th)$[b]	···	0.96
	$L_{\rm sd}$	···	5.82×10^{36} erg/s
	χ^2/dof	467.5/610	476.6/611

Table 5.1: Results of the X-ray spectral analysis. For the calculation of the thermal component *Th*, a mass-loss rate of 2.65×10^{-7} $M_\odot$/yr and an inclination of 45° have been assumed. Notes: a) Interstellar column densities are in units of 10^{22} cm^{-2}. b) ISM unabsorbed X-ray fluxes of the non-thermal power law (*P*) and the thermal shocked stellar wind (*Th*) components in the range 0.3–10 keV are given in units of 10^{-12} erg cm^{-2} s^{-1}.

(Freeman et al., 2001) bundled with CIAO 4.3. The fit results for this strictly non-thermal source model may be found in the third column of Table 5.1.

5.5.2 *Method of spin-down luminosity upper-limit derivation*

To accurately compare the output of our model of thermal X-ray emission from the shocked stellar wind described in sections 5.2 and 5.3 with the observed spectra, we formatted the computed X-ray spectra as a FITS table model that could be loaded by the spectral analysis software package *Sherpa*. We computed the cumulative spectra for 25 pulsar spin-down luminosities spaced logarithmically between 10^{36} erg s^{-1} and 5×10^{37} erg s^{-1}, taking a constant value of the mass-loss rate. The normalization was initially fixed to unity but can be used to account for different distances to the source when set to $(2.5\,{\rm kpc}/d)^2$, where d is the distance in kiloparsecs.

We assigned each of the two groups of spectra (periastron, p, and apastron, a) a source model corresponding to an interstellar medium neutral hydrogen photoelectric absorption component (A) affecting both the non-thermal power law (P) and the computed shocked stellar wind thermal emission (Th): $A_{\rm ISM}^{\rm p,a} \times (P^{\rm p,a} + Th^{\rm p,a})$. Whereas all the parameters of the absorption and power

law components were left free for the spectral fitting, the spin-down luminosity of the pulsar was linked between the periastron and apastron models. We note that such a choice for the source model implies that the non-thermal emission is not significantly affected by circumstellar absorption, whereas the thermal emission is. This would happen for either extended non-thermal emitters or very low circumstellar absorption (see Sect. 5.7.1 below for a discussion).

In order to derive the spin-down luminosity upper limit we performed a simultaneous fit of the six spectra (three detectors for each of the two orbital phases). In all cases, the best fit corresponded to the lowest level of emission from the thermal component, i.e., the non-thermal component alone provided the best fit to the data. As expected from the rough estimate (see Sect. 5.3.2), the X-ray luminosity of the thermal component increased monotonically with the value of the spin-down luminosity of the pulsar. The goal is then to find for which value of the spin-down luminosity the thermal component begins to affect the shape of the spectrum and the fit worsens significantly. We used the `confidence` *Sherpa* command to evaluate the 99.7% (3σ) confidence level range for acceptable values of the spin-down luminosity. In all cases the lower bound was consistent with zero, i.e., lack of thermal component. The upper bound, on the other hand, provides us with the upper limit to the spin-down luminosity of the pulsar.

5.6 Results

5.6.1 Thermal X-ray spectra

We used the dynamical, radiative and absorption model described above to calculate the thermal X-ray spectra emitted by the shocked stellar wind gas. In accordance with the estimates of Sect. 5.3.2, we have found that in general the thermal X-ray luminosities increase monotonically with the spin-down luminosity of the pulsar. In Fig. 5.3 we show the 0.3–10 keV X-ray luminosity of the thermal emission from the shocked stellar wind as a function of the pulsar spin-down luminosity, taking $\dot{M} = 2.65 \times 10^{-7}\,\mathrm{M_\odot/yr}$. For scenarios with a dominance of the stellar wind (i.e., $L_{\rm sd} \lesssim 10^{37}\,\mathrm{erg\,s^{-1}}$), the behavior is generally in good agreement with Eq. (5.3). At higher spin-down luminosities, the proximity of the CD to the stellar surface at periastron provokes a decrease in the total intrinsic X-ray luminosity.

Figure 5.4 shows the obtained intrinsic and absorbed spectra for different values of the spin-down luminosity ranging from $3 \times 10^{35}\,\mathrm{erg\,s^{-1}}$ to $3 \times 10^{37}\,\mathrm{erg\,s^{-1}}$. The mass-loss rate of $2.65 \times 10^{-7}\,\mathrm{M_\odot/yr}$ assumed for these spec-

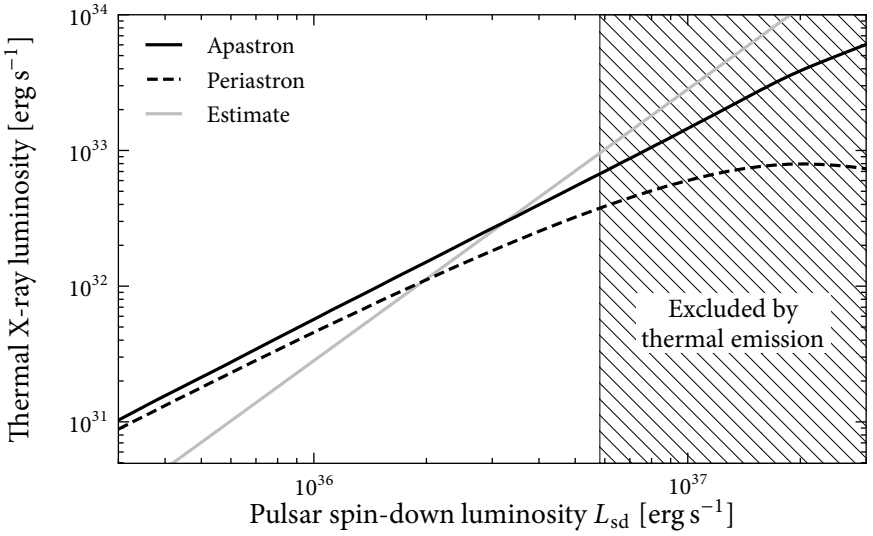

Figure 5.3: Thermal emission luminosity in the 0.3–10 keV range as a function of the spin-down luminosity of the pulsar. The fluxes at periastron (dashed) and apastron (solid) are shown. In addition, the rough estimate of Equation 5.3 is shown as a gray line. The range of pulsar spin-down luminosities excluded by the thermal emission is shown as a hatched region. In all cases, a mass-loss rate of $2.65 \times 10^{-7}\,M_\odot/\mathrm{yr}$ was assumed.

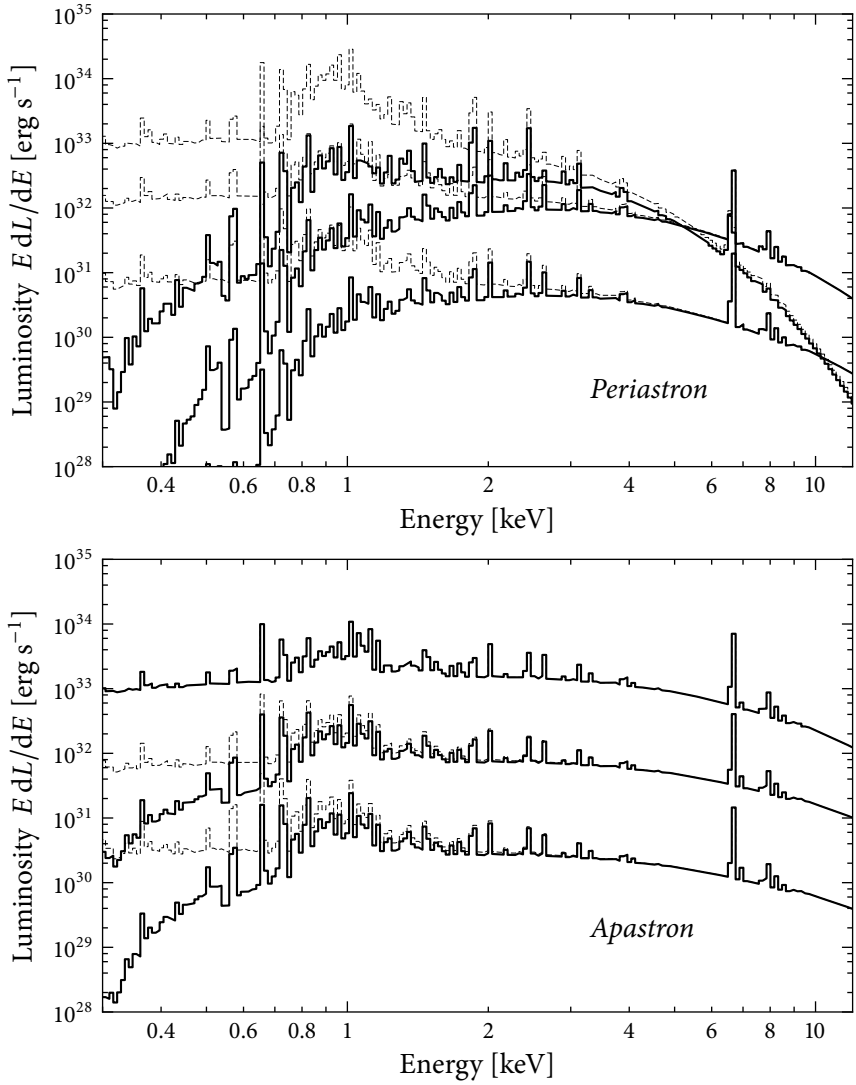

Figure 5.4: X-ray emission computed from the shocked stellar wind of LS 5039 at periastron (top) and apastron (bottom), taking $\dot{M} = 2.65 \times 10^{-7}\,M_\odot$/yr and $i = 45°$. The different spectra for each orbital phase correspond to different values of pulsar spin-down luminosity L_{sd}: 0.3 (bottom), 3 (middle) and 30 (top) $\times 10^{36}$ erg s^{-1}, corresponding to $\eta_\infty = 0.0025$, 0.025 and 0.25, respectively. The thin dashed lines indicate the intrinsic spectra, whereas the thick solid ones are the ones absorbed owing to the stellar wind.

tra provides a dense matter field in the binary. Its effect can be seen as a very strong absorption at energies below 1 keV for the periastron spectrum. The column density at this phase is of the order of 10^{22} cm^{-2}, even higher than the measured interstellar one. In contrast, the apastron spectrum for the highest spin-down luminosity shows negligible circumstellar absorption. This is because, at apastron, the pulsar would be close to inferior conjunction, and the high opening angle of the CD would mean that most of the thermal X-ray emission only has to travel through the unshocked stellar wind to reach the observer (see Fig. 5.2), thus being barely absorbed. As discussed in Sect. 5.3.3, the hardest X rays will come from the region around the apex of the CD. For high values of the spin-down luminosity, the apex of the CD at periastron will be closer to the stellar surface, and the velocity of the incoming wind will be lower owing to the β wind velocity law. Therefore, the X-rays from the apex will be softer, an effect that can be seen in the high energy part of the topmost spectrum of Fig. 5.4. For the parameters used to compute this spectrum, the stagnation point of the CD is at only 0.39 stellar radii from the surface of the star and the wind velocity at the shock is about one third of the terminal velocity. Note how this effect is not apparent in the corresponding apastron spectra, for which the stagnation point is much farther from the stellar surface.

5.6.2 Spin-down luminosity upper limits

To derive the upper limits of the pulsar spin-down luminosity we chose to explore the range of stellar mass-loss rate values mentioned in Sect. 5.4, corresponding to the estimates of Bosch-Ramon et al. (2007), Szostek & Dubus (2011) and Sarty et al. (2011): 5×10^{-8} M$_\odot$/yr, 1.5×10^{-7} M$_\odot$/yr and 4.25×10^{-7} M$_\odot$/yr, respectively. The orbital inclination will affect the importance of circumstellar absorption, particularly at periastron, in the emitted spectrum, so we have also explored the whole range delimited by Casares et al. (2005), $i = 20°$–$70°$. The result of the pulsar spin-down luminosity upper-limit determination for the whole ranges of mass-loss rate and orbital inclination is shown in Figure 5.5. A summary of the results for the extremes and midpoints of the ranges can be seen in Table 5.2.

We found that pulsar spin-down luminosities above 6.3×10^{36} erg s^{-1} are excluded by the lack of spectral thermal features in the observed periastron and apastron spectra for any combination of mass-loss rates and orbital inclinations. This upper-limit corresponds to the extreme inclination of 70°, and for moderate orbital inclinations the upper-limit is at all times below 6×10^{36} erg s^{-1}. While the wind kinetic luminosity available for $\dot{M} = 5 \times$

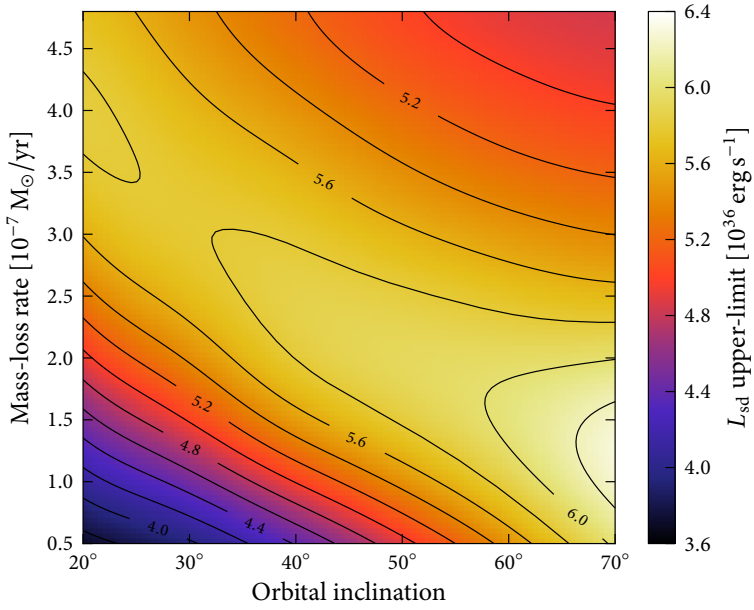

Figure 5.5: Spin-down luminosity upper-limits as a function of orbital inclination and stellar mass-loss rate.

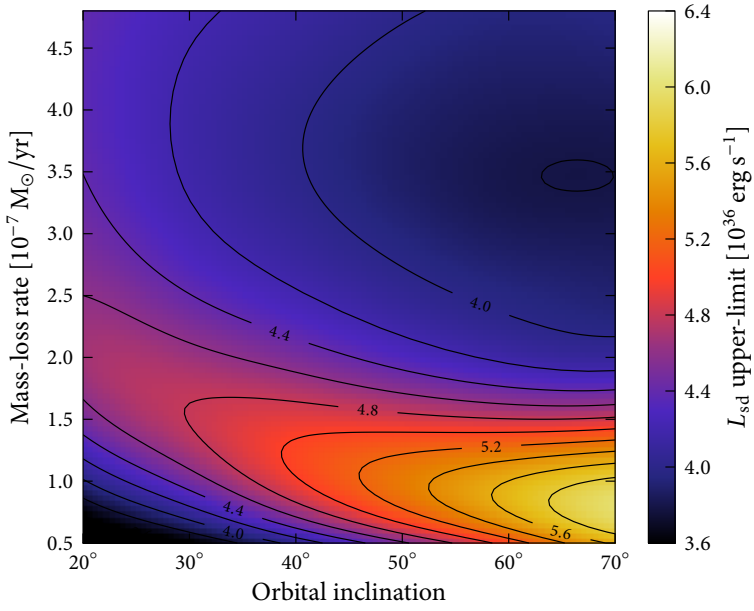

Figure 5.6: As above, but linking the ISM absorption between apastron and periastron.

Mass-loss rate ($M_\odot$/yr)	Inclination	L_{sd} upper-limit (10^{36} erg s^{-1})
5×10^{-8}	20°	3.7
	45°	4.7
	70°	6.0
1.5×10^{-7}	20°	4.5
	45°	5.6
	70°	6.3
4.25×10^{-7}	20°	5.8
	45°	5.2
	70°	4.9

Table 5.2: Pulsar spin-down luminosity upper limits as a function of orbital inclination and stellar mass-loss rate.

10^{-8} $M_\odot$/yr is lower than for the other cases, the upper limits derived are at least as strict as for higher mass-loss rates. We found that the reduced absorption owing to the lower density of the stellar wind results in brighter emission below 1 keV. In the last column of Table 5.1 we show the best-fit results of the thermal plus non-thermal source model with the spin-down luminosity of the pulsar fixed at the upper limit we found for the midpoint values of mass-loss rate and orbital inclination. As compared to the non-thermal source model, the best fit power law is slightly harder and its unabsorbed flux is ~10% lower. In addition, the required interstellar column densities cease to be constant between apastron and periastron. An illustration of the thermal and non-thermal contributions to the observed spectrum is shown in Fig. 5.7.

We note that if we force the value of the ISM photoelectric absorption to remain constant between the fits of periastron and apastron spectra the upper limits are considerably more strict. For the midpoint situation with $\dot{M} = 2.65 \times 10^{-7}$ $M_\odot$/yr and $i = 45°$, the pulsar spin-down upper limit is reduced from 5.82×10^{36} erg s^{-1} down to 4.08×10^{36} erg s^{-1}. As can be seen in Figure 5.6, the pulsar spin-down upper limits are more restrictive. Except for a small parameter space region at high inclination and low mass-loss rates, this results in upper limits below 5×10^{36} erg s^{-1}.

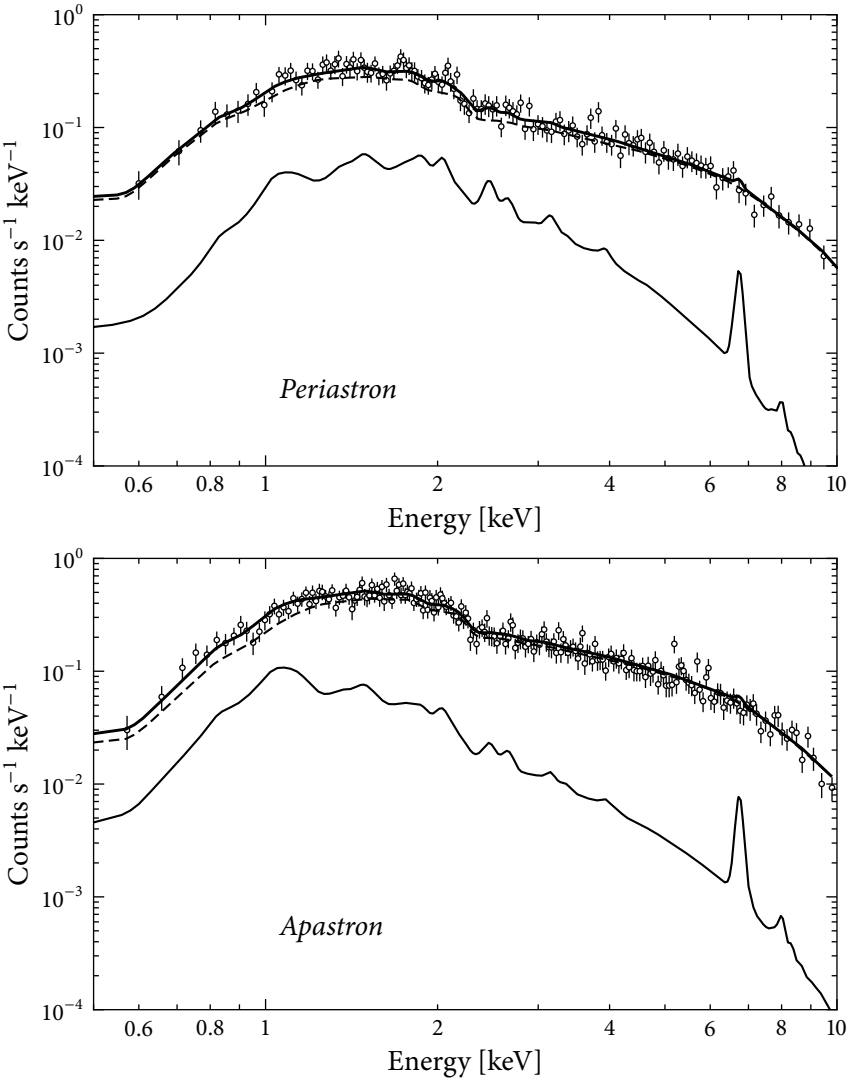

Figure 5.7: X-ray spectra of LS 5039 at periastron (top) and apastron (bottom). The open circles are the data from the pn detector. The MOS data are fit simultaneously but not shown here for clarity. The lines indicate the best fit spectral model for the spin-down luminosity fixed at the upper limit for moderate values of orbital inclination and stellar mass-loss rate: $L_{\rm sd} = 5.82 \times 10^{36}$ erg s^{-1}. The thick solid line is the sum of the non-thermal power-law component (thin dashed) and the shocked stellar wind thermal component (thin solid). The energy resolution of the thermal component is lower than in Fig. 5.4, which results from folding the spectral models with the energy redistribution matrix of the detector

5.7 Discussion

5.7.1 On the stellar mass-loss rate

The strength of stellar mass-loss rate plays a double role in the PWS scenario. On one hand it determines the shape of the CD and the kinetic luminosity that is shocked onto the CD. On the other hand, it determines the importance of photoelectric absorption in the X-ray spectra of the thermal and non-thermal radiation sources.

The lack of X-ray absorption variability in LS 5039 along the orbit indicates that the stellar wind density must be low if the non-thermal emitter is inside the orbital system. However, a very low value will result in the pulsar wind overpowering the stellar wind for reasonable values of the pulsar spin-down luminosity. We have found that the maximum mass-loss rate possible compatible with a variation of the neutral hydrogen column density along the orbit below 10^{21} cm^{-2} (Bosch-Ramon et al., 2007) is of $\sim 5 \times 10^{-8}$ M$_\odot$/yr. For such a low mass-loss rate, the pulsar wind could impact on the stellar surface at periastron for reasonable values of spin-down luminosity. However, the lack of orbital variations of the UV spectra of LS 5039 (McSwain et al., 2004) indicate that the stellar surface is not perturbed at any point along the orbit. This places an upper limit on spin-down luminosities of $\sim 7 \times 10^{36}$ erg s^{-1}. However, if the star has a strong enough surface magnetic field, then magnetic pressure could be enough to balance the pulsar wind away from the surface (Harding & Gaisser, 1990). For a surface magnetic field of 50 G and assuming a dipole field, the spin-down luminosity could be as high as 3×10^{37} erg s^{-1} without the CD collapsing onto the stellar surface.

However, if a significant fraction of the non-thermal emitter is not located deep inside the binary system the X-ray absorption may be reduced. The photoelectric absorption of the thermal and non-thermal X-ray emission could then be decoupled (as we have done in Sect. 5.5.2) since their locations would be different. For this scenario, the stellar mass-loss rate could be as high as a few times 10^{-7} M$_\odot$/yr, as measured by Sarty et al. (2011). Additionally, such a location would favor the acceleration of particles up to the very high energies required to account for the VHE gamma-ray spectrum (Khangulyan et al., 2008; Bosch-Ramon et al., 2008).

5.7.2 On the pulsar spin-down luminosity

The upper limits we have found on the spin-down luminosity of the pulsar pose strong constraints on further modeling of the PWS scenario for non-

thermal emission. As discussed in Sect. 5.4, the pulsar spin-down luminosity should be at least a few times $10^{36}\,\mathrm{erg\,s^{-1}}$ in order to account for the GeV emission. The upper limit we have found from the thermal X-ray emission ($L_{\mathrm{sd}} < 6 \times 10^{36}\,\mathrm{erg\,s^{-1}}$) indicates that the spin-down luminosity must be very close to this value in order for the PWS scenario to be consistent. A detailed modeling of the GeV emission from LS 5039 is required to accurately check the consistency of the observed GeV luminosity and the PWS scenario. Unfortunately, the structure of the GeV emitter is not well known, and IC emission is very sentive to the θ_{IC}-value, which makes difficult to obtain conclusive results. Nevertheless, the lower limit derived here for L_{e}, in the IC scenario, is still robust enough to show that, likely, $L_{\mathrm{e}}/L_{\mathrm{sd}} \to 1$.

The recent detection of PSR B1259−63 at GeV energies (Tam et al., 2011; Abdo et al., 2011) provides a perfect comparison of the efficiency of spin-down luminosity to non-thermal emission conversion efficiency. During its highest state of emission the total gamma-ray luminosity was comparable to the pulsar spin-down luminosity. Whereas the X-ray emission lightcurve is symmetric with respect to periastron and correlated with Be disc passages (Chernyakova et al., 2009), the HE gamma-ray emission after periastron was a factor 20–30 higher than before periastron. This indicates that anisotropy of the gamma-ray emission is at play. Possible sources of anisotropy, in addition to the intrinsic θ_{IC}-dependent IC anisotropy, include relativistic beaming of the emitting outflow (Bogovalov et al., 2008), anisotropy of the pulsar wind, and anisotropy of the radiation field of the star (Negueruela et al., 2011). However, even considering Doppler boosting, the efficiency of the shocked pulsar wind in converting the spin-down luminosity into non-thermal HE gamma-ray emission is extremely high.

5.7.3 Concluding remarks

The semi-analytic model presented here has allowed us to gain valuable insight into the nature of LS 5039. The assumptions described in Sect. 5.3.3 are chosen such that the resulting level of thermal X-ray emission is fairly conservative and thus the upper limit on the spin-down luminosity robust. We have shown that the study of the thermal emission from the shocked stellar wind can be a powerful diagnostic tool for pulsar gamma-ray binaries. Even for cases where no thermal features are observed in the X-ray spectrum it can be used to place constraints on important properties of the system such as stellar mass-loss rate and pulsar spin-down luminosity.

References

Abdo, A. A., et al. 2009, ApJ, 706, L56

—. 2011, ApJL, submitted, arXiv:1103.4108

Aharonian, F., et al. 2006, A&A, 460, 743

Anders, E., & Grevesse, N. 1989, Geochim. Cosmochim. Acta, 53, 197

Antokhin, I. I., Owocki, S. P., & Brown, J. C. 2004, ApJ, 611, 434

Bogovalov, S. V., Khangulyan, D. V., Koldoba, A. V., Ustyugova, G. V., & Aharonian, F. A. 2008, MNRAS, 387, 63

Bosch-Ramon, V., Khangulyan, D., & Aharonian, F. A. 2008, A&A, 489, L21

Bosch-Ramon, V., Motch, C., Ribó, M., Lopes de Oliveira, R., Janot-Pacheco, E., Negueruela, I., Paredes, J. M., & Martocchia, A. 2007, A&A, 473, 545

Casares, J., Ribó, M., Ribas, I., Paredes, J. M., Martí, J., & Herrero, A. 2005, MNRAS, 364, 899

Cerutti, B., Dubus, G., & Henri, G. 2009, A&A, 507, 1217

Chernyakova, M., Neronov, A., Aharonian, F., Uchiyama, Y., & Takahashi, T. 2009, MNRAS, 397, 2123

Dermer, C. D., Schlickeiser, R., & Mastichiadis, A. 1992, A&A, 256, L27

Dubus, G. 2006, A&A, 456, 801

Freeman, P., Doe, S., & Siemiginowska, A. 2001, in Presented at the Society of Photo-Optical Instrumentation Engineers (SPIE) Conference, Vol. 4477, Society of Photo-Optical Instrumentation Engineers (SPIE) Conference Series, ed. J.-L. Starck & F. D. Murtagh, 76–87

Harding, A. K., & Gaisser, T. K. 1990, ApJ, 358, 561

Kaastra, J. S., Mewe, R., & Nieuwenhuijzen, H. 1996, in UV and X-ray Spectroscopy of Astrophysical and Laboratory Plasmas, ed. K. Yamashita & T. Watanabe, 411–414

Khangulyan, D., Aharonian, F., & Bosch-Ramon, V. 2008, MNRAS, 383, 467

Khangulyan, D., Hnatic, S., Aharonian, F., & Bogovalov, S. 2007, MNRAS, 380, 320

Kirk, J. G., Ball, L., & Skjaeraasen, O. 1999, Astroparticle Physics, 10, 31

Kishishita, T., Tanaka, T., Uchiyama, Y., & Takahashi, T. 2009, ApJ, 697, L1

Maraschi, L., & Treves, A. 1981, MNRAS, 194, 1

Markova, N., Puls, J., Repolust, T., & Markov, H. 2004, A&A, 413, 693

McSwain, M. V., Gies, D. R., Huang, W., Wiita, P. J., Wingert, D. W., & Kaper, L. 2004, ApJ, 600, 927

Negueruela, I., Ribó, M., Herrero, A., Lorenzo, J., Khangulyan, D., & Aharonian, F. A. 2011, ApJL, in press, arXiv:1103.4636

Paredes, J. M., Martí, J., Ribó, M., & Massi, M. 2000, Science, 288, 2340

Paredes, J. M., Ribó, M., Ros, E., Martí, J., & Massi, M. 2002, A&A, 393, L99

Pauldrach, A., Puls, J., & Kudritzki, R. P. 1986, A&A, 164, 86

Pittard, J. M. 2009, MNRAS, 396, 1743

Pittard, J. M., Dougherty, S. M., Coker, R. F., & Corcoran, M. F. 2005, in X-Ray and Radio Connections, ed. L. O. Sjouwerman & K. K. Dyer

Rea, N., Torres, D. F., van der Klis, M., Jonker, P. G., Méndez, M., & Sierpowska-Bartosik, A. 2010, MNRAS, 405, 2206

Ribó, M., Paredes, J. M., Moldón, J., Martí, J., & Massi, M. 2008, A&A, 481, 17

Sarty, G. E., et al. 2011, MNRAS, 411, 1293

Stevens, I. R., Blondin, J. M., & Pollock, A. M. T. 1992, ApJ, 386, 265

Szostek, A., & Dubus, G. 2011, MNRAS, 411, 193

Takahashi, T., et al. 2009, ApJ, 697, 592

Tam, P. H. T., Huang, R. H. H., Takata, J., Hui, C. Y., Kong, A. K. H., & Cheng, K. S. 2011, ApJL, submitted, arXiv:1103.3129

Tavani, M., & Arons, J. 1997, ApJ, 477, 439

Zabalza, V., Paredes, J. M., & Bosch-Ramon, V. 2008, International Journal of Modern Physics D, 17, 1867

6

A search for Very High Energy gamma-ray emission from Sco X-1 with the MAGIC telescopes

The acceleration of particles up to GeV or higher energies in microquasars has been the subject of considerable theoretical and observational efforts in the past few years. Sco X-1 is a microquasar from which evidence of highly energetic particles in the jet has been found when it is in the so-called Horizontal Branch, a state when accretion is lower and a powerful relativistic jet is present. In this chapter we present the first very high energy gamma-ray observations of Sco X-1 obtained with MAGIC, performed simultaneously to X-ray observations with *RXTE* in order to probe the accretion states of the source.

6.1 Introduction

It has been proposed that particles accelerated in relativistic microquasar ejections could produce detectable gamma-ray emission (Atoyan & Aharonian, 1999). A confirmation of such predictions may be found in Cygnus X-3, an accreting X-ray binary from which non-thermal emission up to energies above 100 MeV has been clearly detected (Tavani et al., 2009; Abdo et al., 2009). However, an extensive observational campaign in the very high

energy (VHE) gamma-ray band yielded no detection (Aleksić et al., 2010). Another well-known microquasar, GRS 1915+105, was observed at VHE but only upper limits were obtained (Saito et al., 2009; Acero et al., 2009). Finally, MAGIC found evidence (at a post-trial significance level of 4.1σ) for VHE gamma-ray emission from the microquasar Cygnus X-1 (Albert et al., 2007), but this has not been confirmed yet through an independent detection. See Section 1.3 for additional information on these accreting binaries and the four binaries detected so far at VHE energies (i.e., LS 5039, LS I +61 303, PSR B1259−63 and HESS J0632+057).

In the case of the microquasar Cygnus X-1, a powerful young stellar companion provides an intense target photon field for IC scattering. However, this photon field could also absorb the produced gamma rays through pair production with opacities up to 10 at 1 TeV (Bednarek & Giovannelli, 2007). Such strong absorption might not be present in the case of low-mass X-ray binaries (LMXB), where the companion star is less massive and has a much lower luminosity. Low-mass systems with persistent accretion and powerful relativistic jets could produce TeV emission via synchrotron self-Compton scattering (SSC), and would be good candidates to be detected at these energies given their continuous activity and the lack of severe absorption. However, external IC cannot be fully discarded in LMXBs given the strong accretion disc emission (Bosch-Ramon et al., 2006) and X-ray-enhanced radiation from the stellar companion, which would also increase the TeV opacities (Bednarek & Pabich, 2010).

Z sources are a class of LMXBs that contain a low magnetic field neutron star accreting close to the Eddington limit. Their X-ray intensity and colors change on timescales of hours, and their path through a hard color versus soft color diagram follows a roughly Z-shaped track (Hasinger & van der Klis, 1989). Along this track the sources change between different spectral states known as Horizontal Branch (HB), Normal Branch (NB), and Flaring Branch (FB), in order of increasing mass accretion rate. Since most LMXBs have an almost circular orbit, the accretion states are not expected to have an orbital dependence. Even though known as a Z-track, with the HB being the upper-left horizontal part of the track, in some sources it may be more accurately described as a double banana shape, with the upper banana being the part corresponding to the HB/NB states and the lower banana corresponding to the NB/FB states (Hasinger & van der Klis, 1989). Radio emission and hard X-ray power-law tails, which are strong evidence of particle acceleration up to very high energies, have been only detected while the sources are in the Horizontal Branch (Hjellming et al., 1990; Di Salvo et al., 2006).

Sco X-1, located at 2.8 ± 0.3 kpc, is a prototype Z-type low-mass X-ray binary containing a low magnetic field neutron star of 1.4 $M_\odot$ orbiting an M star of 0.4 $M_\odot$ every 0.787 d. The circular binary orbit has an inclination of 44° and a separation of ~ 1.5×10^{11} cm (see Fomalont et al. 2001, Steeghs & Casares 2002 and references therein). Accretion takes place via Roche lobe overflow. The source displays a double banana track in color-color diagrams and covers the whole track in a few tens of hours, spending roughly half of the time in the HB. Spectral fits at hard X-rays reveal a non-thermal power law with higher fluxes during the HB, reaching values in the range 10^{-10}–10^{-9} erg cm^{-2} s^{-1}, and no high-energy cutoff (Di Salvo et al., 2006; D'Aí et al., 2007). Moreover, twin relativistic radio lobes moving at ~0.5 c from the central source have been detected, while successive flaring of the core and lobes reveals the action of an unseen, highly relativistic flow with a speed above 0.95 c (Fomalont et al., 2001). All these results clearly indicate the presence of highly energetic particles when the source is in the HB, and suggest that the IC (likely SSC) process could be at work when a powerful jet is present in this spectral state. The IC process could generate VHE emission, but to adequately assess its origin simultaneous X-ray observations are required to monitor the source accretion state. Sco X-1 was claimed to be a source of TeV and PeV gamma-rays (Brazier et al., 1990; Tonwar et al., 1991), but the low significance and lack of later confirmation shed doubts on these detections.

In May 2010 we carried out a simultaneous observation campaign with the Cherenkov VHE gamma-ray telescopes MAGIC and the X-ray observatory *RXTE*. Here we present the results of the first VHE observations of Sco X-1 for selected X-ray states, focusing on the HB state, where evindence for relativistic particles in the jet has already been found.

6.2 Observations and Data Analysis

6.2.1 MAGIC

MAGIC observations were carried out in wobble mode (Fomin et al., 1994), pointing in two directions at 0.4° on opposite sides of the source. Since the source culminates at a zenith angle of 43° at La Palma, it was observed at high zenith angles, between 43° and 50°, for a total amount of 7.75 hours during six consecutive nights in May 2010. Table 6.1 shows the detailed observation log.

The data analysis procedure was the standard MAGIC analysis and can be found in more detail in Appendix A. For the case of the Sco X-1 observations, the optimization of the analysis on a Crab Nebula sample led to a sensitivity

Date (MJD)	Orbital phase	Eff. time (hours)	X-ray state	UL (> 300 GeV) ($cm^{-2}\,s^{-1}$)	C.U.
55331.09	0.26–0.38	1.28	NB/FB	7.9×10^{-12}	6.4%
55332.11	0.58–0.64	0.48	HB	5.2×10^{-12}	4.2%
55333.07	0.77–0.86	1.65	NB/FB	3.5×10^{-12}	2.8%
55334.06	0.03–0.12	1.37	HB	5.1×10^{-12}	4.1%
55335.05	0.25–0.39	1.73	HB	5.3×10^{-12}	4.3%
55336.06	0.52–0.66	1.24	NB	2.0×10^{-12}	1.6%

Table 6.1: Log of the VHE Observations. Notes: The central MJD of each observation is quoted. Upper limits are at 95% confidence level. In the last column the upper limits are indicated in units of the Crab Nebula flux (C.U.)

of 1.1% for energies above the analysis threshold of 300 GeV. The relatively low sensitivity and high energy threshold of the analysis is a consequence of the large zenith angle of the observations. For the case of non-detections, we computed flux upper limits using the method of Rolke et al. (2005) including a 30% systematic uncertainty, as explained in Section A.3.1. The source spectrum was assumed to be a power law with a photon index of $\Gamma = 3$. This photon index was taken to account for the possibility of a steeper spectrum than the Crab Nebula one, as would be the case for some of the plausible emission scenarios (see Section 6.4). However, it must be noted that a 30% change in the assumed photon index yields a variation of less than 1% in the flux upper limits. The integral upper limits quoted are at a confidence level of 95% and measured above 300 GeV.

6.2.2 X-rays

We performed *RXTE* observations of Sco X-1 simultaneously to the MAGIC VHE gamma-ray observations. To study the source X-ray spectral state, we analyzed the data from the Proportional Counter Array (PCA) instrument, which is sensitive in the range 2–60 keV. To calculate the color-color diagram of Sco X-1 we extracted Soft Color and Hard Color lightcurves in 64 s bins, where the Soft Color is defined as the ratio between the count rate in the energy bands [4.08–6.18 keV]/[1.94–4.05 keV] and the Hard Color is the ratio [8.32–16.26 keV]/[6.18–8.32 keV]. These energy ranges are equivalent to those used in previous studies of the source (e.g. D'Aí et al., 2007). The resulting color-color diagram for the whole observational campaign is shown in Fig-

X-ray state	Eff. time (hours)	Significance σ	UL (> 300 GeV)[a] ($cm^{-2}\,s^{-1}$)	C.U.
All	7.75	0.52	2.4×10^{-12}	1.9%
HB	3.58	0.72	3.4×10^{-12}	2.7%
NB/FB	4.17	0.08	2.8×10^{-12}	2.3%

Table 6.2: Integral Upper Limits for selected accretion states. Notes: Upper limits are at 95% confidence level.

ure 6.1, where it can be seen that the source practically covered the full double banana-shaped track during the observations. We selected the top part of the upper banana of the color-color diagram (indicated by a gray box in Figure 6.1) as corresponding to the HB. This selection is supported by previous observations of Sco X-1 with *RXTE*, where periods with similar color-color diagram selections were found to show the hard X-ray power-law component characteristic of the HB state (Di Salvo et al., 2006; D'Aí et al., 2007).

6.3 Results

A night by night analysis of the X-ray spectral states of Sco X-1 showed that the source did not move extensively along the Z track during any of the individual observation nights, as can be seen in Figure 6.1. During three of the six VHE observations the source was in the HB (MJD 55332, 55334 and 55335), as indicated in the observation log of Table 6.1.

The total significance (following the definition of Li & Ma, 1983) of the gamma-ray signal coming from Sco X-1 for the complete dataset of MAGIC observations, which amounts to 7.75 hours of effective time, is $S = 0.52\sigma$. For the complete dataset, the computed flux upper limit is of 2.4×10^{-12} $cm^{-2}\,s^{-1}$ above 300 GeV. The simultaneous X-ray observations allowed us to select the VHE data corresponding to each accretion state. We performed a signal search for those periods when the source was in the HB, but no significant excess was found, with a flux upper limit of 3.4×10^{-12} $cm^{-2}\,s^{-1}$ above 300 GeV. A search for a signal in the rest of the dataset, when the source was in NB and FB states, didn't produce a positive result either. A summary of these accretion-state selected results is shown in Table 6.2.

Additionally, a night-by-night analysis was performed. In none of the six observations a significant signal was found, with the corresponding flux up-

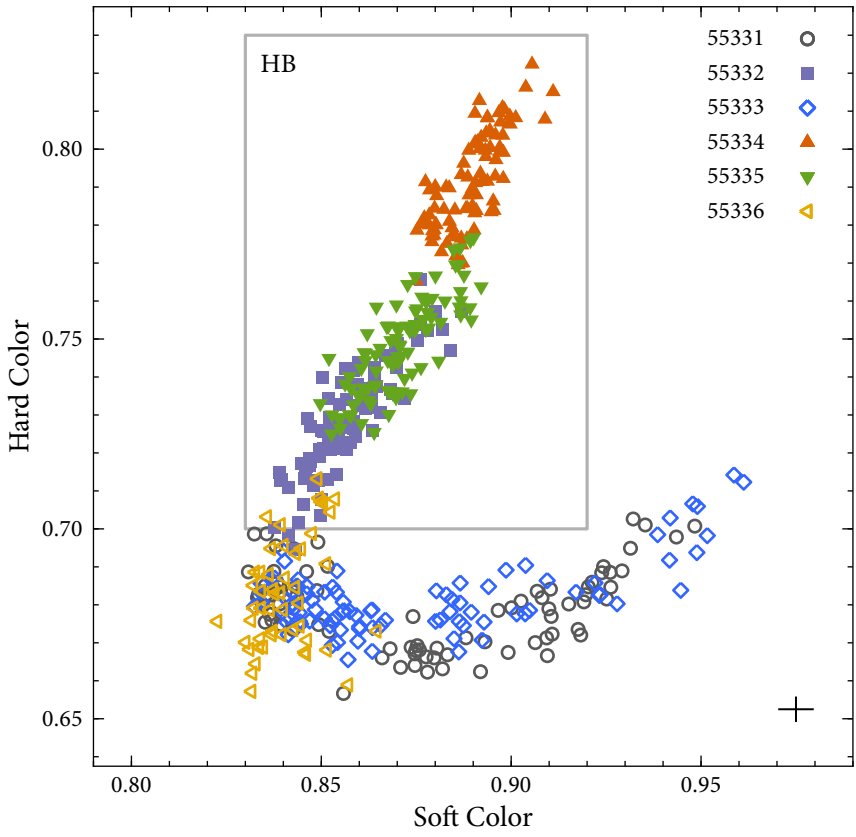

Figure 6.1: X-ray color-color diagram of Sco X-1 from the *RXTE*/PCA data obtained during the simultaneous MAGIC campaign. See the text for a definition of the Hard and Soft colors. The typical relative error of each measurement is around 0.5% and is shown by a black cross at the bottom-right corner. The HB selection range is indicated by the gray box. The different symbols and colors indicate each of the different observation days, labeled in MJD. The filled symbols indicate days selected as HB and empty symbols days selected as NB or FB.

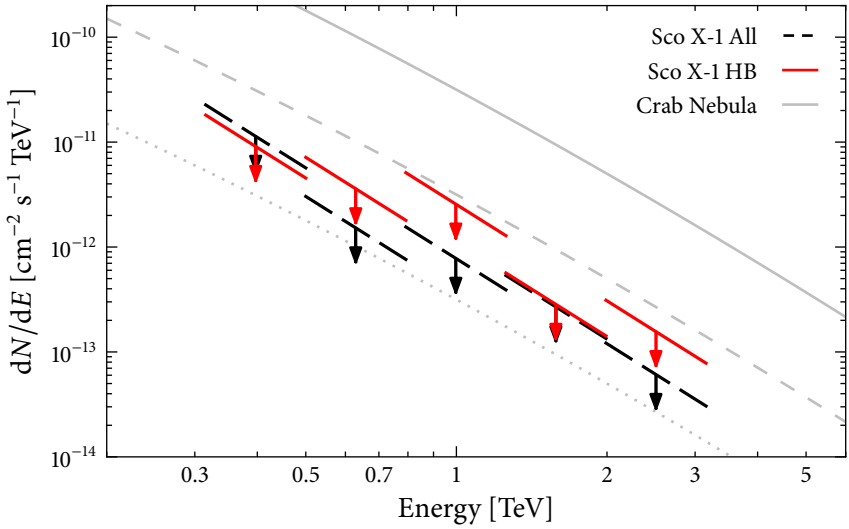

Figure 6.2: Differential upper limits for all the observations (black, dashed) and for the days in the HB (red). The slope of the bar indicates the assumed power-law photon index in the calculation of the upper limit. The Crab Nebula spectrum (Albert et al., 2008) is shown for comparison, as well as its 10% (dashed) and 1% (dotted) fractions.

per limits between 2.0×10^{-12} cm^{-2} s^{-1} and 7.9×10^{-12} cm^{-2} s^{-1}, as shown in Table 6.1.

In Figure 6.2 we show the differential flux upper limits computed for the HB state and the whole dataset to serve as a constraint for future theoretical modeling of the VHE emission of the source.

6.4 Discussion

To put in context the MAGIC results and understand the potentialities of Sco X-1 to produce VHE emission, we will discuss some of the possible emission scenarios. We will consider the energy budget available from the relativistic jet and the processes that could give rise to VHE emission either at its base or further away from the compact object. Finally, we compare Sco X-1 with other microquasars and the detected gamma-ray binaries and conclude with a brief summary.

The dominant radiation fields play an important role in the emission of VHE photons through IC processes, and also in the gamma-ray absorption through pair creation. In Sco X-1 these are the ~1 keV X rays from the ac-

cretion disc, the non-thermal hard X rays, and possibly the X-ray enhanced stellar radiation (Bednarek & Pabich, 2010). The magnetic field also needs to be considered, since it determines the relevance of SSC versus external IC channels (with seed photons from disc/corona and stellar radiation fields) as well as the importance of synchrotron cooling. LMXBs are not expected to have dense enough matter fields for efficient proton-proton collisions (see, e.g., Vila & Romero 2010) or relativistic Bremsstrahlung. Other processes like photomeson production are not expected to be relevant (see, however, Levinson & Waxman 2001). A general analysis of the importance of hadronic and leptonic processes of VHE emission in microquasars can be found in Bosch-Ramon & Khangulyan (2009).

The emitter properties will be mostly constrained by the jet power, which dictates the maximum energy budget available, and the emitter size and location. The jet luminosity ($L_{\rm j}$) can be fixed assuming that the power-law hard X rays come from the jet, and assuming an X-ray luminosity to total jet power ratio of 0.01–0.1. Given that the non-thermal power-law luminosity is $L_{\rm ntX} \sim 10^{35} - 10^{36}$ erg s^{-1}, a value of $L_{\rm j} \sim 10^{37}$ erg s^{-1} seems reasonable, and is also high enough to account for the radio emission from the source (Fomalont et al., 2001). The VHE luminosity upper limits in the HB show that Sco X-1 has a maximum VHE luminosity to jet power ratio of $L_{\rm VHE}/L_{\rm j} \lesssim 10^{-3}$. This value is slightly below the ratio inferred for the Cygnus X-1 flare (Albert et al., 2007), and similar to the upper limit of Cygnus X-3 (Aleksić et al., 2010). For the whole dataset, the upper limit to this ratio is more strict, going down to $L_{\rm VHE}/L_{\rm j} \lesssim 10^{-4}$, close to the maximum values inferred for GRS 1915+105 (Acero et al., 2009). However, given the transient nature of these sources, the orbital coverage and total length of the observational campaign play a role in their eventual detection. We note that the campaign presented here is relatively short and does not provide a complete orbital coverage so it does not rule out the possibility of VHE flares from Sco X-1.

Assuming that the jet of Sco X-1 can indeed accelerate particles efficiently, there are several possible reasons to explain the MAGIC non-detection. We will begin by considering the possibility that particles are accelerated in the jet base and the power-law hard X rays are emitted there. At this location, it may be difficult to accelerate particles beyond 100 GeV because of strong radiative cooling. The emitted spectrum is likely to be very soft because of the dominant synchrotron cooling and IC occurring deep in the Klein-Nishina regime (see Sec. 2.3.1). In addition, the radiation from 10 GeV to 1 TeV would likely be absorbed through pair creation by the intense radiation field from the accretion disc. At this location, even lower energy GeV photons would be absorbed. However, if the magnetic field is low enough and electromag-

netic cascading (e.g., Aharonian & Vardanian, 1985) is efficient, absorption at the jet base owing to the disc photon field might not be so relevant. Another source of absorption is the stellar photon field, enhanced through accretion X-ray-irradiance of the stellar surface, and could be optically thick for VHE gamma rays in some orbital phases. Note however that MAGIC has not detected the source even for those phases in which this source of gamma-ray absorption should be negligible (Bednarek & Pabich, 2010): on MJD 55334 the source was in the HB and the orbital phase range of the observation was ϕ=0.03–0.12, for which the expected gamma-ray opacity is $\tau \sim 0.1$. The combined effect of a steep gamma-ray spectrum and pair creation absorption would diminish the chances of a VHE detection, particularly for an observation at high zenith angles and correspondingly high energy threshold as presented here.

On the other hand, radiation at VHE produced further apart from the compact object, at distances above 10^8 cm, could be eventually detected. The SSC channel, efficient for intermediate values of the magnetic field, would yield a less steep spectrum and may occur in regions where the emitter and the environment are optically thin to VHE photons. IC with the X-ray enhanced stellar photon field could also yield significant and less steep VHE radiation and would be most efficient for optical depths of order of unity. According to the calculations of Bednarek & Pabich (2010), this would take place around orbital phases close to 0.3 and 0.7, but we did not detect such emission on MJD 55335 at orbital phases 0.25–0.39. At these high altitudes in the jet, GeV photons could easily escape the system and produce detectable high-energy gamma-ray emission. The eventual detection of Sco X-1 by *Fermi* or *AGILE*, plus a non-detection with low-enough upper limits at VHE, would likely favor the scenario where gamma-ray radiation is emitted from a location far away from the neutron star but the spectrum is too steep for a VHE detection. Synchrotron cooling dominance could explain the steep spectrum and would mean that the power-law hard X rays have a synchrotron origin.

For leptonic emission scenarios, such as SSC and external IC described above, it can be assumed that X-ray emission has a synchrotron origin and VHE gamma-rays have an IC origin. The VHE to non-thermal X-ray luminosity ratio is then a sensitive indicator of the importance of synchrotron cooling and ultimately of the magnetic field of the emitter. For the case of Sco X-1, and considering only the hard X-ray power-law as non-thermal X-ray emission, this ratio has a maximum value of $L_{\rm VHE}/L_{\rm ntX} \lesssim 0.02$ for the HB. On the hitherto detected gamma-ray loud X-ray binaries this ratio is much higher. For the case of LS I +61 303, for example, the VHE to X-ray ratio is between 0.5 and 1 during the X-ray and VHE peak at phases ϕ=0.6–0.7 (see

Chapter 3 and, in particular, Tables 3.1 and 3.2). Even considering the average fluxes for the full simultaneous campaign during 60% of an orbit the ratio is 0.26. In both cases, the VHE to X-ray luminosity ratio is higher than the value we obtained for Sco X-1 by more than an order of magnitude. However, as mentioned above for the comparison with other microquasars, the short total length of the observational campaign presented here prevents us from making absolute comparisons because of the possible transient nature of the source. On the other hand, if there is no such flaring behaviour, the difference in the VHE to X-ray luminosity ratios indicates that the underlying physics is significantly different than for LS I +61 303 or LS 5039.

In conclusion, our results place the first upper limits on the VHE gamma-ray emission from Sco X-1 in all of the accretion states of the source. If Sco X-1 is indeed capable of producing TeV emission, either a longer observational campaign, with better orbital coverage (to probe effects that might depend on orbital phase such as absorption, cascading, etc.), or an instrument with a significant increase in sensitivity, such as the future CTA, might be required to detect it. Our upper limits also indicate that the underlying VHE emission physics may be inherently different in the case of Sco X-1 and the detected gamma-ray binaries.

References

Abdo, A. A., et al. 2009, Science, 326, 1512

Acero, F., et al. 2009, A&A, 508, 1135

Aharonian, F. A., & Vardanian, V. V. 1985, Ap&SS, 115, 31

Albert, J., et al. 2007, ApJ, 665, L51

—. 2008, ApJ, 674, 1037

Aleksić, J., et al. 2010, ApJ, 721, 843

Atoyan, A. M., & Aharonian, F. A. 1999, MNRAS, 302, 253

Bednarek, W., & Giovannelli, F. 2007, A&A, 464, 437

Bednarek, W., & Pabich, J. 2010, A&A, 514, A61+

Bosch-Ramon, V., & Khangulyan, D. 2009, International Journal of Modern Physics D, 18, 347

Bosch-Ramon, V., Romero, G. E., & Paredes, J. M. 2006, A&A, 447, 263

Brazier, K. T. S., et al. 1990, A&A, 232, 383

D'Aí, A., Życki, P., Di Salvo, T., Iaria, R., Lavagetto, G., & Robba, N. R. 2007, ApJ, 667, 411

Di Salvo, T., et al. 2006, ApJ, 649, L91

Fomalont, E. B., Geldzahler, B. J., & Bradshaw, C. F. 2001, ApJ, 558, 283

Fomin, V. P., Stepanian, A. A., Lamb, R. C., Lewis, D. A., Punch, M., & Weekes, T. C. 1994, Astroparticle Physics, 2, 137

Hasinger, G., & van der Klis, M. 1989, A&A, 225, 79

Hjellming, R. M., et al. 1990, ApJ, 365, 681

Levinson, A., & Waxman, E. 2001, Physical Review Letters, 87, 171101

Li, T., & Ma, Y. 1983, ApJ, 272, 317

Rolke, W. A., López, A. M., & Conrad, J. 2005, Nuclear Instruments and Methods in Physics Research A, 551, 493

Saito, T. Y., et al. 2009, in Proc. of the 31st ICRC (Łódź), arXiv:0907.1017

Steeghs, D., & Casares, J. 2002, ApJ, 568, 273

Tavani, M., et al. 2009, Nature, 462, 620

Tonwar, S. C., Gopalakrishnan, N. V., Gupta, S. K., Rajeev, M. R., Sreekantan, B. V., & Srivatsan, R. 1991, Physical Review Letters, 67, 2248

Vila, G. S., & Romero, G. E. 2010, MNRAS, 403, 1457

7

Concluding remarks and future work

7.1 Concluding remarks

In this thesis we have presented the current state of high-energy astrophysics, and in particular of our understanding of gamma-ray binaries. At all moments a multiwavelength approach has been taken to unveil the mysteries of gamma-ray binaries, with special attention to the intrinsic connection between X-ray and VHE emission in non-thermal sources.

After an introduction to the field and to high-energy processes in gamma-ray binaries, we have presented the discovery of correlated X-ray and VHE emission from LS I +61 303 in Chapter 3. Even though this is an important result, the relatively low sensitivity of the VHE gamma-ray observations precluded us from gaining further insight into the correlation at scales shorter that a few hours. For this reason, we also explore how the future VHE instrumentation may improve these campaigns through a simulation of CTA observations in Appendix C. We have presented an expansion on the physical interpretation of the X-ray/VHE correlation in Chapter 4 through the development of a leptonic one zone radiation model. Assuming dominant adiabatic losses, which could be natural in a binary system environment, we have demonstrated that the X-ray/VHE correlated emission can be originated in a single population of relativistic electrons. We consider the likelihood of the PWS and accreting scenarios to give rise to the shown properties and in

addition conclude that a different particle population must be responsible for the emission at GeV energies.

It is important to identify all the possible channels of information that can give us additional clues about the nature of gamma-ray binaries. In Chapter 5 we have considered the previously unexplored thermal X-ray emission from the shocked stellar wind in gamma-ray binaries as an indicator of the shape of the interaction region and therefore of the pulsar spin-down luminosity. We have applied the resulting model to LS 5039, the only gamma-ray binary with a relatively well understood stellar wind. From the lack of thermal features in X-ray spectra taken at apastron and periastron we have derived strict upper limits to the spin-down luminosity of the pulsar. These upper limits are very close to the lower limit imposed by the energetic output in the MeV–GeV range. Therefore, we find that if the PWS scenario is indeed a reality in LS 5039, the efficiency of the energy conversion from pulsar spin-down luminosity to accelerated relativistic particles must be extremely high. The reduced range of allowed spin-down luminosities will prove extremely useful in future testing of the PWS scenario.

We have also conducted a search for VHE gamma-ray emission from other, yet undetected, binary systems. In Chapter 6 we have presented the results of a simultaneous X-ray/VHE observation campaign with *RXTE* and MAGIC on Sco X-1. This campaign has allowed us to select the VHE data based on the accretion states of the source as seen through its X-ray colors. However, we did not detect a significant VHE signal for any of the selected states. This upper limits allowed us to place constrains on the ability of Sco X-1 to produce VHE gamma-ray emission, and will prove valuable for future modeling of the non-thermal emission of the source.

In spite of the efforts of the community to understand gamma-ray binaries, they have proved to be difficult to understand completely due to the many components of the systems relevant to the non-thermal emission. However, it is clear that a multiwavelength approach as the one presented in this thesis is fundamental to gain more knowledge about these systems. Below we present a few of the items that would be a natural continuation of the work presented here and that could shed more light on the nature of gamma-ray binaries.

7.2 Future work

Study of the implications of the limit on thermal X-ray emission

The computation of the thermal X-ray luminosity of the shocked stellar wind presented in Chapter 5 is based on a series of assumptions on the cooling

regime of the post-shock gas. This emission could be calculated self-consistently through hydrodynamical simulations of the stellar wind. In addition, hydrodynamical instabilities not taken into account may play an important role and would be naturally considered by the simulation. These hydrodynamical simulations could reproduce the work presented in Chapter 5 and provide it with a higher degree of confidence owing to the self-consistency of the method. The output of such modelling will also prove useful in determining the structure and orientation of the non-thermal emitter for the given pulsar spin-down luminosities, so we will be able to refine the energetics considerations made in Section 5.4. The natural following step would be the calculation of a non-thermal broadband radiation model of the binary pulsar scenario using the constrained pulsar spin-down luminosity values and evaluate the fitness of this scenario to explain the radiation from LS 5039.

The long term gamma-ray variability of LS I +61 303

It has been long known that LS I +61 303 has a four year super-orbital modulation of the amplitude of the outburst peak in radio (Paredes, 1987; Gregory, 2002, see also Section 3.1). However, it has never been detected at other bands. Recently the source has been displaying apparently erratic behaviour in the HE and VHE gamma-ray bands. After March 2009, the periodic modulation of the source in HE gamma-rays as seen by *Fermi* decreased notably along with an increase of the overall flux (Dubois, 2010). In the VHE gamma-ray band there have been no reports of detection around apastron since 2008, while a detection around periastron was recently made by VERITAS (Ong et al., 2010; Holder, 2010). It was previously thought that the intense stellar photon field at periastron would absorb any VHE emission through pair production absorption, but in Chapter 4 we have shown that the geometrical dependence of the pair production cross section, along with the binary orbit characteristics, required the intrinsic emission to be very low to account for the previous non-detections. It must be noted that such long-term variability is not present in the apparently similar gamma-ray binary LS 5039 (see Aharonian et al. 2006 for VHE and Zabalza et al. 2008; Takahashi et al. 2009 for X-ray emission)

It is not clear for the scientific community which are the many timescales of variability that may affect the non-thermal processes in this system. This situation could be improved through a combination of X-ray observations and modeling techniques. A re-analysis of past X-ray observations of the source performed with *XMM-Newton*, *Chandra*, *Swift* and *RXTE*, as well as requesting new observations during the following Announcements of Op-

portunity, will allow to search for any long-term variability or characteristics in the non-thermal emission in the X-ray band, which is intimately related to non-thermal emission at VHE. In parallel to this observational review of the source, it would be interesting to perform a theoretical analysis of the possible mechanisms that may affect non-thermal processes along such long time scales. An initial candidate is the presence of density waves in the decretion disc of the star, which may interact hydrodynamically with the emitting region or even be a source of increased absorption in certain phases, thus leading to diminished emission around periastron in VHE.

The Hard X-ray emission of gamma-ray loud X-ray binaries

In the following years the astrophysical community will see an increase in the quality of the hard X-ray observatories. The launch of the first mirror imaging hard X-ray telescope, NuSTAR, will provide us with new insights into the non-thermal emission of gamma-ray binaries, and will be followed by the even more sensitive ASTRO-H. While accretion powered X-ray binaries typically show a cutoff in the spectrum below 100 keV, such a feature has not been observed in LS I +61 303 and LS 5039, prompting their dismissal as accretion-powered sources. Deeper observations in the hard X-ray band may point towards spectral features that, while not necessarily exponential cutoffs, will give us information on the highest energy particles through their synchrotron emission. These very high energy particles cool rapidly through both synchrotron and Inverse Compton, so their emission is bound to come from a location close to the acceleration region. A detailed study of the hard X-ray spectra from the *Suzaku* hard X-ray detector (HXD) and the forthcoming NuSTAR and ASTRO-H along with spectral modeling in the context of a broadband radiation model will allow to probe closer to the particle acceleration site.

Study of new gamma-ray binaries

The current generation of VHE gamma-ray telescopes (HESS, MAGIC, VERITAS) has provided us with a wealth of new discoveries during the past few years. Both HESS and MAGIC have been planning an upgrade of their systems that will provide them with an increase in the energy range covered and sensitivity. In the case of MAGIC, a second identical 17 m telescope is already working to provide stereo images of the electromagnetic showers and aid in background rejection. This has provided a significant increase of sensitivity

and the first papers with results from this system are being currently published (e.g., the search for VHE emission from Sco X-1 presented in Chapter 6). HESS, on the other hand, has chosen to complement its four midsized telescopes (~13 m) with a fifth very large one (~25 m) to have enough collecting area to detect the smaller showers corresponding to lower energy photons and thus be sensitive in the 50–200 GeV range. For the case of HESS, the improvement will allow to extend the galactic plane survey to lower energies and hopefully detect new candidates for gamma-ray binaries. Some X-ray binaries are expected to have a softer spectrum in the VHE band due to strong cooling and pair production absorption, and thus a lower energy threshold will be very useful for their detection and study.

In the HE gamma-ray domain a few other binaries have been recently detected. These cannot be strictly classified as gamma-ray binaries given that their emission in other bands is orders of magnitude above that in the HE and VHE gamma-ray bands, whereas in known gamma-ray binaries the dominant band in energy output is from MeV to TeV. Cyg X-3, and accreting microquasar, has been detected repeatedly during flares in the HE gamma-ray domain (Abdo et al., 2009; Tavani et al., 2009b) and we have made efforts to observe it with MAGIC, but have yet been unsuccessful in its detection at VHE (Aleksić et al., 2010, see, however, the alert system implemented in Appendix B). In addition, the massive star binary Eta Carinae has been possibly detected in the GeV range by both *Fermi*/LAT (Abdo et al., 2010) and *AGILE*/GRID (Tavani et al., 2009a). This indicates that colliding wind binaries may accelerate particles up to very high energies. The continuous survey mode of *Fermi*/LAT will probably discover a handful of these kind of sources during the following few years. We must be prepared to study these new sources from a multiwavelength observational and theoretical point of view.

References

Abdo, A. A., et al. 2009, Science, 326, 1512

—. 2010, ApJ, 723, 649

Aharonian, F., et al. 2006, A&A, 460, 743

Aleksić, J., et al. 2010, ApJ, 721, 843

Dubois, R. 2010, in Proceedings of the VERITAS Workshop on High Energy Galactic Physics, Barnard College, Columbia University, New York, ed. E. Aliu, J. Holder & R. Mukherjee, eConf C1005281, 9

Gregory, P. C. 2002, ApJ, 575, 427

Holder, J. 2010, in Proceedings of the VERITAS Workshop on High Energy Galactic Physics, Barnard College, Columbia University, New York, ed. E. Aliu, J. Holder & R. Mukherjee, eConf C1005281, 10

Ong, R. A., et al. 2010, The Astronomer's Telegram, 2948

Paredes, J. M. 1987, PhD thesis, University of Barcelona

Takahashi, T., et al. 2009, ApJ, 697, 592

Tavani, M., et al. 2009a, ApJ, 698, L142

—. 2009b, Nature, 462, 620

Zabalza, V., Paredes, J. M., & Bosch-Ramon, V. 2008, International Journal of Modern Physics D, 17, 1867

A

The MAGIC telescopes

The atmosphere of the earth is optically thick to practically all wavelengths of the electromagnetic spectrum except for optical and radio radiation. This precludes the observation of radiation of astrophysical origin in all the other bands using ground-base telescopes and requires the use of space-borne observatories. While this remains true for VHE gamma-rays, the observations of the secondary products of the extremely energetic gamma-rays as they interact with the particles in the atmosphere allows us to reconstruct the direction and energy of the original photon. Here we briefly explain this technique, known as atmospheric Cherenkov detection, and present its use in the operations of the Major Atmospheric Gamma-ray Imaging Cherenkov (MAGIC) telescopes.

A.1 Imaging Atmospheric Cherenkov Telescopes

When a VHE gamma-ray enters the atmosphere it will interact with the Coulomb field of the atmospheric nuclei and create an electron positron pair. The secondary particles will produce a new generation of energetic gamma-rays through bremsstrahlung emission. This process will go on while the subsequent generations of photons and pairs travel downwards through the atmosphere, in a process known as Extensive Air Shower (EAS). Eventually, the energy of the electrons and positrons drop to the point that the ionisation

losses are dominant over bremsstrahlung, so the generation of new particles begins to fall off as fewer pairs are capable to produce secondaries. The energetic electrons that travel towards the ground give rise to a compact patch of Cherenkov light at the ground level of between 100 and 150 m in diameter. In general, the total particle number of the shower is related to the energy of the parent gamma-ray, and thus the luminosity of Cherenkov light can be related to the original VHE photon.

By recording the images of the Cherenkov light distribution from ground based telescopes it is possible to recover both the longitudinal and lateral development of the electromagnetic shower. However, this method of detection carries a significant background in the form of air showers initiated by hadronic cosmic rays. When a cosmic ray proton or nucleus interacts with the atmosphere it produces nuclear fragments and pions with large transverse momentum. The addition of transverse momentum to the shower has the consequence that its development is notably wider than for purely electromagnetic showers, as can be seen in Figure A.1. Imaging Atmospheric Cherenkov Telescopes are able to exploit this development difference to discriminate between hadronic and electromagnetic showers from the imaged shapes and time development.

Images of EAS initiated by gamma-rays have a compact elliptic shape, with the major axis of the ellipse indicating the shower axis projected onto the detector. Since the instrument will receive the Cherenkov radiation from all showers within its field of view, its effective area is not that of its light collector but that of the imaged atmosphere. The energy range for gamma-ray detection is limited at the lower end by the reduced number of Cherenkov light emitting particles of the lower-energy EAS. Their correspondingly lower Cherenkov luminosity precludes a confident energy and direction reconstruction. Therefore, larger light collecting mirrors help in reducing the energy threshold of the observation. At the higher end, the limiting factors are the low number of photons and the large size of the showers on the camera (sometimes still developing at the position of the telescope).

All current instruments use multiple telescopes to image the shower from different angles for improved reconstruction of the gamma-ray direction and energy, as well as an improvement on background rejection through a coincidence requirement and better shower shape characterisation. The telescopes should be spaced apart enough to provide sufficient baseline for stereoscopic measurements but small enough so that they fit within the Cherenkov light pool of the shower. Therefore, they are typically set between 70 m to 150 m apart. The current generation of IACTs, embodied in HESS, MAGIC and VERITAS, provide angular resolutions of around 0.1° and down to an ar-

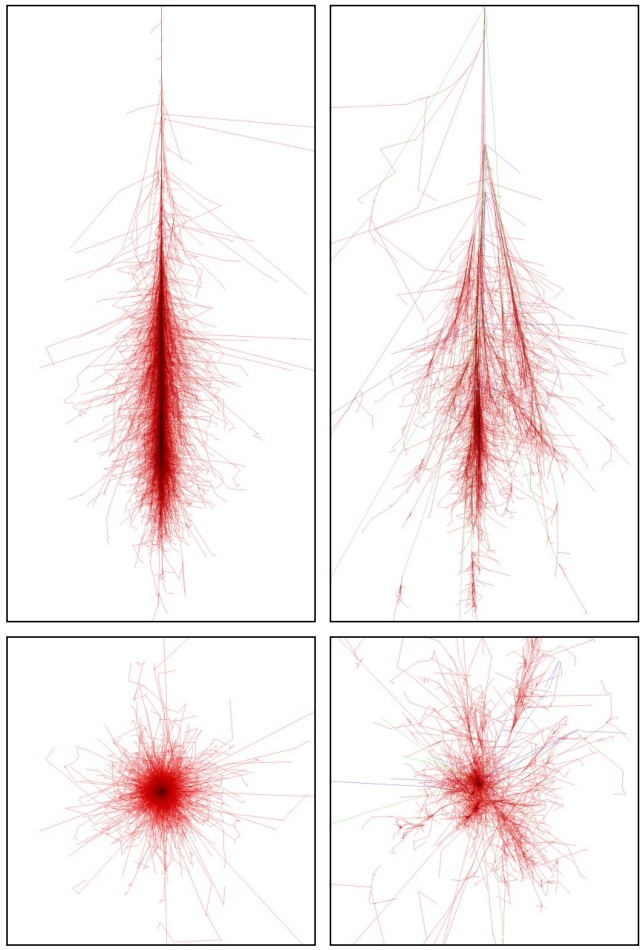

Figure A.1: Longitudinal (top) and lateral (bottom) development of an electromagnetic (left) and hadronic (right) showers with an initial energy of 100 GeV simulated with CORSIKA. The longitudinal projection plot has a height of 20 km and a width of 10 km, while the lateral projection plot is 10 km on the side. Images from Schmidt (2005).

Figure A.2: The MAGIC telescopes

cminute for bright sources around 1 TeV and a cosmic ray rejection factor of the order of 10^{-4}. A detailed discussion of EAS and the IACT detection technique can be found, for example, in Aharonian et al. (2008).

A.2 The MAGIC Telescopes

MAGIC consists of two 17 m diameter IACTs located at the Roque de los Muchachos Observatory, in the Canary Island of La Palma (28° N, 18° W, 2200 m above sea level). It began scientific operations in 2004 as the largest single dish IACT, allowing for the lowest energy threshold among the current generation of IACT. The energy threshold for the nominal trigger was of 55 GeV and provided a sensitivity of 1.6% of the Crab Nebula flux for a 5σ detection in 50 hr of on-source time. In order to improve the background rejection and energy reconstruction, it became a stereoscopic system in autumn 2009 with the addition of a second telescope with the same dimensions as the first but with an improved camera and readout electronics. Since then, the instrument sensitivity almost doubled with respect to the one of the stand-alone telescope operation mode, reaching at low zenith angles 0.8% of the Crab Nebula flux for a detection at 5σ significance level in 50 hours above 250 GeV (Colin et al., 2009).

A.3 MAGIC data analysis with MARS

Below we do a brief outline of the data analysis procedure with the current MAGIC standard analysis software known as MARS. For each telescope individually, a signal calibration is done based on the calibration and pedestal runs taken interleaved with the data. Then an image cleaning is performed to assure that only those pixels with a significant signal are passed onto the shower reconstruction algorithm. After the image cleaning a shower image reconstruction is performed and the Hillas parameters are computed (Aliu et al., 2009). The stereo events which survive in both detectors are then selected. The image parameters of the corresponding single-telescopes are combined for the estimation of the stereo parameters. The event direction is reconstructed as the intersection of the corresponding single-telescope directions determined through a DISP algorithm (Aleksić et al., 2010). These stereo variables, together with single-telescope image parameters, are the input of a Random Forest (RF) algorithm (Albert et al., 2008) that provides the background rejection based on Monte Carlo samples of gamma-rays and a so-called OFF observation with no gamma-ray signal. The result of the RF algorithm is a parameter given to each event, known as *hadronness*, that may be interpreted as the likelihood that it is a hadronic initiated shower event and thus should be rejected as background. For each of the observations, a cut optimization is performed, as a function of energy, on a Crab Nebula sample recorded under similar conditions. The signal selection is performed based on the distribution of the squared angular distance (θ^2) between the reconstructed shower pointing direction and the catalogue source position. The energy of each event is estimated by using look-up tables created from Monte Carlo simulated gamma-ray events.

Since observations are usually performed in the so-called wobble mode (Fomin et al., 1994), in which the telescope points in two directions at 0.4° opposite sides of the source, up to three background measurements can be obtained from the same observation. From the selected source and background cuts, integrated fluxes from the source may be derived by computing the effective area from the Monte Carlo simulated gamma-ray events. Lightcurves and spectra may be generated through selections on event time and energy, respectively. The relatively low energy resolution of ~20% may result in spillover of events for power-law spectra and artificially softer measured photon indices. To avoid this, the application of spectral unfolding methods is necessary (Albert et al., 2007).

A.3.1 Upper limit calculation

For the case of non-detections, flux upper limits are computed. To do so, we used the method of Rolke et al. (2005), including a 30% systematic uncertainty, to obtain the upper limit of the number of events consistent with the measured excess events. Once the event upper limit $N_{\rm ul}$ is known, the derivation of the integral flux upper limit is quite straightforward. In general, the number of events obtained by a detector will be

$$N = T_{\rm eff} \int_0^\infty \Phi(E) A_{\rm eff}(E) {\rm d}E, \tag{A.1}$$

where $T_{\rm eff}$ is the effective integration time, $\Phi(E) = {\rm d}N/({\rm d}A{\rm d}E{\rm d}t)$ is the source differential flux in units of photons per unit area, energy, and time, and $A_{\rm eff}(E)$ is the effective detection area. For a given assumed source spectrum $\Phi(E) = K \times S(E)$, the normalization K may be found from the event upper limit $N_{\rm ul}$ by inverting Eq. (A.1)

$$K \leq \frac{N_{\rm ul}}{T_{\rm eff} \int_{E_0}^\infty S(E) A_{\rm eff}(E) {\rm d}E}.$$

Here the integral will not be from null energy but from the low energy threshold of the analysis E_0.

The previous flux upper-limit calculation relies on the assumed shape of the particle spectrum. For a previously undetected source the spectral shape may be unknown, and while educated guesses can be made in most cases (see, e.g., Sec. 6.2.1), it may be safer to evaluate the upper limits in restricted ranges in energy, obtaining the so-called differential flux upper limits. Even though a spectral shape assumption is still required, assuming a power-law with its pivot point inside the restricted energy range will incur in a variation of less that 1% in the value of the upper limit for a variation of 30% in the assumed photon index, so the computed values can be considered quite robust. The pivot point for the source spectrum $S(E) = (E/E_0)^{-\Gamma}$ can be computed as the mean expected photon energy in the energy range (E_1, E_2)

$$E_0 = \frac{\int_0^\infty E E^{-\Gamma} A_{\rm eff}(E, E_1, E_2) {\rm d}E}{\int_0^\infty E^{-\Gamma} A_{\rm eff}(E, E_1, E_2) {\rm d}E},$$

where $A_{\rm eff}(E, E_1, E_2)$ is the effective area computed for Monte Carlo events with true energies between E_1 and E_2. The normalization factor K can then be obtained as above

$$K \leq \frac{N_{\rm ul}}{T_{\rm eff} \int_{E_0}^\infty (\frac{E}{E_0})^{-\Gamma} A_{\rm eff}(E) {\rm d}E} = \frac{N_{\rm ul} E_0^{-\Gamma}}{T_{\rm eff} \int_{E_0}^\infty E^{-\Gamma} A_{\rm eff}(E) {\rm d}E}.$$

The resulting energy fluxes for both the integral and differential upper limits can be computed from the assumed source spectrum by integrating it over energy in the selected range, i.e., E_0 to infinity for integral upper limits and E_1 to E_2 for differential upper limits. An example of the results obtained through this method for the case of Sco X-1 are presented in Section 6.3.

References

Aharonian, F., Buckley, J., Kifune, T., & Sinnis, G. 2008, Reports on Progress in Physics, 71, 096901

Albert, J., et al. 2007, Nuclear Instruments and Methods in Physics Research A, 583, 494

—. 2008, Nuclear Instruments and Methods in Physics Research A, 588, 424

Aleksić, J., et al. 2010, A&A, 524, A77+

Aliu, E., et al. 2009, Astroparticle Physics, 30, 293

Colin, P., et al. 2009, in Proc. of the 31st ICRC (Łódź), arXiv:0907.0960

Fomin, V. P., Stepanian, A. A., Lamb, R. C., Lewis, D. A., Punch, M., & Weekes, T. C. 1994, Astroparticle Physics, 2, 137

Rolke, W. A., López, A. M., & Conrad, J. 2005, Nuclear Instruments and Methods in Physics Research A, 551, 493

Schmidt, F. 2005, "CORSIKA Shower Images", `http://www.ast.leeds.ac.uk/~fs/showerimages.html`

B

GeV monitoring of galactic variable sources with Fermi/LAT

The *Fermi* observatory began operations on August 2008. Since then, it has been monitoring the whole sky every 3 hours in the energy band 0.3–30 GeV with the LAT instrument. Since the data is immediately public and available within a few hours of observation, it provides the ideal observatory to detect GeV flares from variable sources and trigger multiwavelength observation campaigns on short notice. Here we present an automatic analysis pipeline to detect flaring behaviour from a selection of sources.

B.1 Aperture analysis and alert thresholds

The best sensitivity from *Fermi*/LAT data can be obtained through the so-called maximum likelihood analysis, which takes into account the galactic diffuse emission and other sources in the field of the source of interest. This method, however, requires fine-tuning to obtain satisfactory results for galactic plane sources and, in addition, is computationally intensive.

There is a simpler, albeit less sensitive, method to obtain a lightcurve from sources with constant background. This method, known as aperture photometry, relies on the integration of the number of photons detected by the observatory in a circular region of radius 1° around the position of the source of

interest. The exposure for each bin of lightcurve is computed and a lightcurve in units of ph cm^{-2} s^{-1} is obtained. To reach the best sensitivity to flares, we select all photons in the energy band of the LAT instrument, i.e., 0.3–30 GeV. We note that this method does not provide a background-subtracted lightcurve. However, it can be assumed that, apart from the source of interest, the sources that contribute to the lightcurve background are constant over long timescales. This is the case for the galactic diffuse background and pulsed emission from galactic plane pulsars, the most common background sources in the galactic plane. Therefore, even if the lightcurve is not background-subtracted, we can detect flaring behavior from the source of interest as an increase in the flux from the extraction circle when compared to the long-term mean. As will be shown below, we found that for a difference between a given flux bin and the long-term mean of 2σ (where σ is the flux uncertainty of the bin), there is a high probability that the source is flaring.

We implemented an automatic analysis pipeline to perform the aperture analysis of a selection of galactic variable sources on a daily basis. The foundation of the pipeline is a Python script launched from the `cron` daemon. When launched, the script requests the latest LAT data from the LAT data server through a web form* and launches an analysis script on the downloaded data. It then puts together a long-term lightcurve from the recently analysed data and the archived flux points from the analysis of previous days, from which it computes the long-term mean. If the last analysed flux bin in either the 1 or 2 day binned lightcurves is at a flux higher than 2σ above the long-term mean, it sends an alert e-mail to a predefined group of people. The alert e-mail contains the information of the source, the flux of the most recent bin, and the lightcurve as an attachment. In case the source has soft or hard X-ray data available from the *RXTE*/ASM and *Swift*/BAT detectors, respectively, the script downloads the data and includes them in the plotted lightcurve (see Figures B.1, B.2 and B.3 for an example of the attached plots).

This method allows for a fast and automatic alert in order to prepare follow-up observations within the same day.

B.2 Monitored sources

B.2.1 Cygnus X-3

Cygnus X-3 is a microquasar that has been extensively observed with MAGIC (Aleksić et al., 2010), but no VHE emission has been detected yet. The extreme

* Accesible at `http://fermi.gsfc.nasa.gov/cgi-bin/ssc/LAT/LATDataQuery.cgi`

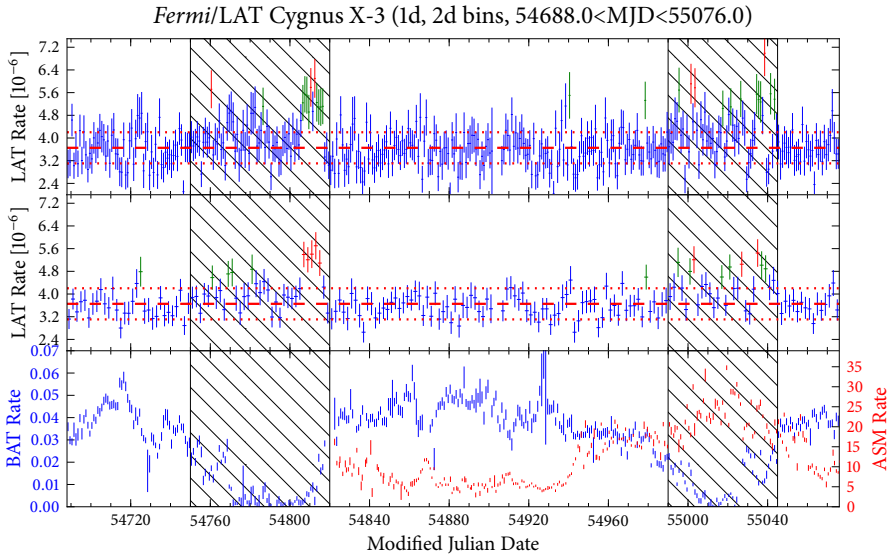

Figure B.1: HE gamma-ray lightcurve from Cygnus X-3 computed by the automatic analysis pipeline. The top and middle panels are the *Fermi*/LAT aperture photometry lightcurve of the source in 1 and 2 day bins, respectively. The horizontal red dashed line indicates the long term mean and the dotted line its 1σ dispersion. The flux bins shown in red are at least 3σ above the long term mean, whereas those shown in green are between 2σ and 3σ above the mean. In the bottom panel the *Swift*/BAT hard X-ray count rate is shown in blue and the *RXTE*/ASM soft X-ray count rate in red. The hatched time ranges correspond to the periods of activity reported by Abdo et al. (2009).

variability of the source and the diverse accretion states make it difficult to decide when to trigger VHE observations. Until recently, the best method was to rely on the information given by the X-ray state of the source through the monitoring of *RXTE*/ASM and *Swift*/BAT, but it was not clear how the X-ray state related to its putative gamma-ray flaring behavior. Recently, the source was detected by the gamma-ray observatories *AGILE* (Tavani et al., 2009) and *Fermi* (Abdo et al., 2009). The goal of having a better tool to trigger MAGIC observations through the HE gamma-ray state of Cygnus X-3 led us to develop the automatic analysis pipeline explained above. Comparing the output of the aperture photometry method with the maximum likelihood lightcurves shown in Abdo et al. (2009) we found that the 2σ threshold was a very good indicator of activity from the source. The result from the automatic analysis for the period during the flares reported by Abdo et al. (2009) can be seen in Figure B.1. Since 2009 Cygnus X-3 has undergone at least two other periods of activity, but we have been unable to trigger MAGIC observations because of either visibility constraints or bad weather at La Palma. However, we are confident that in the future the trigger alert will prove extremely useful.

B.2.2 Crab Nebula

The Crab Nebula is the only hard X-ray and gamma-ray source in the sky that is both bright and stable enough to be used as a standard candle. For decades it has been used as normalization standard by most X-ray and gamma-ray observatories. From 19 to 21 September 2010 the source unexpectedly doubled its flux in HE gamma-rays, as seen by *AGILE* (Tavani et al., 2010) and *Fermi*/LAT (Buehler et al., 2010). A subsequent analysis of the *Fermi*/LAT data indicated the flux increase consisted of several ~12 hr flux spikes (Balbo et al., 2011). Simultaneous observations at other wavelengths, including VHE gamma-rays, failed to see any significant variability from the source. In order to trigger MAGIC observations within the same day in case this flaring behavior repeats, we added the Crab Nebula to the list of monitored sources. Figure B.2 shows the flux increase during the September 2010 flare, and demonstrates that the automatic analysis pipeline will readily detect flares from the source even if they happen at lower fluxes.

B.2.3 PSR B1259−63

The gamma-ray binary PSR B1259−63 is known to be active in VHE gamma-rays only around the periastron passages. The long orbital period (4.3 years)

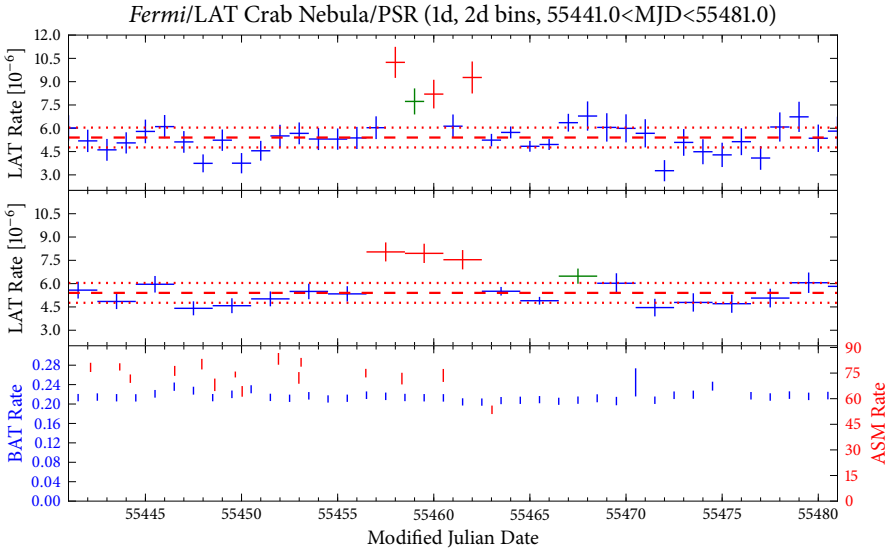

Figure B.2: HE gamma-ray lightcurve from the Crab Nebula computed by the automatic analysis pipeline. Note the lack of variability at X-rays during the gamma-ray flare. See Fig. B.1 for an explanation of the plots.

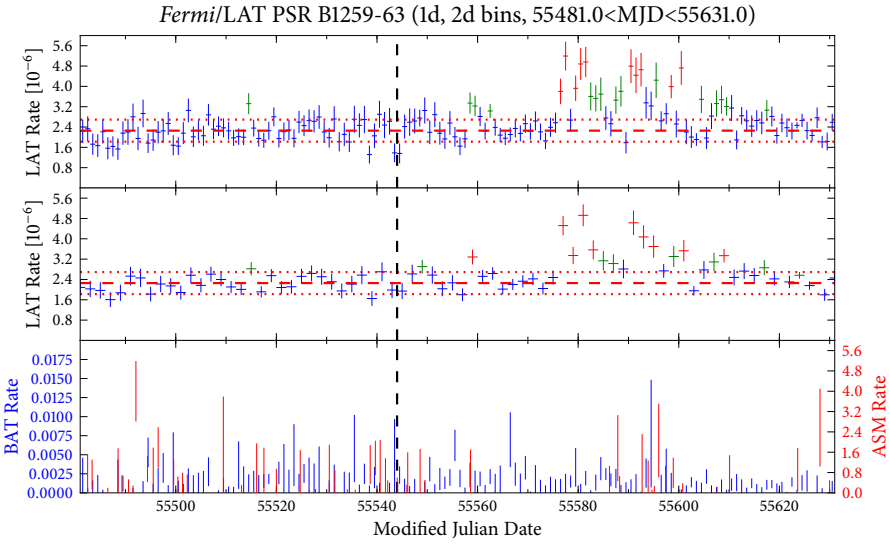

Figure B.3: HE gamma-ray lightcurve from PSR B1259−63 computed by the automatic analysis pipeline. Here the vertical dashed line indicates the periastron passage date. See Fig. B.1 for an explanation of the plots.

of the source had precluded any previous HE gamma-ray observations with *Fermi* until the periastron passage of December 2010. In contrast with the soft and hard X-ray lightcurve, which is symmetric with respect to periastron (Chernyakova et al., 2009), the HE gamma-ray flux before periastron is extremely low whereas it exhibits significant flares during a period 30 days after periastron. Even though PSR B1259−63 is not visible from the MAGIC site and thus the monitoring has no trigger value, in Figure B.3 we show the result of the automatic analysis pipeline. While aperture photometry is not sensitive enough to detect the source before periastron, the flare after the periastron passage is well detected and resolved when compared to the more sensitive maximum likelihood analyses (Tam et al., 2011; Abdo et al., 2011).

References

Abdo, A. A., et al. 2009, Science, 326, 1512

—. 2011, ApJL, submitted, arXiv:1103.4108

Aleksić, J., et al. 2010, ApJ, 721, 843

Balbo, M., Walter, R., Ferrigno, C., & Bordas, P. 2011, A&A, 527, L4+

Buehler, R., D'Ammando, F., Hays, E., et al. 2010, The Astronomer's Telegram, 2861

Chernyakova, M., Neronov, A., Aharonian, F., Uchiyama, Y., & Takahashi, T. 2009, MNRAS, 397, 2123

Tam, P. H. T., Huang, R. H. H., Takata, J., Hui, C. Y., Kong, A. K. H., & Cheng, K. S. 2011, ApJL, submitted, arXiv:1103.3129

Tavani, M., et al. 2009, Nature, 462, 620

—. 2010, The Astronomer's Telegram, 2855

C

Studying the short timescale variability of gamma-ray binaries with CTA

The next generation of Imaging Atmospheric Cherenkov Telescopes is embodied in the Cherenkov Telescope Array (CTA) (CTA Consortium, 2010). It is currently under planning and is being developed by an international collaboration of more than 700 scientists around the world, including, but not limited to, the MAGIC, HESS and VERITAS communities. CTA will consist of two arrays located in the North and South hemispheres in order to be able to observe the whole sky. Each of the arrays is planned to have of the order of a hundred telescopes of varying sizes. The largest telescopes (diameter ~ 23 m) will be sensitive to the low-energy range of VHE, i.e., 30 GeV $\lesssim E \lesssim$ 150 GeV. Two sizes of smaller and more sparsely located telescopes will provide sensitivity up to a 100 TeV. Not only will CTA provide an increased energy range of VHE observations, but the sensitivity is increased by nearly an order of magnitude with respect to the current generation of IACTs. However, the exact number of telescopes and their layout is currently under study. Monte Carlo simulations of the sensitivity of the array for several possible configurations have been computed within the Monte Carlo working group (WP-MC). At the current phase of the design study, it is important to test these configurations from an astrophysical point of view and select the ones that guarantee a higher scientific output from the observatory.

C.1 Fast flux variability

As part of the design study effort, we have studied the capabilities of CTA to detect fast flux and spectral variability from gamma-ray binaries. The perfect candidate for such studies is LS I +61 303. In Chapter 3 we have shown the discovery of correlated X-ray/VHE emission from this source with MAGIC and *XMM-Newton*. Additionally, fast X-ray variability on timescales of a thousand seconds has been detected (Sidoli et al., 2006; Rea et al., 2010), so it is natural to think that such fast variability may be present in VHE emission.

We analysed the data from a ~100 ks long *Chandra* X-ray observation of LS I +61 303 and extracted lightcurves with bins ranging from 100 s to 1000 s. We analysed the integrated spectrum and derived an average flux, from which we obtained the conversion factor from count rate to flux. We note this factor may depend on spectral shape variations, which were not taken into account. We applied this conversion factor to the count rate lightcurve to obtain an X-ray flux lightcurve. We then used the correlation between X-ray and VHE fluxes to derive the predicted VHE flux for each of the lightcurve bins

$$\left[\frac{\mathrm{F_X}}{10^{-12}\,\mathrm{erg\,cm^{-2}\,s^{-1}}}\right] = \left(12.2^{+0.9}_{-1.0}\right) + \left(0.71^{+0.17}_{-0.14}\right) \times \left[\frac{\mathrm{F_{TeV}}}{10^{-12}\,\mathrm{cm^{-2}\,s^{-1}}}\right].$$

We note, however, that the X-ray pedestal flux obtained in Chapter 3 is of 12.2×10^{-12} erg cm^{-2} s^{-1}, but the lightcurve from the *Chandra* observations presents fluxes as low as 7.8×10^{-12} erg cm^{-2} s^{-1}. For this reason, we have taken the latter value as the pedestal for obtaining the predicted VHE fluxes, resulting in the final expression $F_{\mathrm{TeV}} = 1.41 \times F_{\mathrm{X}} - 10.98$ (units as above). This is not based on any physical consideration but rather on the goal to have the best possible dataset to test the capabilities of CTA. The resulting VHE predicted lightcurves were then used as input for the CTA simulation routines which use the sensitivity curves for a variety of telescope configurations.

We considered two feasible observation scenarios. In the first, the full CTA I array is used to perform a deep, short observation of LS I +61 303. In this case, the observation length would be of the order of 4 h, which is the typical time span for which a source is visible under optimum conditions for a single night. To simulate this scenario, we selected 10 ks of the X-ray observation and obtained the simulated VHE fluxes. The resulting lightcurves are shown in Figure C.1, and it can be seen that CTA is able to clearly detect the fast variability exhibited by the X-ray lightcurve at scales down to 500 s. The detection of such variability would have strong implications on the location and size of the non-thermal emitter, as well as on the source of the apparently erratic variability of LS I +61 303. Even with the relatively short in-

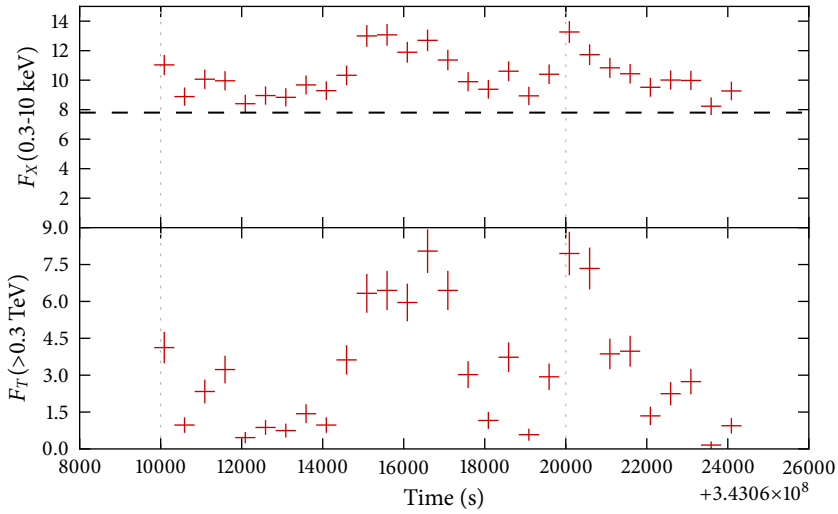

Figure C.1: Measured X-ray flux (top) and simulated VHE fluxes obtained with the full CTA array in configuration I (bottom) for the case of a one-night observation and a binning time of 500 s.

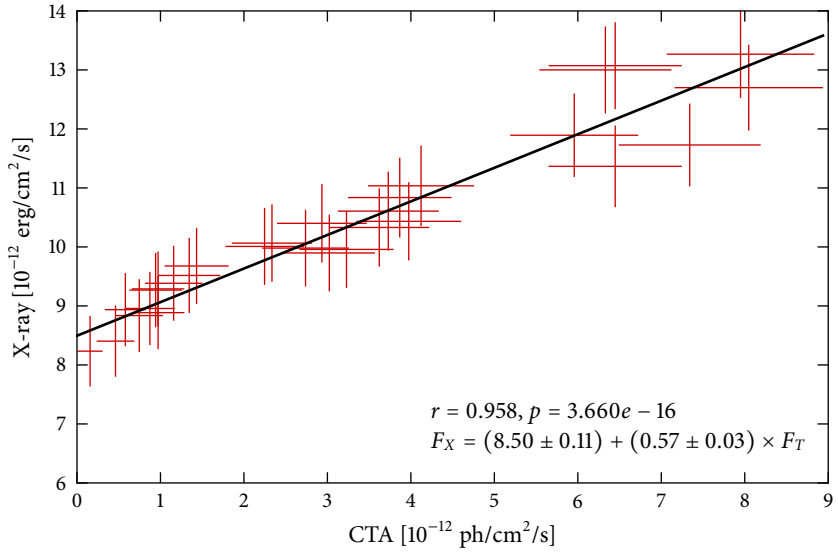

Figure C.2: X-ray/VHE correlation plot from the one-night, full array observation plotted in 500 s bins. The Pearson correlation factor, the chance probability of correlation and the parameters of the fitted correlation are shown as insets.

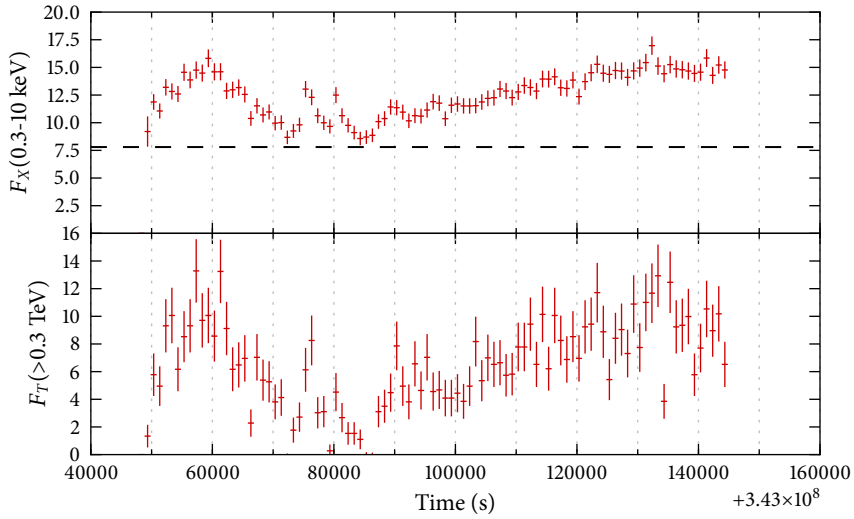

Figure C.3: Measured X-ray flux (top) and simulated VHE fluxes obtained with the subarray s9-2-120 (bottom) for the case of a campaign of ten nights of observation and binning time of 1000 s.

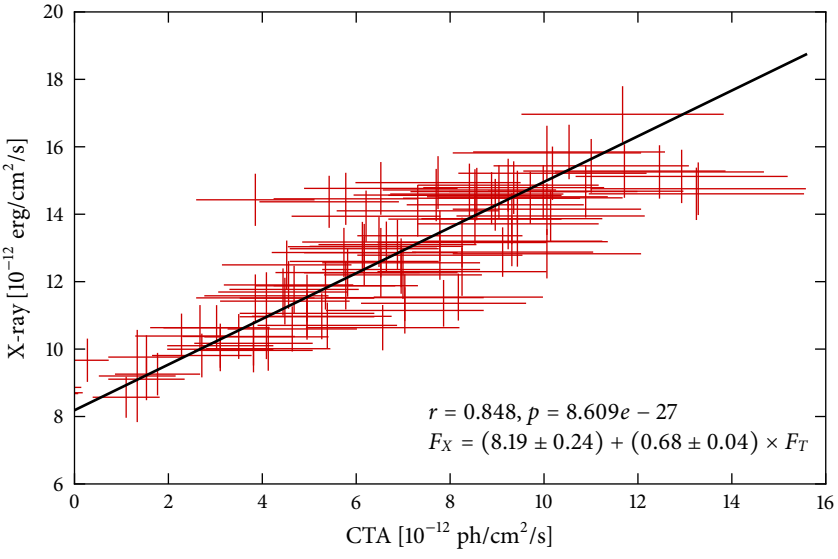

Figure C.4: X-ray/VHE correlation plot from the ten-night, subarray s9-2-120 observation plotted in 1000 s bins. The Pearson correlation factor, the chance probability of correlation and the parameters of the fitted correlation are shown as insets.

tegration time, we see that CTA is able to recover the X-ray/VHE correlation with high significance if the X-ray flux variation is large enough (Fig. C.2). The second observation scenario consists of a longer observational campaign of about ten nights. Given the foreseeable time pressure on CTA, this campaign would not be done with the full array but with a so-called subarray, a subset of the 100 telescopes that may operate independently. Here we chose a subarray configurations similar to an expanded HESS: nine medium sized telescopes located at a distance of 120 m from each other, known as `s9-2-120`. In Figure C.3 we see that the longer observation time allows the campaign to probe a wider range of X-ray fluxes, as well as different scales of variability from kiloseconds up to a few hours. Even with the reduced sensitivity of the subarray as compared to the full array, the correlation is well recovered (see Fig. C.4), partly owing to the aforementioned wider X-ray flux coverage.

As a conclusion from this simulation exercise, we see that the full CTA array will be a powerful tool to probe into the fast flux variability of gamma-ray binaries. In addition, we have shown that subarray operations must be encouraged since they are able to provide very interesting results using only a fraction of the full array. They will prove invaluable not only in observational campaigns where the long-term variability is important, but also to monitor flaring sources such as gamma-ray binaries and AGNs.

C.2 Sensitivity to spectral shape variations

There have been some hints of VHE spectral variability of LS I +61 303 along the orbit (Jogler, 2009), but they were not significant enough to be claimed as real. Here we consider a variation of the power-law VHE spectrum of LS I +61 303 within the statistical error obtained in the MAGIC campaign on September 2007 (See Chapter 3) and test the time required by CTA to significantly detect it. The measured spectral index was $\Gamma = 2.7 \pm 0.3$ (Eq. 3.1), so we took the two extreme values (2.4 and 3.0) and obtained the simulated CTA spectra keeping the integrated flux above 300 GeV constant. We found that an observation with the full CTA `I` array of 4 h for each of the spectral states (i.e., one night per state) provides a set of spectra from which the photon index variations can be clearly seen. The difference between the hard ($\Gamma_H = 2.4$) and soft ($\Gamma_S = 3.0$) is detected at a confidence level of nearly 10σ. Considering the difference with the mean spectral shape of $\Gamma_M = 2.7$, the significance is lower but still very good at a level of 5σ (see Fig. C.5). We also considered the possibility of longer observations with the subarray `s9-2-120`. In this case, for an observation of 10 h for each of the spectral states, the spectral variation is still significant at a level of, at least, 3.7σ for the comparison of the soft

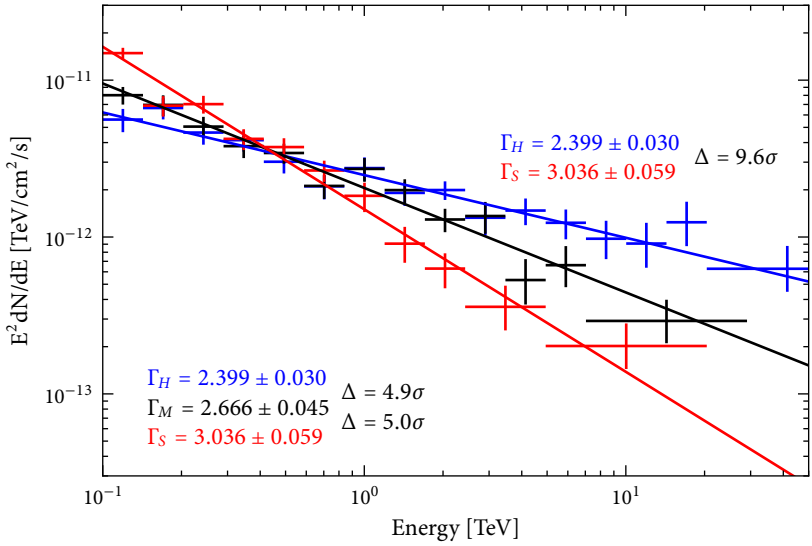

Figure C.5: Simulated spectra and power-law fits for 4 h of observation with the full CTA I array for each of the spectral states. The measured power-law indices and the significance of the variations is shown.

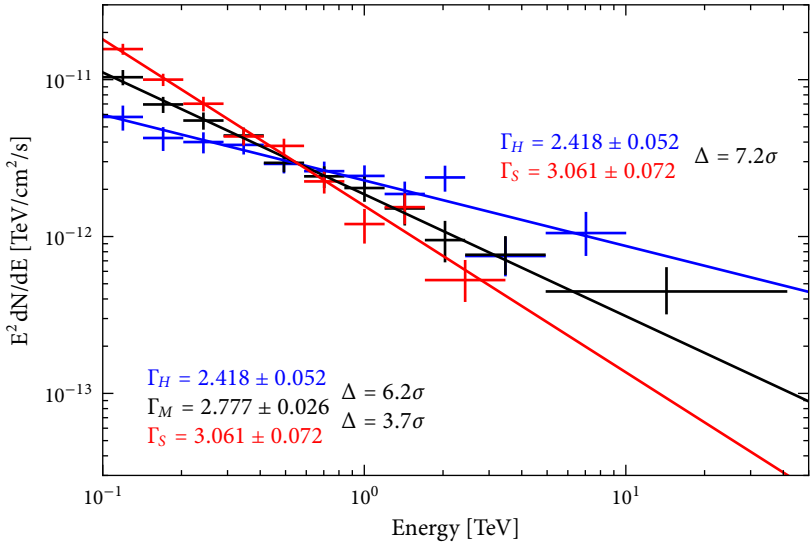

Figure C.6: Simulated spectra and power-law fits for 10 h of observation with the subarray s9-2-120 array for each of the spectral states. The measured power-law indices and the significance of the variations is shown.

and mean spectra (see Fig. C.6). It is clear that CTA will be a powerful tool for the detection of spectral variations in gamma-ray binaries. The statistical errors we obtained for these simulations are nearly an order of magnitude lower than the ones obtained with MAGIC in 2007, thus demonstrating the capability of CTA to deliver new and exciting science in the following years.

References

CTA Consortium. 2010, arXiv:1008.3703

Jogler, T. 2009, PhD thesis, Technische Universität München

Rea, N., Torres, D. F., van der Klis, M., Jonker, P. G., Méndez, M., & Sierpowska-Bartosik, A. 2010, MNRAS, 405, 2206

Sidoli, L., Pellizzoni, A., Vercellone, S., Moroni, M., Mereghetti, S., & Tavani, M. 2006, A&A, 459, 901

List of Figures

List of Tables

List of Acronyms

CTA Cherenkov Telescope Array
CD Contact discontinuity
CGRO Compton Gamma-Ray Observatory
EAS Extensive Air Shower
EGRET Energetic Gamma Ray Experiment Telescope
FB Flaring Branch
GLAST Gamma-Ray Large Area Space Telescope
HB Horizontal Branch
HE High energy
HESS High Energy Stereoscopic System
HMXB High-mass X-ray binary
IACT Imaging Atmospheric Cherenkov Telescope
IC Inverse Compton
ISM Interstellar medium
LMXB Low-mass X-ray binary
MAGIC Major Atmospheric Gamma-ray Imaging Cherenkov
NB Normal Branch
PCA Proportional Counter Array
PWS Pulsar Wind Shock
RXTE Rossi X-ray Timing Experiment
SED Spectral Energy Distribution
SNR Supernova remnant
SSC Synchrotron self-Compton
VERITAS Very Energetic Radiation Imaging Telescope Array System
VHE Very high energy
WCR Wind Collision Region

Colophon

This thesis was typeset with LaTeX 2_ε using Robert Slimbach's *Minion* and *Myriad* type faces for body text and headlines, respectively. In addition, Herman Zapf's *Euler* was used for chapter numbers and Donald Knuth's *Computer Modern* for typewriter text. All the figures in this thesis, with exception of those included from other works and Figures 3.1 and 3.3, have been generated using matplotlib, an open source plotting library for Python.

The thesis style is based on the classicthesis package by André Miede, available via CTAN, which is in turn inspired by Robert Bringhurst's book *The Elements of Typographic Style*.

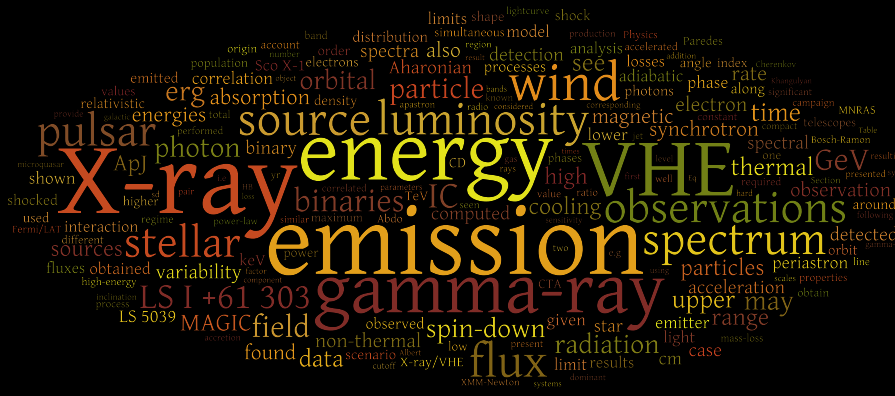

UNIVERSITAT DE BARCELONA